

JOINT SPARSITY-DRIVEN INVERSION AND
MODEL ERROR CORRECTION FOR SAR
IMAGING

by N. Özben Önhon

Submitted to the Graduate School of Sabancı University
in partial fulfillment of the requirements for the degree of
Doctor of Philosophy

Sabancı University
February, 2012

JOINT SPARSITY-DRIVEN INVERSION AND MODEL ERROR
CORRECTION FOR SAR IMAGING

APPROVED BY

Assist. Prof. Dr. Müjdat ÇETİN
(Thesis Supervisor)

Prof. Dr. Aytül ERÇİL

Prof. Dr. Orhan ARIKAN

Assoc. Prof. Dr. Gözde ÜNAL

Assoc. Prof. Dr. S. İlker BİRBİL

DATE OF APPROVAL:

© N. Özben Önhon 2012
All Rights Reserved

JOINT SPARSITY-DRIVEN INVERSION AND MODEL ERROR CORRECTION FOR SAR IMAGING

N. Özben Önhon

EE, PhD Dissertation, 2012

Thesis Supervisor: Müjdat Çetin

Keywords: Synthetic Aperture Radar, Regularization-based imaging, Sparsity,
Model errors, Phase errors, Autofocus

Abstract

Image formation algorithms in a variety of applications have explicit or implicit dependence on a mathematical model of the observation process. Inaccuracies in the observation model may cause various degradations and artifacts in the reconstructed images. The application of interest in this thesis is synthetic aperture radar (SAR) imaging, which particularly suffers from motion-induced model errors. These types of errors result in phase errors in SAR data which cause defocusing of the reconstructed images. Particularly focusing on imaging of fields that admit a sparse representation, we propose a sparsity-driven method for joint SAR imaging and phase error correction. In this technique, phase error correction is performed during the image formation process. The problem is set up as an optimization problem in a nonquadratic regularization-based framework. The method involves an iterative algorithm each iteration of which consists of consecutive steps of image formation and model error correction. Experimental results show the effectiveness of the proposed method for various types of phase errors, as well as the improvements it provides over existing techniques for model error compensation in SAR.

SAR GÖRÜNTÜLEME İÇİN ORTAK SEYREKLİK GÜDÜMLÜ GERİÇATIM VE MODEL HATASI DÜZELTİMİ

N. Özben Önhon

EE, Doktora Tezi, 2012

Tez Danşmanı: Müjdat Çetin

Keywords: Sentetik Açıklıklı Radar, Düzenliştirmeye dayalı görüntü oluşturma,
Seyreklik, Model hataları, Faz hataları, Otomatik odaklama

Özet

Çeşitli uygulamalardaki görüntü oluşturma algoritmaları açık veya kapalı olarak gözlem sürecinin matematiksel modeline bağlıdır. Gözlem modelindeki hatalar, oluşturulan görüntüde kötüleşmeye ve çeşitli bozukluklara neden olabilmektedir. Bu tezin ilgi alanı ise özellikle harekete bağlı model hatalarının ortaya çıktığı sentetik açıklıklı radar (synthetic aperture radar (SAR)) görüntü oluşturmadır. Bu tip hatalar SAR verisinde faz hatalarına, faz hataları da oluşturulan görüntülerde bulanıklaşmaya yol açmaktadır. Özellikle seyrek gösterimle ifade edilebilecek sahneleri gözönüne alarak, aynı anda hem SAR görüntüsü oluşturan hem de faz hatalarının giderilmesini sağlayan seyreklik güdümlü bir yöntem öneriyoruz. Bu yöntemde, faz hataları görüntü oluşturma aşamasında düzeltilmektedir. Problem, karesel olmayan düzenliştirmeye dayalı bir çerçevede, bir eniyileme problemi olarak ele alınmaktadır. Yöntem yinelemeli bir algoritmaya sahip olup, her yineleme, görüntü oluşturma ve model hatası düzeltimi olmak üzere ardışık iki basamaktan oluşmaktadır. Deneysel sonuçlar, önerilen yöntemin, hem çeşitli tipteki faz hataları için etkinliğini hem de SAR görüntülemesindeki model hatalarının giderilmesi için geliştirilmiş yöntemlere göre üstünlüklerini göstermektedir.

Acknowledgements

I am very happy for being at the end of the PhD and for writing these sentences. I have tried to write the thesis as clear as possible. I apologize in advance, for any mistakes or any wrong expressions existing in the thesis which I have not noticed. I hope this thesis will be useful for the people working in the same area.

I owe thanks to many people for their help during my PhD.

First of all, I would like to thank my advisor Müjdat Çetin for his continuous guidance, unlimited patience and for his kindness. I feel very lucky to have an advisor like him. He has been friendly and helpful all the time. I am very grateful to him for his persistent support and encouragement.

I would like to thank Aytül Erçil for her generosity and support. I would like to thank her also for being a member of my thesis jury. To see her smiling face and her joyful personality always let me feel better.

I also would like to thank my thesis committee members Gözde Ünal and Ilker Birbil for the help and suggestions they have provided and for their understanding.

I owe special thanks to Orhan Arıkan for accepting to be a member of my thesis jury which is invaluable for me.

I also would like to thank Hakan Erdoğan and Özgür Erçetin for their kindness and helpfulness.

I would like to thank all VPA Lab members from my heart, for their friendship, for the useful conversations and for their support. I am very happy for knowing all of the people in the VPA Lab. I have really enjoyed working with them.

Finally, I would like to thank my family for their infinite support and love without which I could not write this thesis.

Contents

1	Introduction	1
1.1	A Brief History of Synthetic Aperture Radar (SAR)	1
1.2	SAR Autofocus Problem	3
1.3	Overview of Existing State-of-the-Art Approaches and the Contributions of the Thesis	4
1.4	Organization of the Thesis	7
2	Preliminaries	9
2.1	SAR Background	9
2.1.1	Introduction to SAR	9
2.1.2	SAR Imaging Model	11
2.1.3	Range and Cross-range Resolution	15
2.1.4	Conventional Imaging (Polar-Format Algorithm)	16
2.2	Phase Errors	16
2.2.1	2D Non-separable Phase Errors	21
2.2.2	2D Separable Phase Errors	22
2.2.3	1D Phase Errors	23
2.3	Existing Autofocus Techniques	23
2.3.1	Conventional Approaches	23
2.3.2	Phase Gradient Autofocus (PGA)	25
2.3.3	Autofocus Techniques based on the Optimization of the Sharpness Metrics of the Defocused Image Intensity	28
2.3.4	Multi-Channel Autofocus (MCA)	30
2.4	Regularization Based Image Reconstruction	34
2.4.1	Least Squares Solutions	35

2.4.2	Tikhonov Regularization	35
2.4.3	Nonquadratic Regularization	36
3	Sparsity-Driven Autofocus (SDA)	38
3.1	Principles and Development of SDA	38
3.1.1	Algorithm for 1D Phase Errors	41
3.1.2	Algorithm for 2D Separable Phase Errors	43
3.1.3	Algorithm for 2D Non-separable Phase Errors	44
3.2	Experimental Results	45
3.2.1	Qualitative Results and Comparison to the Uncompensated Case	45
3.2.2	Quantitative Results in Comparison to State-of-the-art Auto- focus Methods	60
4	Moving Target Imaging	71
4.1	SAR Imaging Model	72
4.2	Proposed Method	73
4.2.1	Phase Error Estimation and Correction by Determining Re- gions of Interest (ROI)	76
4.3	Experimental Results	79
5	Conclusion and Potential Future Research	87
5.1	Conclusion	87
5.2	Potential Future Research	88
5.2.1	Application of the Proposed Method to Other Areas	88
5.2.2	Using the Proposed Framework with Other Dictionaries	88
5.2.3	Adaptive Approaches in Regularization-based Imaging	89
5.2.4	Velocity Estimation using the Corresponding Phase Error Es- timate	89
5.2.5	Imaging of Moving Targets with Reflectivities Changing in Time	90
5.2.6	Multi-static SAR Applications	90
5.2.7	Group Sparsity Approach for Moving Target Imaging	91
A	Appendix	92

List of Figures

1.1	Electromagnetic spectrum	2
1.2	SAR image of a military vehicle	3
2.1	SAR data collection geometry	10
2.2	SAR flightpath and imaging geometry	12
2.3	Reflected signal	13
2.4	Annular patch	14
2.5	2D data collection geometry	19
2.6	Linear components of a quadratic phase error function	26
2.7	Algorithm of PGA	29
2.8	Graphical illustration of multi-channel nature of the SAR autofocus problem.	31
2.9	Region of support condition for MCA.	34
3.1	(a) The original scene. (b) Conventional imaging from the data with- out phase errors. (c) Sparsity-driven imaging from the data without phase errors.	46
3.2	Left- Phase error. Middle- Images reconstructed by conventional imaging. Right- Images reconstructed by the proposed SDA method. (a) Results for quadratic phase error. (b) Results for an 8th order polynomial phase error. (c) Results for a phase error uniformly dis- tributed in $[-\pi/2, \pi/2]$	47

3.3	Experimental results on a speckled scene. (a) Conventional image reconstructed from noisy data without phase error. (b) Conventional image reconstructed from noisy data with phase error. (c) Image reconstructed by sparsity-driven imaging from noisy data with phase error. (d) Image reconstructed by the proposed SDA method.	48
3.4	(a) Photo of the Slicy target. (b) Conventional imaging from the data without phase error. (c) Sparsity-driven imaging from the data without phase error.	49
3.5	Top- Images reconstructed by conventional imaging. Middle- Images reconstructed by sparsity-driven imaging. Bottom- Images reconstructed by the proposed SDA method. (a) Results for a 1D quadratic phase error. (b) Results for a 1D phase error uniformly distributed in $[-\pi, \pi]$	50
3.6	Top- Images reconstructed by conventional imaging. Middle- Images reconstructed by sparsity-driven imaging. Bottom- Images reconstructed by the proposed SDA method. (a) Results for a 2D separable phase error composed of two 1D phase errors uniformly distributed in $[-3\pi/4, 3\pi/4]$. (b) Results for a 2D non-separable phase error uniformly distributed in $[-\pi, \pi]$	51
3.7	Results for a 2D separable phase error composed of two 1D phase errors, one of which is uniformly distributed in $[-\pi, \pi]$ and the other is uniformly distributed in $[-\pi/2, \pi/2]$. (a) Conventional imaging. (b) Image reconstructed by the proposed SDA method (the order of phase error estimation process: 1)for cross-range direction 2)for range direction). (c) Image reconstructed by the proposed SDA method (the order of phase error estimation process: 1)for range direction 2)for cross-range direction). (d) Difference between the cross-range dependent phase error estimates of two cases. (e) Difference between the range dependent phase error estimates of two cases.	53
3.8	(a)The facet of the Backhoe vehicle. (b) Conventional imaging from the data without phase error. (c) Sparsity-driven imaging from the data without phase error.	55

3.9	Top- Images reconstructed by conventional imaging. Middle- Images reconstructed by sparsity-driven imaging. Bottom- Images reconstructed by the proposed SDA method. (a) Results for a 1D phase error uniformly distributed in $[-\pi/2, \pi/2]$. (b) Results for a 2D separable phase error composed of two 1D phase errors uniformly distributed in $[-3\pi/4, 3\pi/4]$	56
3.10	Experiments on the Slicy data with 30% frequency band omissions : (a) Conventional imaging from the data without phase error. (b) Sparsity-driven imaging from the data without phase error.	57
3.11	Experiments on the Slicy data with 30% frequency band omissions and 1D random phase error uniformly distributed in $[-\pi, \pi]$: (a) Conventional imaging. (b) Sparsity-driven imaging. (c) Proposed SDA method.	57
3.12	Experiments on the Slicy data with 70% frequency band omissions : (a) Conventional imaging from the data without phase error. (b) Sparsity-driven imaging from the data without phase error.	58
3.13	Experiments on the Slicy data with 70% frequency band omissions and 1D quadratic phase error: (a) Conventional imaging. (b) Sparsity-driven imaging (c) Proposed SDA method.	58
3.14	Results of the experiment for testing the effect of the nonquadratic regularization term in the proposed SDA method on phase error compensation. (a) The original scene. (b) Conventional imaging from the data with phase error. (c) Image reconstructed in the case of replacing the l_1 -norm in our approach with an l_2 -norm without changing the phase error estimation piece. (d) Image reconstructed by the proposed SDA method.	59
3.15	(a) The original scene. (b) Conventional imaging from noisy data with phase error. Results of the proposed SDA method for various regularization parameter (λ) values. (c) $\lambda = 0.5$. (d) $\lambda = 1$. (e) $\lambda = 1.5$. (f) $\lambda = 2.5$. (g) $\lambda = 25$. (h) $\lambda = 50$. (i) $\lambda = 100$. (j) $\lambda = 2000$. (k) $\lambda = 2500$. (l) $\lambda = 4000$	61

3.16	(a) The original scene. (b) Conventional imaging from noisy data without phase error. (c) Conventional imaging from noisy data with phase error. (d) Result of PGA. (e) Result of entropy minimization. (f) Result of the proposed SDA method.	62
3.17	MSE evaluation of the reconstruction of the scene in Figure 3.14(a) for various SNRs. Each point on the curves corresponds to an average over 20 experiments with different random 1D phase errors uniformly distributed in $[-\pi, \pi]$	65
3.18	Target-to-background ratio evaluation of the reconstruction of the scene in Figure 3.14(a) for various SNRs. Each point on the curves corresponds to an average over 20 experiments with different random 1D phase errors uniformly distributed in	65
3.19	MSE evaluation of phase error estimations for the scene in Figure 3.14(a) for various SNRs. Each point on the curves corresponds to an average over 20 experiments with different random 1D phase errors uniformly distributed in	66
3.20	Experiments on the Backhoe data for a 1D random phase error with a uniform distribution in $[-\pi, \pi]$. (a) Conventional imaging from data without phase error. (b) Sparsity-driven imaging from data without phase error. (c) Conventional imaging with phase error. (d) Result of PGA. (e) Result of entropy minimization. (f) Result of the proposed SDA method.	67
3.21	(a) The original scene. (b) Conventional imaging from noisy phase-corrupted data for input SNR of 27dB. (c) Result of MCA for input SNR of 27dB. (d) Result of the proposed SDA method for input SNR of 27dB. (e) Conventional imaging from noisy phase-corrupted data for input SNR of 10dB. (f) Result of MCA for input SNR of 10dB. (g) Result of the proposed SDA method for input SNR of 10dB. . . .	69
3.22	MSEs for phase error estimation versus SNR.	70

4.1	Results of the first experiment. a) Original scene. b) Image reconstructed by conventional imaging. c) Image reconstructed by sparsity-driven imaging. d) Image obtained by using the PGA method for space-invariant focusing. e) Image reconstructed by the SDA method for space-invariant focusing. f) Image reconstructed by the proposed method for space-variant focusing.	82
4.2	Results of the second experiment. a) Original scene. b) Image reconstructed by conventional imaging. c) Image reconstructed by sparsity-driven imaging. d) Image obtained by using the PGA method for space-invariant focusing. e) Image reconstructed by the SDA method for space-invariant focusing. f) Image reconstructed by the proposed method for space-variant focusing.	83
4.3	Results of the third experiment. a) Original scene. b) Image reconstructed by conventional imaging. c) Image reconstructed by sparsity-driven imaging. d) Image reconstructed by the proposed method. . .	84
4.4	Results of the fourth experiment. a) Original scene. b) Image reconstructed by conventional imaging. c) Image reconstructed by sparsity-driven imaging. d) Image reconstructed by the proposed method. e) Image reconstructed by the proposed method with phase error estimation for ROI.	85
4.5	Results of the fifth experiment. a) Original scene. b) Image reconstructed by conventional imaging. c) Image reconstructed by sparsity-driven imaging. d) Image reconstructed by the proposed method with phase error estimation for ROI.	86

List of Tables

3.1	SAR System Parameters used in the synthetic scene experiment whose results are shown in Figures 3.1 and 3.2.	45
3.2	MSE achieved by various methods in estimating the phase error for the Backhoe experiment in Figure 3.20.	68
4.1	SAR System Parameters for Experiments in Figure 4.4 and Figure 4.5	81

Chapter 1

Introduction

This dissertation presents a new approach to the synthetic aperture radar (SAR) autofocus problem. The purpose of this chapter is to: 1) give a brief history of SAR; 2) introduce the SAR autofocus problem; 3) give an overview of existing approaches and provide a concise description of the approach taken in this work by pointing out the main contributions; 4) present the outline of the dissertation.

1.1 A Brief History of Synthetic Aperture Radar (SAR)

In 1960s, cameras and passive radiometers were the most used remote sensing sensors to observe a field on the earth [1]. Since these sensors operate in the visible or infrared part of the electromagnetic spectrum, they provide fine spatial resolution. Today, they are still used. However, they are limited with the daylight and weather conditions. With this type of sensors, imaging may not be possible during night or in the existence of cloud cover, rain or fog. On the other hand, we know that the speed of electromagnetic waves is a constant and in the electromagnetic spectrum, shown in Figure 1.1, as the frequency increases the wavelength decreases and microwaves have longer wavelengths than the visible and infrared light. This property of microwave signals help us to overcome cloud cover problem. However, since the discriminatory power of an optical system is reversely proportional to the wavelength of the illuminating source and proportional to the antenna aperture size,

to obtain a good enough resolution with microwave signals, very large antenna aperture sizes need to be used. This fact will be explained in Section 2.1 in more detail.

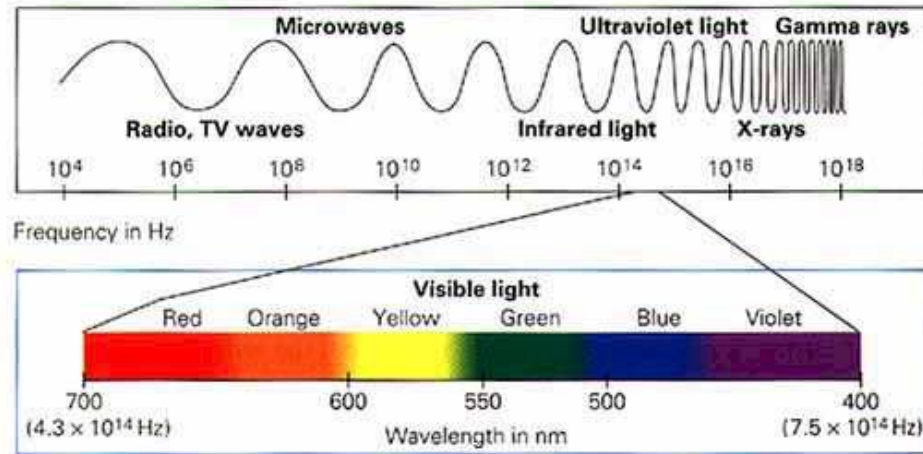


Figure 1.1: Electromagnetic spectrum (Image taken from the website of Princeton University.)

Carl Wiley, working at Goodyear (which later became Goodyear Aerospace, and eventually Lockheed Martin Corporation), in 1951, found that the construction of a detailed image is possible with a reasonable antenna aperture size based on the principle that each object in the radar beam has a slightly different speed relative to the non-moving antenna [2]. Approximately one year after Wiley, researchers at the University of Illinois independently developed the same idea, as well as developing beam-sharpening and autofocus concepts. In 1957, the first practical airborne SAR is developed and used by the University of Michigan [2]. With the development of SAR, the spatial-resolution problem arising due to the usage of microwave signals is solved and this fact led to the idea of using a satellite with a SAR sensor for oceanic observations. In 1978, the first civilian application of synthetic aperture radar, SEASAT, was launched. Unfortunately, SEASAT could operate only from June to October due to a short circuit in its power system [2]. After SEASAT, the evolution of SAR continued with Soviet 1870 SAR in 1987 and then with Magellan SAR, which imaged Venus, in 1990. Beginning from 90s many SARs have been placed on satellites in space. Some of them are as follows: Soviet ALMAZ and European ERS-1 (1991), Japanese JERS-1 (1992), SIR-C (1994), ERS-2(1995),

Canadian RADARSAT-1 (1995), SRTM (2000) and ENVISAT (2002) [1]. Synthetic aperture radar (SAR) has recently been and continues to be a sensor of great interest in a variety of remote sensing applications including military, atmospheric, geological and space observation processes. In Figure 1.2, an example of a SAR image is displayed.

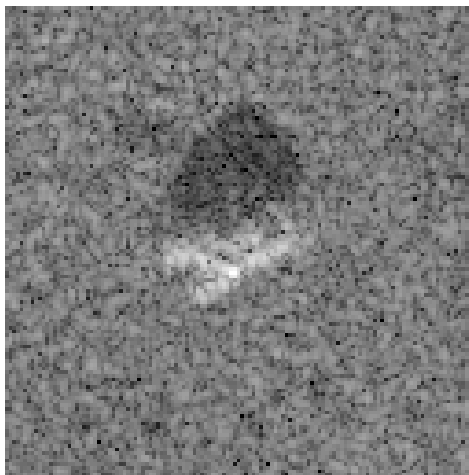


Figure 1.2: SAR image of a military vehicle

1.2 SAR Autofocus Problem

Due to the advantages of SAR over other sensing modalities, SAR image formation has become an important research topic. The problem of SAR image formation is a typical example of inverse problems in imaging. Solution of inverse problems in imaging requires the use of a mathematical model of the observation process. However such models often involve errors and uncertainties themselves. As a predominant example in SAR imaging, motion-induced errors are reasons for model uncertainties which may cause undesired artifacts in the formed imagery. In SAR systems, at every aperture position the demodulation time, which is the time required for the signal transmitted by the SAR sensor to propagate from the SAR platform to the field and back, is needed to obtain the data used for imaging, from the returned signals. The inexact knowledge of the demodulation time causes phase errors in the SAR data which result in defocusing of the reconstructed images [3].

The most common causes of demodulation time errors are the inexact measurement of the distance between the SAR platform and the field due to SAR platform position uncertainties or random delays in the signal due to propagation in atmospheric turbulence. Because of the defocusing effect of such errors, this problem is known as SAR autofocus problem and the techniques developed for removing phase errors are often called autofocus techniques. Besides the SAR platform position uncertainties, presence of moving targets in the scene cause phase errors as well. However, the phase errors caused by moving targets does not affect the entire image, the defocusing appears only in the parts of the image where moving targets exist, i.e., these phase errors cause space-variant defocusing.

1.3 Overview of Existing State-of-the-Art Approaches and the Contributions of the Thesis

Various studies have been presented on the SAR autofocus problem [4–19]. One of the most well known techniques, Phase Gradient Autofocus (PGA) [4], estimates phase errors using the data obtained by isolating many single defocused targets via center-shifting and windowing operations. It is based on the assumption that there is a single target at each range coordinate. Another well-known approach for autofocus is based on the optimization of a sharpness metric of the defocused image intensity [5–12]. These techniques aim to find the phase error estimate which minimizes or maximizes a sharpness function of the conventionally reconstructed image. Commonly used metrics are entropy or square of the image intensity. Techniques such as mapdrift autofocus [13] use subaperture data to estimate the phase errors. These techniques are suitable mostly for quadratic and slowly varying phase errors. A recently proposed autofocus technique, multichannel autofocus (MCA) [14], is based on a non-iterative algorithm which finds the focused image in terms of a basis formed from the defocused image, relying on a condition on the image support to obtain a unique solution. In particular, MCA estimates 1D phase error functions by directly solving a set of linear equations obtained through an assumption that there are zero-reflectivity regions in the scene to be imaged. When this is not precisely satisfied, presence of a low-return region is exploited, and the phase error is estimated

by minimizing the energy of the low-return region. When the desired conditions are satisfied, MCA performs very well. However, in scenarios involving low-quality data (e.g., due to low SNR) the performance of MCA degrades. A number of modifications to MCA have been proposed, including the incorporation of sharpness metric optimization into the framework [14], and the use of a semidefinite relaxation based optimization procedure [19] for better phase error estimation performance.

One common aspect of all autofocus techniques referred to above is that they perform post-processing, i.e., they use conventionally reconstructed (i.e., reconstructed using 2D inverse Fourier transform) defocused images in the process of phase error estimation. Our starting point however is the observation that more advanced SAR image formation techniques have recently been developed. Of particular interest in this dissertation is regularization-based SAR imaging (see, e.g., [20–22]), which has been shown to offer certain improvements over conventional imaging. Regularization-based techniques can alleviate the problems in the case of incomplete data or sparse apertures. Moreover, they produce images with increased resolution, reduced sidelobes, and reduced speckle by incorporation of prior information about the features of interest and imposing various constraints (e.g., sparsity, smoothness) about the scene. However, existing regularization-based SAR imaging techniques rely on a perfect observation model, and do not involve any mechanism for addressing any model uncertainties.

Motivated by these observations and considering scenes that admit sparse representation in some dictionary, we propose a sparsity-driven technique for joint SAR imaging and phase error correction by using a nonquadratic regularization-based framework. In the proposed *sparsity-driven autofocus* (SDA) method, phase errors are considered as model errors which are estimated and removed during image formation. The proposed method handles the problem as an optimization problem in which the cost function is composed of a data fidelity term (which exhibits a dependence on the model parameters) and a regularization term, which is the l_1 - *norm* of the field. For simplicity we consider scenes that are spatially sparse, however our approach can be applied to fields that are sparse in any given dictionary by using an l_1 - *norm* penalty on the associated sparse representation coefficients. The cost function is iteratively minimized with respect to the field and the phase error using

coordinate descent. In the first step of every iteration, the cost function is minimized with respect to the field and in the second step the phase error is estimated given the field estimate. The phase error estimate is used to update the model matrix and the algorithm passes to the next iteration.

Sharpness-based autofocus techniques [5–12] share certain aspects of our perspective, but our approach is fundamentally different. In particular, our approach also involves a certain type of sharpness metric about the field, but inside of a cost function as a side constraint (regularization term) to a data fidelity term which incorporates the system model and the data into the optimization problem for image formation. Hence our approach imposes the sharpness-like constraint during the process of image formation, rather than as post-processing. This enables our technique to correct for artifacts in the scene due to model errors effectively, in an early stage of the image formation process. Furthermore, unlike existing sharpness-based autofocus techniques, our model error correction approach is coupled with an advanced sparsity-driven image formation technique which has the capability of producing high resolution images with enhanced features, and as a result our approach is not limited by the constraints of conventional SAR imaging. In fact, our approach benefits from a dual use of sparsity, both for model error correction (autofocusing) and for improved imaging. Finally, our framework is not limited to sharpness metrics on the scene, but can in principle be used for model error correction in scenes that admit a sparse representation in any given dictionary.

We have extended the framework we proposed, for space-variant defocusing problem caused by moving targets in the scene. The phase errors arising due to the uncertainties on the SAR platform position cause space-invariant defocusing, i.e., the amount of the defocusing in the reconstructed image is same for all points of the scene. Moving targets in the scene cause defocusing in the reconstructed image as well. However, this defocusing needs to be corrected with a space-variant refocus algorithm, since the defocusing appears only around the positions of the moving targets whereas the stationary background is not defocused. Therefore, autofocus techniques developed for space-invariant focusing cannot handle the defocusing arising in the imaging of a scene including multiple moving targets with different velocities.

This not only involves a nontrivial extension of the phase error estimation piece of our previous framework, but it also provides opportunities for incorporation of information about the expected spatial structure of the motion errors as well. In particular, in the new approach, we not only exploit the sparsity of the reflectivity field, but we also impose a constraint on the spatial sparsity of the phase errors based on the assumption that motion in the scene will be limited to a small number of spatial locations. The method effectively produces high resolution images and removes the cross-range dependent phase errors caused by moving targets.

In conclusion, the main contributions of the thesis can be summarized as follows:

- Existing autofocus techniques perform post-processing, i.e., they use conventionally reconstructed defocused images in the process of phase error estimation. However, our method performs SAR imaging and phase error correction, simultaneously.
- Existing autofocus techniques use conventionally reconstructed images. However, the proposed technique uses regularization-based imaging which has many advantages over conventional imaging.
- We have provided a closed-form solution for phase error estimation in every cross-range position.
- We have extended our initial framework to the space-variant defocusing problem arising in the case of moving targets in the scene.

1.4 Organization of the Thesis

In Chapter 2 we cover the preliminaries for our work. This chapter aims to explain basic SAR principles and provide necessary knowledge on phase errors, existing autofocus techniques and regularization-based imaging. In Chapter 3, we present our approach and explain the proposed technique in detail. Moreover, we present experimental results on synthetic scenes as well as on two public datasets provided by the U.S. Air Force Research Laboratory (AFRL) for different scenarios. We also provide results for comparison of our approach with three widely used existing autofocus techniques and a quantitative analysis of these experimental results. In

Chapter 4, we extend our framework for moving target imaging and present two procedures for space-variant focusing. Finally, Chapter 5 summarizes the results we have obtained, and indicates potential future research directions.

Chapter 2

Preliminaries

In this chapter, we provide preliminary knowledge about SAR, SAR autofocus problem and mention existing autofocus techniques. Finally, we cover the basics for regularization-based imaging.

2.1 SAR Background

2.1.1 Introduction to SAR

SAR is an imaging radar used in a significant part of remote sensing applications. A desirable property for a remote sensing device is being able to collect reliable data, independent from the illumination and weather conditions of the environment. SAR satisfies all these conditions since firstly it is an active sensor, so it produces its own signals which gives the ability for imaging both day and night. Secondly, the signals sent by SAR are microwave signals which enable imaging in adverse weather conditions as well. SAR is mostly used for imaging of the ground from an aircraft or a satellite. As shown in Figure 2.1, along the flight path of the aircraft (satellite) the SAR sensor regularly transmits signals to the ground and then receives the returned signals. The direction of radiation propagation called range direction where the one parallel to the flight path is called cross-range or azimuth direction. Imaging is performed using the data which are obtained after a pre-processing of the received signals. For SAR, resolution in the range direction is based on the basic echo principle, as in other radars. The transmitted signal is reflected from the

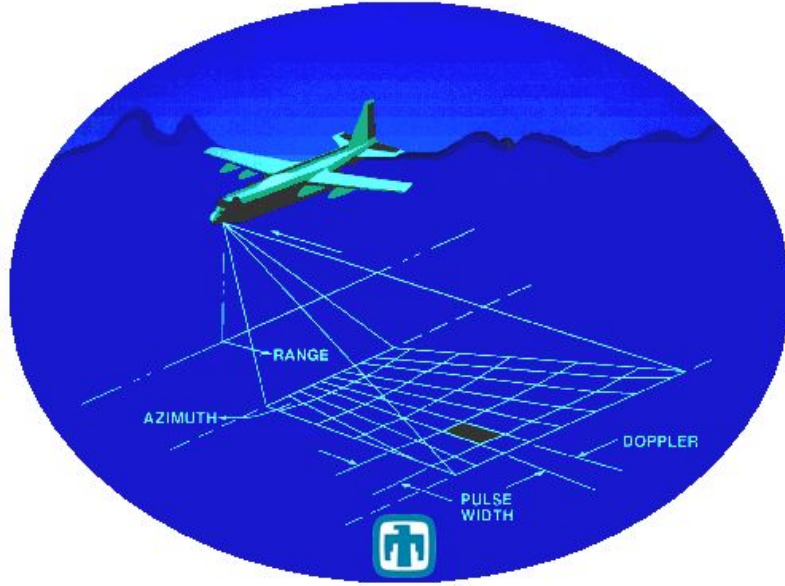


Figure 2.1: SAR data collection geometry. (Image obtained from the web site of Sandia National Laboratories.)

ground points that have the same distance to the SAR platform, at the same time. By using the round trip flight time and speed of the propagated signal, it is possible to find the distance between a point on the 2D scene and the SAR sensor. In this way, the points of a 2D scene which lie at different distances from the SAR sensor can be discriminated. However, cross-range resolution depends on the antenna aperture size. Cross-range resolution in radars and resolution in optical systems are analogous and can be expressed as

$$\rho = \frac{\lambda_w d}{w} \quad (2.1)$$

where λ_w is the wavelength of the illuminating source, d is the target range, and w is the width of the antenna aperture or the diameter of the lens. Let us consider an example, where the wavelength and d are 0.03m and 50km, respectively. This is a typical wavelength for an X-band radar. If we want a resolution of 1m, then according to the above expression we need an antenna aperture width of 1500m. As it is seen, to have a reasonable resolution in the cross-range direction, antennas of huge sizes, which are very impractical to carry on an aircraft or satellite, are

required. SAR solves this problem, by sending multiple pulses from a number of observation points, and then focusing the received information coherently to obtain a high-resolution 2D description of the scene. Hence it synthesizes the effect of a large antenna, using multiple observations from a small antenna [23].

2.1.2 SAR Imaging Model

In SAR imaging systems, one of the most widely used signals in transmission is the chirp signal:

$$s(t) = \text{Re} \left\{ e^{j(\omega_0 t + \alpha t^2)} \right\} \quad t \leq \frac{|T_{pulse}|}{2} \quad (2.2)$$

Here, ω_0 is the center frequency and 2α is the so-called chirp-rate. For spotlight-mode SAR, which is the modality of interest in this thesis, the received signal $q_m(t)$ at the m -th aperture position (cross-range position) involves the convolution of the transmitted chirp signal with the projection $p_m(u)$ of the field at that aperture position.

$$q_m(t) = \text{Re} \left\{ \int p_m(u) e^{j[\omega_0(t-\tau_0-\tau(u)) + \alpha(t-\tau_0-\tau(u))^2]} du \right\} \quad (2.3)$$

$$p_m(u) = \iint_{x^2+y^2 \leq L^2} \delta(u - x \cos \theta - y \sin \theta) F(x, y) dx dy \quad (2.4)$$

Here, L is the radius of the circular patch to be imaged, $F(x, y)$ denotes the underlying field and, θ is the observation angle at the m -th aperture position. The corresponding visual description is presented in Figure 2.2. If we let the distance from the SAR platform to the center of the field be d_0 , then $\tau_0 + \tau(u)$ is the delay for the returned signal from the scatterer at the range position $d_0 + u$, where τ_0 is the so called demodulation time. The corresponding graphical illustration is shown in Figure 2.3. The data used for imaging are obtained after a pre-processing step. In particular, the returned signal is first multiplied with delayed in-phase and quadrature versions of the transmitted chirp signal which are displayed in (2.5) and then the output is low-pass filtered [3].

$$\begin{aligned} s_I(t) &= \cos(\omega(t - \tau_0) + \alpha(t - \tau_0)^2) \\ s_Q(t) &= -\sin(\omega(t - \tau_0) + \alpha(t - \tau_0)^2) \end{aligned} \quad (2.5)$$

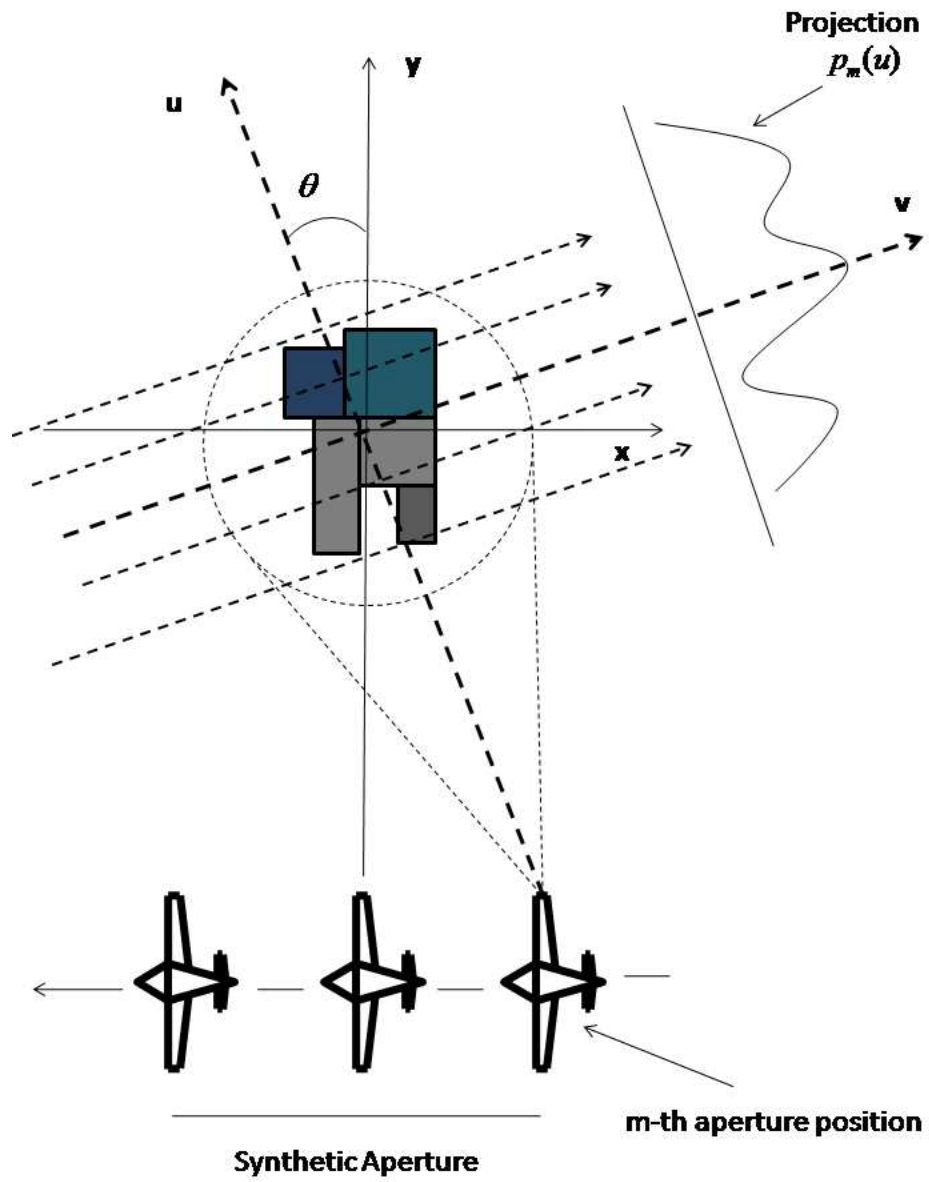


Figure 2.2: SAR flightpath and imaging geometry

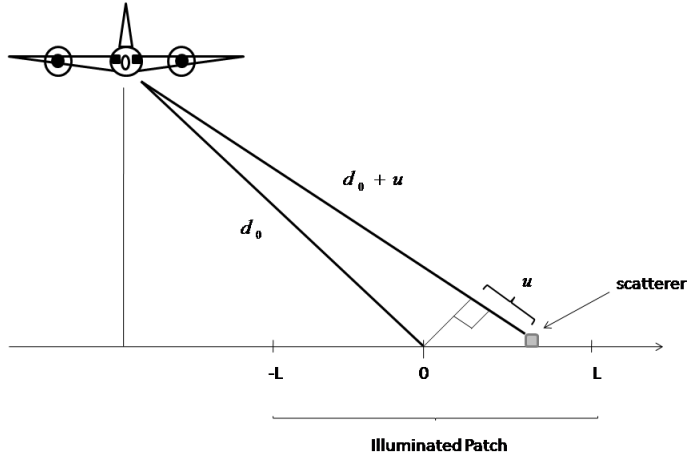


Figure 2.3: Reflected signal.

From the projection-slice theorem [24], the pre-processed SAR data $\bar{r}_m(t)$ obtained after this process, can be identified as a band-pass filtered Fourier transform of the projections of the field [25],

$$\bar{r}_m(t) = \int_{|u| \leq L} p_m(u) e^{-jUu} du \quad (2.6)$$

where

$$U = \frac{2}{c}(\omega_0 + 2\alpha(t - \tau_0)) \quad (2.7)$$

Here, c is the speed of light. In 2.6, a quadratic phase term of $\alpha\tau^2(u)$ is neglected. Substituting (2.4) into (2.6), we obtain the relationship between the observed data $\bar{r}_m(t)$ and the underlying field $F(x, y)$.

$$\bar{r}_m(t) = \iint_{x^2+y^2 \leq L^2} F(x, y) e^{-jU(x \cos \theta + y \sin \theta)} dx dy \quad (2.8)$$

All of the returned signals from all observation angles constitute a patch from the two dimensional spatial Fourier transform of the corresponding field. These data are called phase histories and lie on a polar grid in the 2D frequency domain as shown in Figure 2.4. Let the 2D discrete phase history data be denoted by a $K \times M$ matrix R . Column m of R , denoted by the $K \times 1$ vector \bar{r}_m , is obtained by sampling $\bar{r}_m(t)$ (the returned signal at cross-range position m), in fast-time t (range direction)

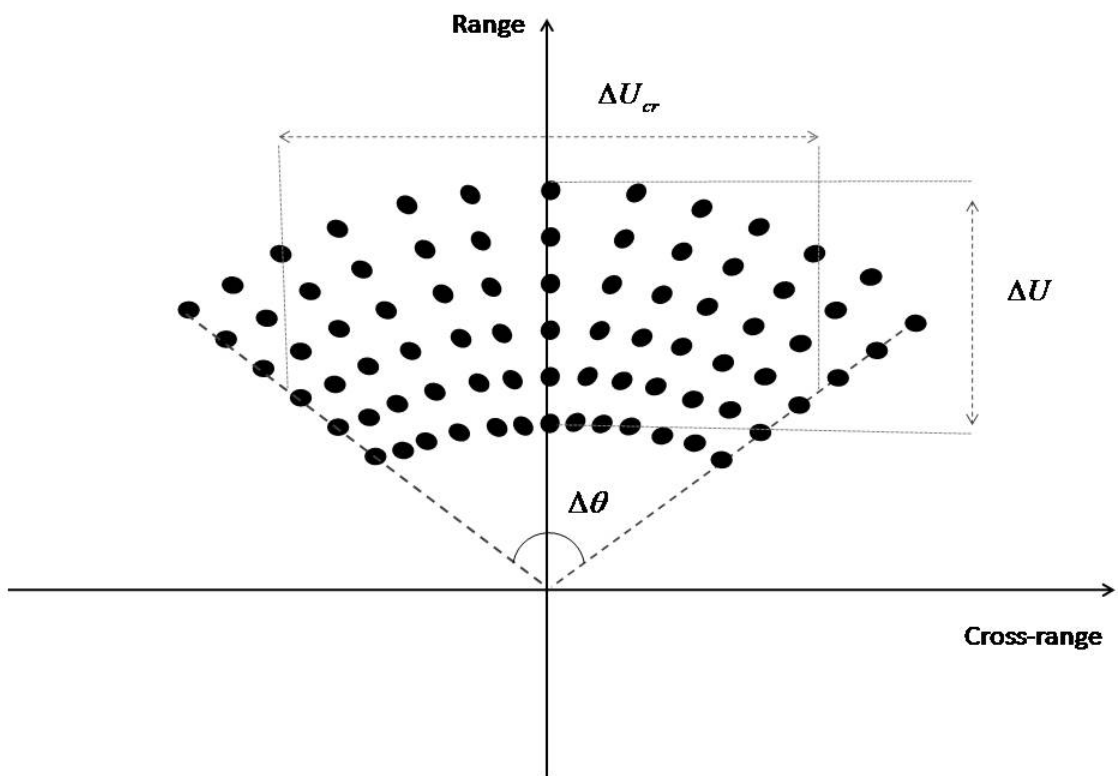


Figure 2.4: Graphical representation of an annulus segment containing known samples of the phase history data in the 2D spatial frequency domain.

at K positions. In terms of this notation, the discrete observation model can be formulated as follows [20]:

$$\underbrace{\begin{bmatrix} \bar{r}_1 \\ \bar{r}_2 \\ \vdots \\ \bar{r}_M \end{bmatrix}}_r = \underbrace{\begin{bmatrix} \bar{C}_1 \\ \bar{C}_2 \\ \vdots \\ \bar{C}_M \end{bmatrix}}_C f \quad (2.9)$$

Here, the vector r of observed samples is obtained just by concatenating the columns of the 2D phase history data R , under each other. \bar{C}_m and C are discretized approximations to the continuous observation kernel at the cross-range position m and for all cross-range positions, respectively. f is a vector representing the sampled and column-stacked version of the reflectivity image F . Note that K and M are the total numbers of range and cross-range positions, respectively.

2.1.3 Range and Cross-range Resolution

In the pre-processing step, for a certain aperture position, only the signals returning in the following time interval are considered:

$$\tau_0 - \frac{T_{pulse}}{2} + \frac{T_{prop}}{2} \leq t \leq \tau_0 + \frac{T_{pulse}}{2} - \frac{T_{prop}}{2} \quad (2.10)$$

Here, T_{pulse} is the duration of the transmitted chirp signal and T_{prop} is the patch propagation time and it is assumed that

$$T_{pulse} \gg T_{prop} \quad (2.11)$$

$\tau_0 - \frac{T_{pulse}}{2} + \frac{T_{prop}}{2}$ is the time at which the chirps returning from the far edge target are firstly received and $\tau_0 + \frac{T_{pulse}}{2} - \frac{T_{prop}}{2}$ is the time at which the chirps returning from the near edge target end. Therefore, the time interval in (2.10) is the only common time segment for which chirp returns from all targets in the field exist simultaneously [3]. If the limits for the observation time t from (2.10) are substituted into the definition of U in (2.7), the lowest and highest spatial frequencies are obtained as follows:

$$\frac{2}{c} (\omega_0 - \alpha (T_{pulse} - T_{prop})) \leq U \leq \frac{2}{c} (\omega_0 + \alpha (T_{pulse} - T_{prop})) \quad (2.12)$$

Since the transmitted chirp signal in (2.2) has a bandwidth of $\frac{\alpha T_{pulse}}{\pi}$ in the frequency domain and we have assumed that $T_{pulse} \gg T_{prop}$, we can write ΔU in Figure 2.4 as follows:

$$\Delta U \approx \frac{4\alpha T_{pulse}}{c} = \frac{4\pi B}{c} \quad (2.13)$$

To determine the cross-range resolution let us use the geometry in the Figure 2.4. According to that geometry, the following relationship can be obtained.

$$\sin\left(\frac{\Delta\theta}{2}\right) \approx \frac{\Delta U_{cr}/2}{U_0} \quad (2.14)$$

Here, $U_0 = 2\omega_0/c$. For very small $\Delta\theta$, the relationship in (2.14) leads to

$$\Delta U_{cr} \approx \frac{2\omega_0 \Delta\theta}{c} \quad (2.15)$$

As a result, using the fact that the wavelength of the transmitted signal is given by $\lambda_w = 2\pi c/\omega_0$, the following range and cross-range resolution expressions are obtained:

$$\begin{aligned} \rho_r &= \frac{2\pi}{\Delta U} \approx \frac{c}{2B} \\ \rho_{cr} &= \frac{2\pi}{\Delta U_{cr}} \approx \frac{\lambda_w}{2\Delta\theta} \end{aligned} \quad (2.16)$$

2.1.4 Conventional Imaging (Polar-Format Algorithm)

In Section 2.1.2, we mentioned that the SAR phase histories data correspond to the band-pass filtered 2D Fourier transform of the field. Consequently, the conventional imaging algorithm for SAR is the polar-format algorithm based on the 2D fast Fourier transform (FFT). In polar-format algorithm, first the data are interpolated from the polar grid to the Cartesian grid and then a 2D inverse Fourier transform is applied.

2.2 Phase Errors

In SAR imagery, the time required for each radar pulse from the SAR platform to the patch center and back is called the demodulation time which was defined as $\tau_0 = \frac{2d_0}{c}$ before. d_0 is the distance from the SAR platform to the patch center.

Conventionally, for each pulse, d_0 is measured with the inertial measurement units (IMUs) placed on the SAR platform. However, even with high quality IMU's, determining d_0 within the required tolerances is difficult. Erroneous d_0 measurements cause demodulation time errors. The demodulation time error results in phase errors in the SAR data obtained after pre-processing of the received signal. To deal with this problem, methods have been developed for increasing the accuracy of IMU systems and for automatically removing the phase errors by post-processing the reconstructed SAR images. The techniques developed for removal of the effects of demodulation time errors are called autofocus techniques and using these techniques has advantages over improving the accuracy of the IMU systems. Improving accuracy of the IMU systems helps only in the situations when the cause of phase errors is the SAR platform position uncertainty. However, except platform position uncertainties, random delays in the signal which occurs through atmospheric turbulence, also cause demodulation time errors. On the other hand, autofocus techniques can remove phase errors independent of the error source. Moreover, these techniques could help avoid significant hardware costs arising from the usage of high accuracy IMU systems.

Demodulation time errors can be modeled as constant phase errors on each range compressed pulse. All of the expressions for the SAR imaging model in Section 2.1.2 are based on the assumption that the demodulation time is known exactly. If the demodulation time is not known exactly, during pre-processing, the received signals are multiplied with

$$\begin{aligned} & \cos(\omega(t - \tau_0 + \epsilon) + \alpha(t - \tau_0 + \epsilon)^2) \\ & - \sin(\omega(t - \tau_0 + \epsilon) + \alpha(t - \tau_0 + \epsilon)^2) \end{aligned} \quad (2.17)$$

instead of the expressions in (2.5). Here, ϵ is the demodulation time error. In this case, the output of the preprocessing step becomes

$$Z_\epsilon(U) = \bar{r}_{m_\epsilon}(t) = e^{-j\epsilon^2\alpha} e^{j\frac{\epsilon c}{2}U} \int_{|u| \leq L} p_m(u) e^{-jUu} du \quad (2.18)$$

Accordingly, the phase corrupted and error-free data relate to each other as follows:

$$Z_\epsilon(U) = e^{-j\epsilon^2\alpha} e^{j\frac{\epsilon c}{2}U} Z(U) \quad (2.19)$$

Since $\epsilon^2\alpha \ll 1$, after the approximation of $e^{-j\epsilon^2\alpha} \approx 1$, the relationship between the erroneous and error-free data is obtained as in (2.20) [3].

$$Z_\epsilon(U) = e^{j\frac{\epsilon\epsilon}{2}U} Z(U) \quad (2.20)$$

If we substitute the expression in (2.19) into (2.20) we find

$$Z_\epsilon(U) = e^{j\epsilon\omega_0} e^{j\epsilon(2\alpha(t-\tau_0))} Z(U) \quad (2.21)$$

The value of $(2\alpha(t - \tau_0))$ is generally very small as compared to ω_0 , so if it is neglected, we obtain

$$Z_\epsilon(U) = e^{j\phi} Z(U) \quad (2.22)$$

where $\phi = \epsilon\omega_0$ is the phase error and it is different for every aperture position which means that it affects the reconstructed image along the cross-range. The implication of such an error in the image domain is the convolution of (each range line of) the image with a 1D blurring kernel in the cross-range direction. Hence, such phase errors cause defocusing of the image in the cross-range direction.

An example of SAR platform position uncertainties arises from errors in measuring the aircraft velocity. A constant error on aircraft velocity induces a quadratic phase error function in the data [3]. A simple 2D SAR data collection geometry is presented in Figure 2.5 for the analysis of such a scenario. The measured demodulation time τ_{0_ϵ} at any point in the aperture can be expressed as

$$\begin{aligned} \tau_{0_\epsilon} &= \frac{2}{c} \sqrt{d_0^2 + d_{1_\epsilon}^2} \\ \tau_{0_\epsilon} &\approx \frac{1}{c} \left(2d_0 + \frac{d_{1_\epsilon}^2}{d_0} \right) \\ \tau_{0_\epsilon} &= \frac{1}{c} \left(2d_0 + \frac{(v_\epsilon t_s)^2}{d_0} \right) \end{aligned} \quad (2.23)$$

where d_{1_ϵ} is the incorrect distance between the aircraft and the aperture center and v_ϵ is the measured velocity of the aircraft. If we let the correct aircraft velocity be v then the correct demodulation time should be

$$\tau_0 \approx \frac{1}{c} \left(2d_0 + \frac{(vt_s)^2}{d_0} \right) \quad (2.24)$$

Therefore, the error on the demodulation time becomes

$$\epsilon(t_s) = \tau_{0_\epsilon} - \tau_0 = \frac{1}{cd_0} (v^2 - v_\epsilon^2) t_s^2 \quad (2.25)$$

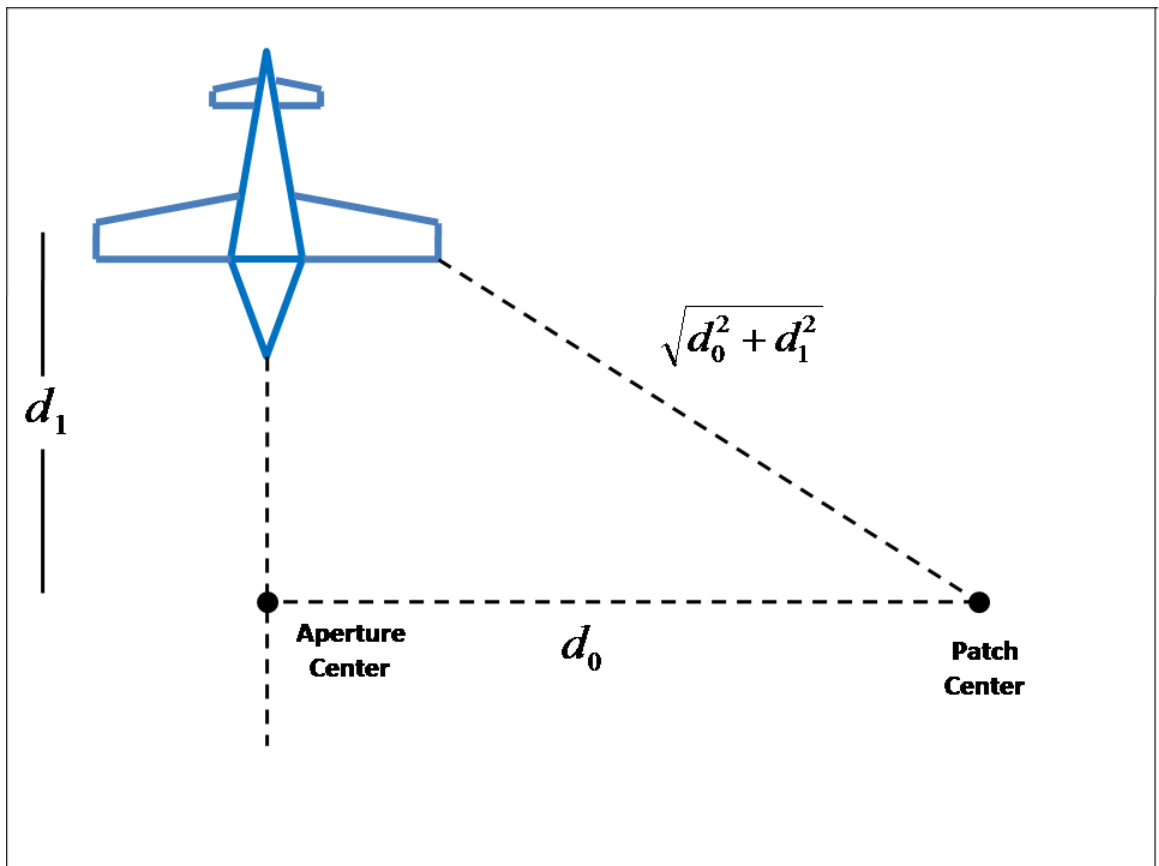


Figure 2.5: 2D data collection geometry

As seen in the Equation (2.25) the error is a quadratic function of aperture time (slow-time) t_s or in other words a quadratic function of aperture position vt_s which is denoted as m in the discrete data. This demodulation time error corresponds to a phase error of

$$\phi(t_s) = \epsilon(t_s) \omega_0 \quad (2.26)$$

which can be expressed in terms of the range position errors $\Delta d(t_s)$ as follows:

$$\phi(t_s) = \epsilon(t_s) \omega_0 = \frac{2\Delta d(t_s)}{c} \omega_0 = \frac{4\pi}{\lambda_w} \Delta d(t_s) \quad (2.27)$$

Since the defocus effect of a quadratic phase error with a peak value of $\pi/4$ radians is negligible [3], the maximum position error along the aperture which cause a negligible phase error can be obtained through:

$$\phi_{max} = \frac{\pi}{4} = \frac{4\pi}{\lambda_w} \Delta d_{max} \quad (2.28)$$

which leads to

$$\Delta d_{max} = \frac{\lambda_w}{16} \quad (2.29)$$

This result shows that the defocus effect of a range position error up to one sixteenth of a wavelength is negligible. Another implication of Equation (2.28) is that only one wavelength of relative range error corresponds to a phase error of 4π radians. It is important here to point out that a constant error in range position measurement for all pulses does not have a defocus effect in the reconstructed image. The defocus arising in the reconstructed image is due to the deviation on the range position measurement error from pulse to pulse. Usually, phase errors arising due to SAR platform position uncertainties are slowly-varying (e.g., quadratic, polynomial) phase errors, whereas phase errors induced by propagation effects are much more irregular (e.g., random) [3]. Quadratic phase errors cause spreading the mainlobe of the impulse response of a point target whereas the random phase errors raise its sidelobes which results in a loss of contrast in the image.

While most phase errors encountered are 1D cross-range varying functions, it is possible to encounter both range and cross-range varying 2D phase errors as well. For instance, in low frequency UWB SAR systems, severe propagation effects may

appear through the ionosphere, including Faraday rotation, dispersion, and scintillation [26] which cause 2D phase errors, defocusing the reconstructed image in both range and cross-range directions. Moreover, waveform errors such as frequency jitter from pulse to pulse, transmission line reflections and waveguide dispersion effects may cause defocus in both range and cross-range direction [27]. 2D phase errors can in principle be handled in two sub-categories as separable and non-separable errors, but it is not common to encounter 2D separable phase errors in practice.

For these three types of phase error functions, let us investigate the relationship between the phase-corrupted and error-free phase history data in terms of the observation model.

2.2.1 2D Non-separable Phase Errors

In the presence of 2D non-separable phase errors, all sample points of the $K \times M$ phase history data, denoted matrix R in Section 2.1.2, are perturbed with different and potentially independent phase errors. Let Φ_{2D-ns} be a 2D non-separable phase error function. The relationship between the phase-corrupted and error-free phase histories are as follows:

$$R_\epsilon(k, m) = R(k, m)e^{j\Phi_{2D-ns}(k, m)} \quad (2.30)$$

Here, R_ϵ denotes the phase-corrupted phase history data. To express this relationship in terms of the observation model, first we define the vector ϕ_{2D-ns}

$$\phi_{2D-ns} = \left[\phi_{2D-ns}(1), \phi_{2D-ns}(2), \dots, \phi_{2D-ns}(S) \right]^T \quad (2.31)$$

which is created by concatenating the columns of the phase error matrix Φ_{2D-ns} under each other. Here, S is the total number of data samples and equal to the product MK . Using the corresponding vector forms, the relationship in (2.30) becomes

$$r_\epsilon = D_{2D-ns}r \quad (2.32)$$

where D_{2D-ns} is a diagonal matrix:

$$D_{2D-ns} = \text{diag} \left[e^{j\phi_{2D-ns}(1)}, e^{j\phi_{2D-ns}(2)}, \dots, e^{j\phi_{2D-ns}(S)} \right] \quad (2.33)$$

In terms of observation model matrices, the relationship in (2.32) is as follows

$$C(\phi_{2D-ns})f = D_{2D-ns}Cf \quad (2.34)$$

where, C is the initially assumed model matrix by the imaging system and $C(\phi_{2D-ns})$ is the model matrix that takes the phase errors into account. The equations (2.32) and (2.34) can be expressed in the following form as well.

$$\begin{aligned} r_\epsilon(s) &= e^{j\phi_{2D-ns}(s)}r(s) \\ C_s(\phi_{2D-ns})f &= e^{j\phi_{2D-ns}(s)}C_s f \quad \text{for } s = 1, 2, \dots, S \end{aligned} \quad (2.35)$$

Here, $r(s)$ denotes s -th element of the vector r and C_s denotes s -th row of the model matrix C .

2.2.2 2D Separable Phase Errors

A 2D separable phase error function is composed of range varying and cross-range varying 1D phase error functions as follows:

$$\Phi_{2D-s}(k, m) = \xi(k) + \gamma(m) \quad (2.36)$$

Here, ξ , representing the range varying phase error, is a $K \times 1$ vector; and γ , representing the cross-range varying phase error, is a $M \times 1$ vector. The $S \times 1$ vector for 2D separable phase errors ϕ_{2D-s} , is obtained by concatenating the columns of Φ_{2D-s} as follows:

$$\phi_{2D-s} = \left[\underbrace{\xi(1) + \gamma(1)}_{\phi_{2D-s}(1)}, \dots, \underbrace{\xi(K) + \gamma(1)}_{\phi_{2D-s}(K)}, \underbrace{\xi(1) + \gamma(2)}_{\phi_{2D-s}(K+1)}, \dots, \underbrace{\xi(1) + \gamma(M)}_{\phi_{2D-s}((M-1)K+1)}, \dots, \underbrace{\xi(K) + \gamma(M)}_{\phi_{2D-s}(S)} \right]^T \quad (2.37)$$

A 2D separable phase error function affects the observation model matrix in the following manner:

$$\begin{aligned} r_\epsilon &= D_{2D-s}r \\ C(\phi_{2D-s})f &= D_{2D-s}Cf \end{aligned} \quad (2.38)$$

Here, D_{2D-s} is a diagonal matrix:

$$D_{2D-s} = \text{diag} \left[e^{j\phi_{2D-s}(1)}, e^{j\phi_{2D-s}(2)}, \dots, e^{j\phi_{2D-s}(S)} \right] \quad (2.39)$$

2.2.3 1D Phase Errors

We mentioned before that most encountered phase errors are functions of cross-range only. In other words, for a particular cross-range position the phase error is the same at all range positions. Let ϕ_{1D} be the 1D cross-range varying phase error. ϕ_{1D} is a vector of length M :

$$\phi_{1D} = \left[\phi_{1D}(1), \phi_{1D}(2), \dots, \phi_{1D}(M) \right]^T \quad (2.40)$$

In the case of 1D phase errors, the relationship between the error-free and the phase-corrupted data can be expressed as:

$$\begin{aligned} r_\epsilon &= D_{1D}r \\ C(\phi_{1D})f &= D_{1D}Cf \end{aligned} \quad (2.41)$$

Here, D_{1D} is a $S \times S$ diagonal matrix defined as:

$$D_{1D} = \text{diag} \left[\underbrace{e^{j\phi_{1D}(1)}, \dots, e^{j\phi_{1D}(1)}}_K, \underbrace{e^{j\phi_{1D}(2)}, \dots, e^{j\phi_{1D}(2)}}_K, \dots, \underbrace{e^{j\phi_{1D}(M)}, \dots, e^{j\phi_{1D}(M)}}_K \right] \quad (2.42)$$

These relationships can also be stated as follows:

$$\begin{aligned} \bar{r}_{\epsilon_m} &= e^{j\phi_{1D}(m)}\bar{r}_m \\ \bar{C}_m(\phi_{1D})f &= e^{j\phi_{1D}(m)}\bar{C}_m f \quad \text{for } m = 1, 2, \dots, M \end{aligned} \quad (2.43)$$

Here, \bar{r}_m and \bar{C}_m are the error-free phase history data and the assumed model matrix for the m -th cross-range position. Note that, in a 1D cross-range phase error case, there are M unknowns, in a 2D separable phase error case there are $M + K$ unknowns, and in a 2D non-separable phase error case there are $S = MK$ unknowns. Hence, correcting for 2D non-separable phase errors is a much more difficult problem than the others.

2.3 Existing Autofocus Techniques

2.3.1 Conventional Approaches

Inverse Filtering

Inverse filtering technique uses the amount of defocus on a single point target to estimate phase errors. Before we mentioned that the implication of 1D phase errors

in the image domain is the convolution of (each range line of) the image with a 1D blurring kernel in the cross-range direction. Mathematically, this can be expressed as follows:

$$\tilde{F}(a, b) = \tilde{h}(b) \otimes F(a, b) \quad (2.44)$$

where

$$\tilde{h}(b) = IFFT_m \{e^{j\phi(m)}\} \quad (2.45)$$

Here, \tilde{F} denotes the defocused image, and a and b are range and cross-range image domain indices, respectively. \otimes denotes circular convolution operation and m is the cross-range index in the frequency domain. Inverse filtering approach is based on the assumption that a single point target can be isolated in the defocused image. This technique estimates phase errors by finding such an isolated strong point target in the defocused image and then using the defocus information on that point target.

Let us consider a simple scenario in which only a single point target exists at the center of the scene. In this case, the corresponding image can be expressed as

$$F(a, b) = \kappa \delta(a, b) \quad (2.46)$$

where

$$\begin{aligned} \delta(a, b) &= 1 \quad \text{if } b = 0 \quad a = 0 \\ \delta(a, b) &= 0 \quad \text{if } b \neq 0 \quad a \neq 0 \end{aligned} \quad (2.47)$$

κ denotes the complex point target reflectivity. According to this image model, the defocused image becomes

$$\begin{aligned} \tilde{F}(a, b) &= \kappa IFFT_m \{e^{j\phi(m)}\} \otimes \delta(a, b) \\ &= \kappa IFFT_m \{e^{j\phi(m)}\} \end{aligned} \quad (2.48)$$

Now the phase error $\phi(m)$ can be obtained by taking the Fourier transform of the defocused image along the cross-range direction and then measuring its phase.

$$\begin{aligned} \hat{\phi}(m) &= \angle \left\{ FFT_b \left\{ \tilde{F}(a, b) \right\} \right\} \\ &= \angle \left\{ \kappa e^{j\phi(m)} \right\} \\ &= \angle \kappa + \phi(m) \end{aligned} \quad (2.49)$$

Here, $\angle\kappa$ is a constant phase and does not have any effect. By multiplying the phase-corrupted data with the complex conjugate of the phase error estimate, the phase error is removed:

$$\hat{R}(k, m) = R_\epsilon(k, m) e^{-j\hat{\phi}(m)} \quad (2.50)$$

Although inverse filtering technique is a simple and fast approach to phase error estimation, in practice it may be very difficult to find such an isolated strong point target in the SAR images. Generally there are other point targets and clutter in the environment surrounding it.

Subaperture-based Techniques

These techniques use the data from subapertures to estimate phase errors. These techniques are also known as map-drift autofocus techniques. The main assumption of these techniques is that the phase error function is a polynomial.

For a quadratic phase error function of the form $\phi(m) = \eta m^2$, where m is the index for cross-range (aperture) position and η is an unknown coefficient, these techniques first divide the data from the whole aperture into two pieces so that each subaperture data contains half of the quadratic phase error. Since half of a quadratic phase error includes a linear component as displayed in Figure 2.6, and since a linear phase error function only shifts the image proportional to its slope, the two low-resolution defocused images reconstructed from the two subaperture data are shifted versions of the original image in reverse directions. For every π radians of peak quadratic phase error, images are shifted by one pixel. By cross-correlating the two low-resolution images and finding the location of maximum correlation, the amount of shift and consequently the coefficient η can be determined.

2.3.2 Phase Gradient Autofocus (PGA)

The basic idea of Phase Gradient Autofocus (PGA) [3] is similar to inverse filtering but in contrast to inverse filtering, PGA estimates the phase error function by averaging across many range lines, based on the fact that every target in the image is corrupted by the same blur function. This averaging operation is performed within the formalism of maximum likelihood estimation. PGA is a non-parametric

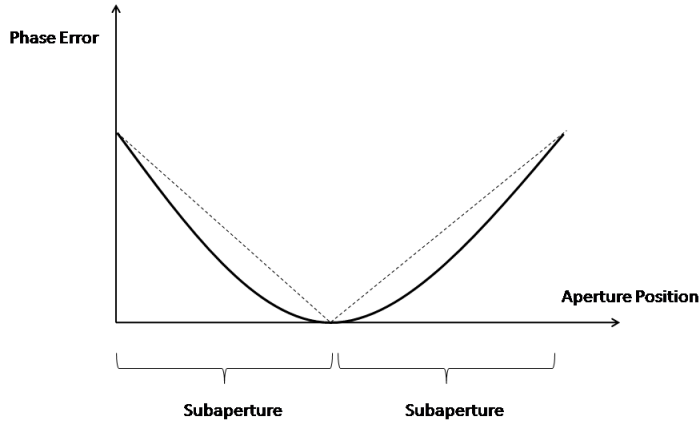


Figure 2.6: Linear components of a quadratic phase error function

technique unlike map-drift autofocus techniques. For phase error estimation, the algorithm aims to isolate a number of single targets in the image. Isolation of single targets is performed via center shifting and windowing operations. Since using the targets with strong reflectivities provides a much better phase error estimation than using the targets with weak reflectivities, PGA selects the strongest target on each range line and circularly shifts it to the scene center. At the end of this shifting operation a new image is obtained. All of the targets which will be used in the estimation process, lie in the center of the cross-range dimension of this new image. PGA includes a windowing operation in the next step, the purpose of which is to preserve the information contained in the blur footprints of the center-shifted targets and at the same time to reject information from all other surrounding targets with weak reflectivities. After center-shifting, the necessary information, contained in the support of the blur footprint, is extracted through windowing. The important part of this windowing operation is to determine the window width. If the window width is selected smaller than the blur footprint then some part of the necessary information cannot be captured. On the other hand, if the window width is wider than the blur footprint then the noise level increases. There are multiple ways to determine the window width. In the first approach, the window width is determined by summing the magnitudes of pixels in the circularly shifted image along the range

direction for every cross-range position as follows:

$$s(b) = \sum_{a=1}^A |F(a, b)|^2 \quad (2.51)$$

Here, a and b represent range and cross-range indices in the image domain, respectively. A is the total number of range lines. $s(b)$ will have its maximum at the center and will exhibit a plateau having approximately the same width as the blur footprint [3]. It is expected that the $s(b)$ significantly decreases outside the plateau. Therefore, the borders of this plateau-like region can be used to determine the window width. For this purpose, $s(b)$ is thresholded at some level, which is typically selected as 10dB lower than the peak. This approach for determining the window width is mostly suitable for slowly varying, particularly quadratic, phase error functions. Since these types of errors broaden the main lobe of the point target response, they cause a regular blur footprint, in which the strength of the reflectivity decreases smoothly in the direction from the center to the two sides. However, since rapidly varying phase error functions (e.g., random) raise the sidelobes of the impulse response function, they cause contrast-loss in the image, which means that the target energy is spread through the entire image along the cross-range. Therefore, the first approach used to determine the window width is not suitable for these types of errors. In this case, a progressive windowing scheme where the window width is reduced at each iteration by a pre-determined rate, is used instead [3]. Once the window width is selected and the windowing operation is performed. Then, by taking the 1D Fourier transform of each range line, the range-compressed data Y_w for the center-shifted and windowed image, used for phase error estimation, is obtained. The phase error is estimated by taking the phase differences between two successive pulses and the phase difference is estimated with a maximum likelihood scheme as follows [3]:

$$\Delta\hat{\phi}(m) = \angle \sum_{a=1}^A \{Y_w^*(a, m-1)Y_w(a, m)\} \quad (2.52)$$

Here, $Y_w^*(a, m-1)$ is the complex conjugate of $Y_w(a, m-1)$. After all $\Delta\phi(m)$ values are obtained, the phase error for the particular cross-range position is found by summing $\Delta\hat{\phi}(m)$ values up to that cross-range position as follows:

$$\hat{\phi}(m) = \sum_{j=2}^m \Delta\hat{\phi}(j) \quad \hat{\phi}(1) = 0 \quad (2.53)$$

The degraded range-compressed data is corrected via multiplying it by the complex conjugate of the phase error estimate as follows:

$$Y_c(a, m) = Y_\epsilon(a, m)e^{-j\hat{\phi}(m)} \quad (2.54)$$

Here, $Y_c(a, m)$ is the corrected data. Then by taking 1D inverse Fourier transform of each range line, the corrected range-compressed data is transformed back to the image domain. All of these steps are repeated until the root mean square value of the estimated incremental phase error function in any iteration is less than a pre-determined threshold. The flow for the algorithm of PGA is shown in Figure 2.7 [3].

2.3.3 Autofocus Techniques based on the Optimization of the Sharpness Metrics of the Defocused Image Intensity

There are many autofocus techniques which optimize various sharpness metrics on the conventionally reconstructed defocused image intensity. The intensity of each pixel for a 2D image is defined as

$$\ell(a, b) = |F(a, b)|^2 \quad (2.55)$$

Commonly used metrics are square or entropy of the image intensity, which are shown in (2.56) and (2.57) respectively.

$$\mu_s = - \sum_a \sum_b \ell(a, b)^2 \quad (2.56)$$

$$\mu_e = - \sum_a \sum_b \ell(a, b) \ln \ell(a, b) \quad (2.57)$$

The phase-error estimate is found by following an optimization routine for minimizing the particular sharpness metric. If we let $\Gamma[\ell(a, b)]$ be a function of image intensity and μ be a general sharpness metric, μ can be expressed as follows:

$$\mu = \sum_a \sum_b \Gamma[\ell(a, b)] \quad (2.58)$$

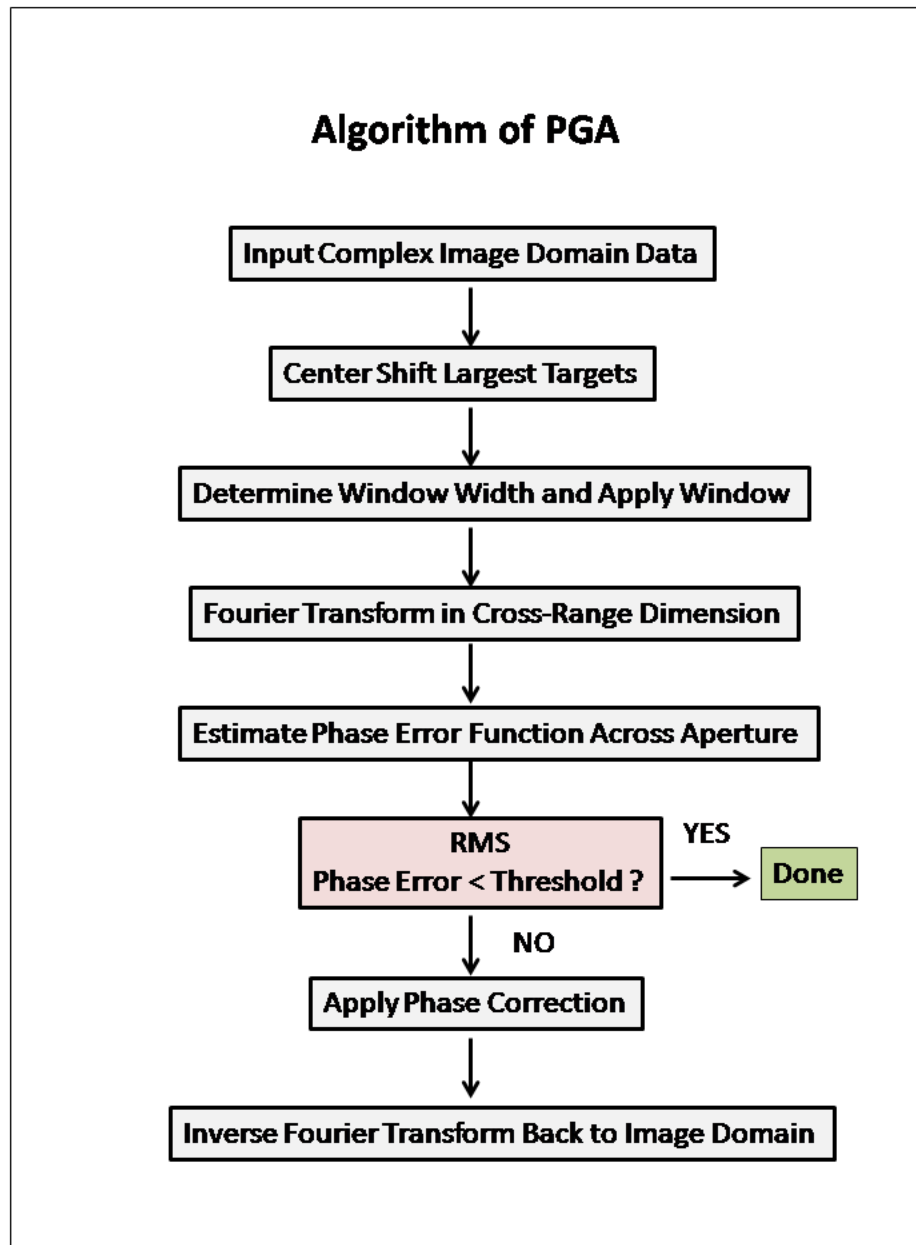


Figure 2.7: Algorithm of PGA

Then the gradient of this metric with respect to the phase error can be computed as follows [7]:

$$\frac{\partial \mu}{\partial \phi(m)} = \sum_a \sum_b \frac{\partial \Gamma [\ell(a, b)]}{\partial \ell(a, b)} \frac{\partial \ell(a, b)}{\partial \phi(m)} \quad (2.59)$$

where

$$\frac{\partial \ell(a, b)}{\partial \phi(m)} = \frac{|F(a, b)|^2}{\partial \phi(m)} = (2/B) \text{Im} [F^*(a, b)Y(a, m)e^{j2\pi mb/B}] \quad (2.60)$$

Here, $F^*(a, b)$ is the complex conjugate of $F(a, b)$ and $Y(a, m)$ is the range-compressed data. Regarding Equation (2.60), the relation in (2.59) can be expressed as:

$$\frac{\partial \mu}{\partial \phi(m)} = (2/B) \sum_a \text{Im} \left[Y(a, m) \left\{ FT \left[F(a, b) \frac{\partial \Gamma}{\partial \ell(a, b)} \right] \right\}^* \right] \quad (2.61)$$

The partial derivatives for $\Gamma [\ell(a, b)] = \ell(a, b)^2$ and for $\Gamma [\ell(a, b)] = \ell(a, b) \ln \ell(a, b)$ are given in (2.62) and in (2.63), respectively.

$$\frac{\partial \Gamma [\ell(a, b)]}{\partial \ell(a, b)} = 2\ell(a, b) \quad (2.62)$$

$$\frac{\partial \Gamma [\ell(a, b)]}{\partial \ell(a, b)} = \ln \ell(a, b) + 1 \quad (2.63)$$

After the phase error is estimated, the range-compressed data are corrected using this estimate.

2.3.4 Multi-Channel Autofocus (MCA)

In the SAR autofocus problem, each range line of the image is defocused by the same 1D blurring kernel. To solve the autofocus problem, Multi-Channel Autofocus (MCA) uses this multichannel structure, displayed in Figure 2.8 with a graphical illustration. The rows $F^{[a]}$ can be viewed as a bank of parallel filters which are circularly convolved with the same input signal $\tilde{h}(b)$. This fact can be mathematically expressed as

$$\tilde{F} = H \left\{ \tilde{h} \right\} F \quad (2.64)$$

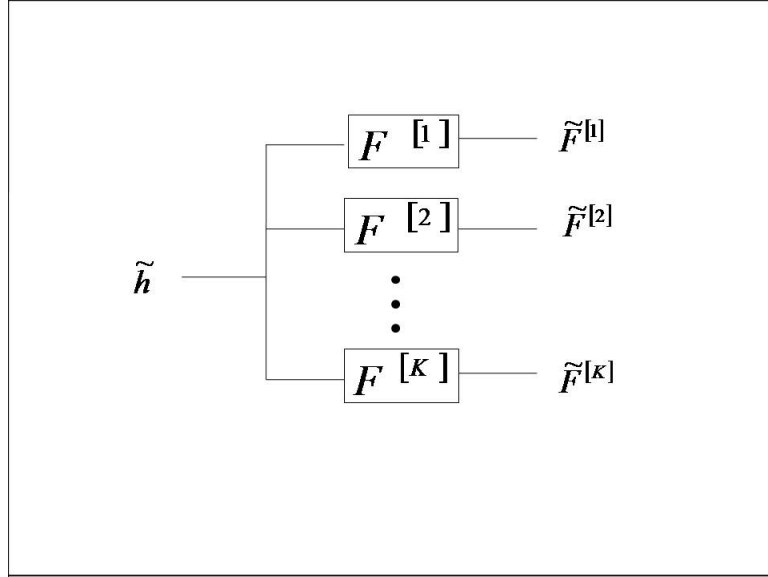


Figure 2.8: Graphical illustration of the multi-channel nature of the SAR autofocus problem.

where \tilde{F} and F are the defocused and focused images, respectively and $H \{ \tilde{h} \}$ is a circulant matrix of the following form:

$$H \{ \tilde{h} \} = \begin{bmatrix} \tilde{h} [0] & \tilde{h} [M-1] & \dots & \tilde{h} [1] \\ \tilde{h} [1] & \tilde{h} [0] & \dots & \tilde{h} [2] \\ \vdots & \vdots & \ddots & \vdots \\ \tilde{h} [M-1] & \tilde{h} [M-2] & \dots & \tilde{h} [0] \end{bmatrix} \quad (2.65)$$

Likewise, the solution space of the problem can be mathematically expressed as:

$$\hat{F}(h) = H \{ h \} \tilde{F} \quad (2.66)$$

Here, h is the correction filter and \hat{F} is the restoration. The goal is to find h by creating a subspace for the focused image F , spanned by a basis constructed from the given defocused image \tilde{F} [14]. To create a basis using the defocused image, first the correction filter is expressed in terms of the standard basis $\{e_m\}_{m=0}^{M-1}$, i.e., $e_m[b] = 1$ if $m = b$, and 0 otherwise, as follows [14]:

$$h = \sum_{m=0}^{M-1} h_m e_m \quad (2.67)$$

Based on the linearity property of circular convolution, the following relation is obtained:

$$H \{h\} = \sum_{m=0}^{M-1} h_m H \{e_m\} \quad (2.68)$$

Consequently, any image \hat{F} in the subspace can be expressed in terms of a basis expansion as follows [14]:

$$\hat{F}(h) = \sum_{m=0}^{M-1} h_m \varphi^{[m]}(\tilde{F}) \quad (2.69)$$

where

$$\varphi^{[m]}(\tilde{F}) = H \{e_m\} \tilde{F}^T \quad (2.70)$$

In a matrix-vector multiplication form, the relationship in (2.69) can be written as

$$vec \left\{ \hat{F}(h) \right\} = \Psi(\tilde{F})h \quad (2.71)$$

where

$$\Psi(\tilde{F}) = \left[vec \left\{ \varphi^{[0]}(\tilde{F}) \right\}, vec \left\{ \varphi^{[1]}(\tilde{F}) \right\}, \dots, vec \left\{ \varphi^{[M-1]}(\tilde{F}) \right\} \right] \quad (2.72)$$

is the basis matrix and $vec \left\{ \hat{F}(h) \right\}$ denotes the vector obtained by concatenating columns of $\hat{F}(h)$. To obtain a unique solution the basis matrix $\Psi(\tilde{F})$ must have rank M . If all of the conditions are satisfied, the perfectly focused image in terms of the basis can be expressed as

$$vec \{F\} = \Psi(\tilde{F})h^* \quad (2.73)$$

where h^* is the true correction filter satisfying $\hat{F}(h^*) = F$. By imposing a constraint to the linear system in (2.71), the unknown correction filter h^* can be directly solved for. This constraint is obtained by the assumption that F is approximately zero-valued for some regions in the scene and this assumption can be mathematically expressed as follows:

$$F[a, b] = \begin{cases} F^\Omega[a, b], & \text{for } a, b \in \Omega \\ F^{\bar{\Omega}}[a, b], & \text{for } a, b \in \bar{\Omega} \end{cases} \quad (2.74)$$

Here, $F^\Omega[a, b]$ are low-return pixels and Ω is the set of low-return pixels. Similarly, $F^{\bar{\Omega}}[a, b]$ are the pixels with nonzero values and $\bar{\Omega}$ is the set of nonzero pixels (i.e.,

the complement of Ω). These nonzero pixels constitute the region of support (ROS). In practice, the desired image support condition can be achieved by exploiting the spatially limited illumination of the antenna beam, or by using prior knowledge of low-return regions in the image [14]. Regarding the low-return region, the relation in (2.73) can be expressed as follows:

$$\begin{bmatrix} \text{vec} \{ F^\Omega \} \\ \text{vec} \{ F^{\bar{\Omega}} \} \end{bmatrix} = \begin{bmatrix} \left\{ \Psi(\tilde{F}) \right\}_\Omega \\ \left\{ \Psi(\tilde{F}) \right\}_{\bar{\Omega}} \end{bmatrix} h^* \quad (2.75)$$

$\left\{ \Psi(\tilde{F}) \right\}_\Omega$ are the rows of $\Psi(\tilde{F})$ that correspond to the pixels in the low-return region and $\left\{ \Psi(\tilde{F}) \right\}_{\bar{\Omega}}$ are the rows of $\Psi(\tilde{F})$ that correspond to the unknown nonzero pixels in the region of support. When $\text{vec} \{ F^{\bar{\Omega}} \}$ is exactly zero, the correction filter h^* can be directly determined up to a scaling constant by solving the following equation.

$$\left\{ \Psi(\tilde{F}) \right\}_\Omega h = 0 \quad (2.76)$$

The solution \hat{h} is the unique vector spanning the nullspace of $\Psi_\Omega(\tilde{F})$ as follows [14]:

$$\hat{h} = \text{Null} \left(\Psi_\Omega(\tilde{F}) \right) = e h^* \quad (2.77)$$

Here, e is a complex constant. The phase error estimate which is used to correct the defocused image is the phase of the Fourier transform of \hat{h} .

$$\hat{\phi}[m] = -\angle \left(\text{DFT}_b \left\{ \hat{h}[b] \right\} \right) \quad (2.78)$$

When $|F^\Omega(a, b)| \neq 0$ or when there is an additive noise in the image, the solution \hat{h} cannot be obtained by solving for the nullspace of $\Psi_\Omega(\tilde{F})$. In this case, to find a solution, the singular value decomposition of $\Psi_\Omega(\tilde{F})$ is performed to obtain the vector that produces the minimum energy solution in the l_2 sense as follows:

$$\hat{h} = \arg \min_{\|h\|_2=1} \left\| \Psi_\Omega(\tilde{F}) h \right\|_2 \quad (2.79)$$

The solution is given by $\hat{h} = \tilde{V}^{[M]}$, in which $\tilde{V}^{[M]}$ denotes the right singular vector corresponding to the smallest singular value of $\Psi_\Omega(\tilde{F})$ [14]. It is important to note that a necessary condition for MCA to produce a unique and correct solution is as follows:

$$\text{rank} \left(F^{\bar{\Omega}} \right) \geq \frac{M-1}{M-\bar{M}} \quad (2.80)$$

Here, $M - \bar{M}$ is the number of low-return columns as seen in Figure 2.9.

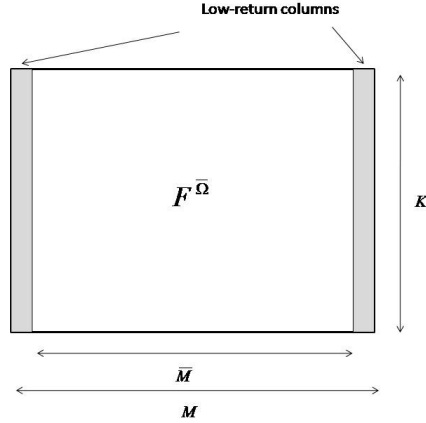


Figure 2.9: Region of support condition for MCA.

2.4 Regularization Based Image Reconstruction

In image reconstruction and restoration problems, the goal is to find an estimate of a 2D field from its indirect observations. From this point of view, image reconstruction and restoration problems can be regarded as general observation problems which we meet in most situations of engineering interest. Assuming that the mathematical relation between the observations and the field is obtained by a linear integral equation, in discrete form an observation system can be expressed as

$$g = Cf + v \quad (2.81)$$

where g and f are vectors of samples from observations and the field, respectively. C is the measurement model matrix and v is the measurement noise. To find an estimate \hat{f} of f looks simple and it seems that just multiplying the inverse of the matrix C with the observations vector g , is sufficient. However, there are four main problems that this approach can not handle. First, due to the observation noise, there may not exist any f which solves this equation exactly. Second, if the null-space of C is nonempty which means that there are not as many independent observations as unknowns, then the solution is not unique. Third, there is a stability problem. The estimate of f is desired to remain same despite the perturbations in the observations. The fourth issue is that the need to incorporate any prior knowledge of f to the solution [28].

2.4.1 Least Squares Solutions

To overcome the first problem, a reasonable approach is to find a least-squares solution. The solution is the best fit to the observed data in the least-squares sense.

$$\hat{f}_{ls} = \operatorname{argmin}_f \|g - Cf\|_2^2 \quad (2.82)$$

If C has full column rank, the estimate is unique and is obtained as

$$(C^T C)\hat{f}_{ls} = C^T g \quad (2.83)$$

When C does not have full column rank, which means that there is not a unique solution and that some components of f are not observable in g , the simple idea to find the estimate of f is to choose the one with minimum energy among all solution candidates. This solution is called generalized solution and defined as:

$$\hat{f}_{gen} = \operatorname{argmin}_f \|f\|_2^2 \quad \text{s.t.} \quad \min \|g - Cf\|_2^2 \quad (2.84)$$

However, this solution does not guarantee to reconstruct components of the image that are unobservable in the data. Another drawback of generalized solution is that it can not deal with stability problem. If the model matrix C is ill-conditioned (the ratio of the largest eigenvalue to the smallest is very large), small changes in the data lead to large changes in the solution. These problems are solved by using prior knowledge about the field f . This is known as ‘regularization’. Regularization provides stable and reasonable estimates of the field f .

2.4.2 Tikhonov Regularization

Tikhonov regularization is the well-known method for regularization. Incorporating of the prior knowledge of the field f is performed by including an additional term to the original least squares cost function.

$$\hat{f}_{tik} = \operatorname{argmin}_f \|g - Cf\|_2^2 + \lambda \|Df\|_2^2 \quad (2.85)$$

Here, the first term of the cost function provides the information in the data, whereas the second term, which is called side constraint, provides the prior knowledge of the field. λ is known as the regularization parameter which determines the weight of the prior knowledge in the estimation process. If D is chosen as identity matrix

then the side constraint becomes simply the energy of f , which prevents the pixel values of f from becoming too large. D can be chosen also as a derivative operator. In this case, the side-constraint forces the solution to have limited high-frequency content which means that the prior information included in the cost function forces the estimate to be smooth.

2.4.3 Nonquadratic Regularization

Many engineering problems admit a sparse representation in some domain. Let us consider an imaging problem, in which the field of interest is sparse, i.e., there are few nonzero pixels. In such a case, a solution with great energy concentration is needed. In Tikhonov regularization, we said that for D being an identity matrix, we obtain energy preserved solutions. However, experience has shown that non-quadratic side-constraints provides image reconstructions with greater energy concentration relative to quadratic Tikhonov approaches. There is a variety of non-quadratic choices to use as the sideconstraint. The general family of l_p -norms is one of them [28].

$$\|f\|_p = \left(\sum_{i=1}^N |f_i|^p \right)^{1/p} \quad (2.86)$$

In spectral analysis, l_p -norm constraints, where $p < 2$, have been shown to result in higher resolution spectral estimates compared to the l_2 -norm case. Moreover, smaller value of p implies less penalty on large pixel values as compared to larger p . Based on these observations, l_p -norm constraints with $p < 2$ are good choices to obtain sparse solutions.

From a statistical point of view, this problem corresponds to a maximum a posteriori (MAP) estimation problem as follows [23]:

$$\begin{aligned} \hat{f}_{MAP} &= \arg \max_f [\log (p_{f/g}(f/g))] \\ &= \arg \max_f [\log (p_{g/f}(g/f)) + \log (p_f(f))] \end{aligned} \quad (2.87)$$

Here, $\log (\cdot)$ denotes the natural logarithm. Maximizing the posterior density $p_{f/g}(f/g)$, or its logarithm are equivalent, due to the monotonicity property of the logarithm. Since the observation noise v is assumed to be independent identically distributed

(i.i.d.) Gaussian noise, the likelihood $p_{g/f}(g/f)$ can be described as follows:

$$p_{g/f}(g/f) \propto e^{(-\frac{1}{2\vartheta^2} \|g-Cf\|_2^2)} \quad (2.88)$$

Here, ϑ^2 is proportional to the noise power. Let the prior probability density function for the field f be given by:

$$p_f(f) \propto e^{(-\varphi\lambda^2 \|f\|_p^p)} \quad (2.89)$$

Substituting (2.88) and (2.89) into (2.87), and then converting the maximization to a minimization through a sign change, the MAP estimation problem can be written as follows [23]:

$$\hat{f}_{MAP} = \arg \min_f \left[\frac{1}{2\vartheta^2} \|g - Cf\|_2^2 + \varphi \left(\lambda^2 \|f\|_p^p \right) \right] \quad (2.90)$$

Letting $\varphi = \frac{1}{2\vartheta^2}$ the MAP estimation problem becomes the following:

$$\hat{f}_{MAP} = \arg \min_f \left[\|g - Cf\|_2^2 + \lambda^2 \|f\|_p^p \right] \quad (2.91)$$

If $p = 2$ is chosen, f is assumed to have a Gaussian distribution and if $p = 1$ is chosen then f is assumed to have a Laplacian distribution.

Chapter 3

Sparsity-Driven Autofocus (SDA)

In this chapter, we present our approach to the SAR autofocus problem and explain our technique, which we call sparsity-driven autofocus (SDA), in details. Moreover, we present experimental results on various synthetic scenes as well as on two public datasets provided by the U.S. Air Force Research Laboratory (AFRL): the ‘Slicy’ data from the ‘MSTAR’ dataset [29] and the ‘Backhoe’ dataset [30]. We also provide qualitative as well as quantitative results for comparison of our approach with three state-of-the-art autofocus techniques: Phase Gradient Autofocus (PGA), entropy minimization based autofocus, and Multi-channel Autofocus (MCA).

3.1 Principles and Development of SDA

In conventional imaging, the image is formed by interpolating the SAR phase history data (2.9) from the polar grid to a rectangular grid and then taking its 2D inverse Fourier transform. Images formed by conventional imaging usually suffer from speckle and sidelobe artifacts. Furthermore the resolution of the images is limited by the SAR system bandwidth. On the other hand, we know that regularization-based image formation techniques can deal with these problems and they have been successfully applied to SAR imaging. As explained in Section 2.4, these techniques formulate image formation as an optimization problem. The cost function is composed of a least-squares data fidelity term, as well as a side constraint or regularization term which incorporates information about the structure of the scene (sparsity, smoothness etc.) into the optimization problem. Incorporation of prior information

about the scene provides feature enhanced images with increased resolution, reduced sidelobes, and reduced speckle. In the context of SAR imaging of man-made objects, the underlying scene, dominated by strong metallic scatterers, is usually sparse, i.e., there are few nonzero pixels. To impose sparsity, often nonquadratic side constraints are incorporated into the cost function. There are a variety of nonquadratic terms to use as the side constraint. The general family of l_p -norms is one of them. Although l_0 -norm is in principle, the *right* choice to obtain sparse solutions, using l_0 -norm results in a combinatorial optimization problem. Therefore, generally, instead of l_0 -norm, l_p -norm of the field ($0 < p \leq 1$) is used to obtain sparse solutions. These types of constraints have been used in SAR imaging to obtain superresolution [31]. However, in most applications $p = 1$ is selected since using l_1 -norm of the field results in a convex optimization problem which is easier to solve. Moreover, recently it has been shown that under certain conditions, l_0 -norm and l_1 -norm yield identical solutions [32]. This observation has sparked much recent interest both in theory and in applications of sparse representations, coverage of which is beyond the scope of this dissertation.

Sparsity-driven radar imaging has already found use in a number of contexts [33–45]. In SAR applications, there is widespread use of sparsity-based imaging due to the advantages such as super-resolution and artifact suppression it provides. Such techniques assume that the observation model is known exactly. In the presence of phase errors and an additive measurement noise induced by the SAR system, as discussed in Section 2.2, the observation model becomes

$$g = C(\phi)f + v \tag{3.1}$$

where v stands for measurement noise, which is assumed to be white Gaussian noise (the most commonly used statistical model for radar measurement noise [46, 47]), and g is the noisy phase-corrupted observation data. Here, ϕ refers to one of the three types of phase errors introduced in Chapter 2.

Based on these observations we propose a nonquadratic regularization-based method for joint imaging and phase error correction. While existing sparsity-driven SAR imaging methods assume that data contain no phase errors, our approach jointly estimates and compensates such errors in the data, while performing sparsity-driven image formation. In particular, we pose the joint imaging and phase error

estimation problem as the problem of minimizing the following cost function:

$$J(f, \phi) = \|g - C(\phi)f\|_2^2 + \lambda \|f\|_1 \quad (3.2)$$

Here, λ is the regularization parameter, which specifies the strength of the contribution of the regularization term into the solution.

This is a difficult optimization problem over f and ϕ . Developing effective and efficient algorithms for such problems involves several research challenges. In this work, we propose and use a coordinate descent based numerical algorithm for solving this problem. The given cost function is minimized jointly with respect to f and ϕ . The algorithm is an iterative algorithm, which cycles through steps of image formation and phase error estimation and compensation. Every iteration involves two steps. In the first step, the cost function is minimized with respect to the field and in the second step the phase error is estimated given the field estimate. Before the algorithm passes to the next iteration, the model matrix is updated using the estimated phase error. This flow is outlined in Algorithm 1.

In Algorithm 1, n denotes the iteration number. $\hat{f}^{(n)}$ and $\hat{\phi}^{(n)}$ are the image and phase error estimates at iteration n , respectively. Note that the knowns in this algorithm are the noisy phase-corrupted data g and the initially assumed model matrix C . The unknowns are the field f and the phase error ϕ together with the associated model matrix $C(\phi)$ that takes the phase errors into account. It is worth noting here

Algorithm 1 Algorithm for the Proposed SDA Method

Initialize $n = 0$ $\hat{f}^{(0)} = C^H g$ and $C(\hat{\phi}^{(0)}) = C$

1. $\hat{f}^{(n+1)} = \arg \min_f J(f, \hat{\phi}^{(n)})$
2. $\hat{\phi}^{(n+1)} = \arg \min_\phi J(\hat{f}^{(n+1)}, \phi)$
3. Update $C(\hat{\phi}^{(n+1)})$ using $\hat{\phi}^{(n+1)}$ and C .
4. Let $n = n + 1$ and return to 1.

Stop when $\left\| \hat{f}^{(n+1)} - \hat{f}^{(n)} \right\|_2^2 / \left\| \hat{f}^{(n)} \right\|_2^2$ is less than a pre-determined threshold.

In this work, the value of the threshold is chosen as 10^{-3} .

that the use of the nonquadratic regularization-based framework contributes to the accurate estimation of the phase errors as well. Although nonquadratic regularization by itself cannot completely handle the kinds of phase errors considered in this work, it exhibits some robustness to small perturbations on the observation model

matrix [48]. In the context of our approach, the nonquadratic regularization term in the cost function provides a small amount of focusing of the estimated field in each iteration. This focusing then enables better estimation of the phase error. This in turn results in a more accurate observation model matrix, which provides better data fidelity and leads to a better field estimate in the next iteration.

Next, we provide the details of the algorithm for the three classes of phase errors described in Chapter 2.

3.1.1 Algorithm for 1D Phase Errors

In the algorithm for 1D phase errors, $\phi = \phi_{1D}$ as described in Section 2.2.3, in the first step of every iteration the cost function $J(f, \phi_{1D})$ is minimized with respect to f . This is the image formation step and same for all types of phase errors.

$$\hat{f}^{(n+1)} = \arg \min_f J(f, \hat{\phi}_{1D}^{(n)}) = \arg \min_f \left\| g - C(\hat{\phi}_{1D}^{(n)})f \right\|_2^2 + \lambda \|f\|_1 \quad (3.3)$$

To avoid problems due to nondifferentiability of the l_1 -norm at the origin, a smooth approximation is used [20]:

$$\|f\|_1 \approx \sum_{i=1}^I (|f_i|^2 + \sigma)^{1/2} \quad (3.4)$$

where σ is a nonnegative small constant. Here, note that the smaller σ is chosen the more the total number of iterations becomes since as σ decreases, the nondifferentiability increases. On the other hand, for big σ values, the approximation diverges from the l_1 -norm. In this work, σ is chosen as 10^{-5} .

In each iteration, the field estimate is obtained as

$$\hat{f}^{(n+1)} = \left(C(\hat{\phi}_{1D}^{(n)})^H C(\hat{\phi}_{1D}^{(n)}) + \lambda W(\hat{f}^{(n)}) \right)^{-1} C(\hat{\phi}_{1D}^{(n)})^H g \quad (3.5)$$

where $W(\hat{f}^{(n)})$ is a diagonal matrix:

$$W(\hat{f}^{(n)}) = \text{diag} \left[\frac{1}{(|\hat{f}_i^{(n)}|^2 + \sigma)^{1/2}} \dots \dots \dots \frac{1}{(|\hat{f}_I^{(n)}|^2 + \sigma)^{1/2}} \right] \quad (3.6)$$

The matrix inversion in (3.5) is not carried out explicitly, but rather numerically through the conjugate gradient algorithm. Note that, this algorithm has been used

in a variety of settings for sparsity-driven radar imaging, and has been shown to be a descent algorithm [49].

The second step involves phase error estimation, in which a different procedure is implemented for each type of phase errors. For 1D cross-range varying phase errors, given the field estimate, the following cost function is minimized for every cross-range position [50, 51],

$$\begin{aligned}\hat{\phi}_{1D}^{(n+1)}(m) &= \arg \min_{\phi_{1D}(m)} J(\hat{f}^{(n+1)}, \phi_{1D}(m)) \\ &= \arg \min_{\phi_{1D}(m)} \left\| \bar{g}_m - e^{(j\phi_{1D}(m))} \bar{C}_m \hat{f}^{(n+1)} \right\|_2^2 \quad \text{for } m = 1, 2, \dots, M\end{aligned}\quad (3.7)$$

where $\hat{\phi}_{1D}^{(n+1)}(m)$ denotes the phase error estimate for the cross-range position m in the iteration $(n + 1)$. In (3.7), the $K \times 1$ vector \bar{g}_m is the noisy SAR data at the $m - th$ cross-range position. After evaluating the norm expression in (3.7) (see appendix for details), we obtain

$$\begin{aligned}\hat{\phi}_{1D}^{(n+1)}(m) &= \arg \min_{\phi_{1D}(m)} \left(\bar{g}_m^H \bar{g}_m - 2\sqrt{\Re^2 + \Im^2} \cos \left[\phi_{1D}(m) + \arctan \left(\frac{-\Im}{\Re} \right) \right] \right. \\ &\quad \left. + \hat{f}^{(n+1)H} \bar{C}_m^H \bar{C}_m \hat{f}^{(n+1)} \right)\end{aligned}\quad (3.8)$$

where

$$\Re = \text{Re} \left\{ \hat{f}^{(n+1)H} \bar{C}_m^H \bar{g}_m \right\} \quad \Im = \text{Im} \left\{ \hat{f}^{(n+1)H} \bar{C}_m^H \bar{g}_m \right\}\quad (3.9)$$

We know that negative cosine has its minimum at zero and integer multiples of 2π , so if we set the argument of the cosine to zero, we can find the phase error estimate in closed form as given in (3.10) for the corresponding aperture position.

$$\hat{\phi}_{1D}^{(n+1)}(m) = -\arctan \left(\frac{-\Im}{\Re} \right)\quad (3.10)$$

Using the phase error estimate, the model matrix is updated as follows:

$$\bar{C}_m(\hat{\phi}_{1D}^{(n+1)}(m)) = e^{(j\hat{\phi}_{1D}^{(n+1)}(m))} \bar{C}_m \quad \text{for } m = 1, \dots, M\quad (3.11)$$

We increment n and turn back to the optimization problem in (3.3).

Moreover, note that, phase updates are performed after each step of the iteration in (3.5), as a result of which, the overall computational load of our approach is not significantly more than that of just image formation.

3.1.2 Algorithm for 2D Separable Phase Errors

In case of 2D separable phase errors, the field estimate is obtained via minimizing the following cost function:

$$\hat{f}^{(n+1)} = \arg \min_f J(f, \hat{\phi}_{2D-s}^{(n)}) = \arg \min_f \left\| g - C(\hat{\phi}_{2D-s}^{(n)})f \right\|_2^2 + \lambda \|f\|_1 \quad (3.12)$$

Given the field estimate, first, the phase error in the cross-range direction, γ , is estimated by minimizing the following cost function using the 1D phase error estimation procedure described in Section 3.1.1:

$$\hat{\gamma}(m)^{(n+1)} = \arg \min_{\gamma(m)} J(\hat{f}^{(n+1)}, \gamma(m)) = \arg \min_{\gamma(m)} \left\| \bar{g}_m - e^{(j\gamma(m))} \bar{C}_m \hat{f}^{(n+1)} \right\|_2^2$$

for $m = 1, 2, \dots, M$ (3.13)

Then this estimate is used to update the model matrix as follows:

$$\bar{C}_m(\hat{\gamma}(m)^{(n+1)}) = e^{(j\hat{\gamma}(m)^{(n+1)})} \bar{C}_m \quad \text{for } m = 1, 2, \dots, M \quad (3.14)$$

Then, to estimate the phase error in the range direction, the elements of the data vector g and the rows of the model matrix $C(\hat{\gamma}^{(n+1)})$ are ordered in such a way that the elements and rows corresponding to the same range position lie under each other. Let these modified data vector and modified model matrix be g_{mod} and C_{mod} , respectively (i.e., the phase history matrix is row-stacked rather than column-stacked). Using these new variables, the phase error estimate $\hat{\xi}$ for the range direction is found repeating the same procedure as in cross-range direction, this time for every range position. This can be expressed as follows:

$$\hat{\xi}(k)^{(n+1)} = \arg \min_{\xi(k)} J(\hat{f}^{(n+1)}, \xi(k)) = \arg \min_{\xi(k)} \left\| \bar{g}_{mod_k} - e^{(j\xi(k))} \bar{C}_{mod_k} \hat{f}^{(n+1)} \right\|_2^2$$

for $k = 1, 2, \dots, K$ (3.15)

$$\bar{C}_{mod_k}(\hat{\xi}(k)^{(n+1)}) = e^{(j\hat{\xi}(k)^{(n+1)})} \bar{C}_{mod_k} \quad \text{for } k = 1, 2, \dots, K \quad (3.16)$$

Here, \bar{g}_{mod_k} and \bar{C}_{mod_k} represent the parts of g_{mod} and C_{mod} corresponding to a particular range position k , respectively. To return to the original form, the rows of the matrix $C_{mod}(\hat{\xi}^{(n+1)})$ are rearranged so that the rows corresponding to the same cross-range position lie under each other. This rearranged matrix is denoted by $C(\hat{\phi}_{2D-s}^{(n+1)})$ which is used in the next iteration to find the next field estimate.

3.1.3 Algorithm for 2D Non-separable Phase Errors

In a more general case in which we consider 2D non-separable phase errors, the image formation step of the algorithm is essentially identical to its counterpart in previous cases. To obtain the field estimate, the following cost function is minimized with respect to f .

$$\hat{f}^{(n+1)} = \arg \min_f J(f, \hat{\phi}_{2D-ns}^{(n)}) = \arg \min_f \left\| g - C(\hat{\phi}_{2D-ns}^{(n)})f \right\|_2^2 + \lambda \|f\|_1 \quad (3.17)$$

Using the same point of view as in the previous two cases, in the phase error estimation step, the following cost function is minimized [51, 52].

$$\begin{aligned} \hat{\phi}_{2D-ns}^{(n+1)}(s) &= \arg \min_{\phi_{2D-ns}(s)} J(\hat{f}^{(n+1)}, \phi_{2D-ns}(s)) \\ &= \arg \min_{\phi_{2D-ns}(s)} \left\| g(s) - e^{(j\phi_{2D-ns}(s))} C_s \hat{f}^{(n+1)} \right\|_2^2 \quad \text{for } s = 1, 2, \dots, S \end{aligned} \quad (3.18)$$

Here, $\hat{\phi}_{2D-ns}^{(n+1)}(s)$ denotes the phase error estimate for the s -th data sample in iteration $(n+1)$. This step is solved in closed form in a similar way to that in (3.7).

In particular, the solution of the optimization problem in (3.18) is as follows:

$$\hat{\phi}_{2D-ns}^{(n+1)}(s) = -\arctan\left(\frac{-\Im}{\Re}\right) \quad (3.19)$$

where

$$\Re = \text{Re} \left\{ \hat{f}^{(n+1)H} C_s^H g(s) \right\} \quad \Im = \text{Im} \left\{ \hat{f}^{(n+1)H} C_s^H g(s) \right\} \quad (3.20)$$

Using the phase error estimate, the model matrix is updated through:

$$C_s(\hat{\phi}_{2D-ns}^{(n+1)}(s)) = e^{(j\hat{\phi}_{2D-ns}^{(n+1)}(s))} C_s \quad \text{for } s = 1, \dots, S \quad (3.21)$$

If the phase error type (i.e., 1D, 2D separable, or 2D nonseparable) is known, then it is natural to use the corresponding version of the proposed algorithm for best phase error estimation performance. If the phase error type is not known *a priori*, then the version of our algorithm for the 2D nonseparable case can be used, since this is the most general scenario. For any of these three types of phase errors, our algorithm does not require any knowledge about how the phase error function varies (randomly, quadratically, polynomially, etc.) along the range (in 2D cases) or cross-range (in 1D and 2D cases) directions. We demonstrate the effectiveness of our approach on data corrupted by various phase error functions.

Table 3.1: SAR System Parameters used in the synthetic scene experiment whose results are shown in Figures 3.1 and 3.2.

carrier frequency (ω_0)	$2\pi \times 10^{10} \text{ rad/s}$
chirp rate (2α)	$2\pi \times 10^{12} \text{ rad/s}^2$
pulse duration (T_{pulse})	$4 \times 10^{-4} \text{ sec.}$
angular range ($\Delta\theta$)	2.3°

3.2 Experimental Results

We have applied the proposed SDA method in a number of scenarios and present our results in the following two subsections. In Section 3.2.1 we present our results on various types of data and demonstrate the improvements in visual image quality as compared to the uncompensated case. In Section 3.2.2 we provide a quantitative comparison of our approach with existing state-of-the-art autofocus techniques.

3.2.1 Qualitative Results and Comparison to the Uncompensated Case

To present qualitative results for the proposed method in comparison to the uncompensated case, several experiments have been performed on various synthetic scenes as well as on two public SAR data sets provided by the U.S. Air Force Research Laboratory (AFRL): the Slicy data, part of the MSTAR dataset [29]; and the Backhoe data [30].

To generate synthetic SAR data for a 32×32 scene we have used a SAR system model with the parameters given in Table 3.1. The resulting phase history data lie on a polar grid. As observation noise, complex white Gaussian noise is added to the data so that SNR is 30dB. We have performed experiments for four different types of phase errors. The original synthetic image is shown in Figure 3.1(a). For the data without phase errors, conventional and sparsity-driven reconstructions are given in Figure 3.1(b) and (c), respectively. In this paper, in all of the experiments, the polar-format algorithm is used for conventional imaging. Results by conventional imaging and by the proposed method for different types of phase errors are shown

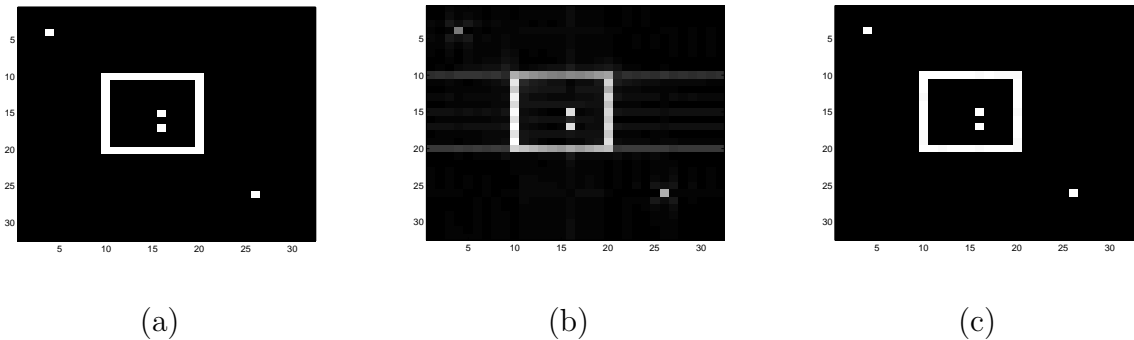


Figure 3.1: (a) The original scene. (b) Conventional imaging from the data without phase errors. (c) Sparsity-driven imaging from the data without phase errors.

in Figure 3.2. Conventionally reconstructed images suffer from degradation due to phase errors. The results show the effectiveness of the proposed method. As seen in Figure 3.2, it is not possible to visually distinguish the images formed by the proposed method from the original scene.

To demonstrate the performance of SDA in the presence of speckle, we present some results on a 128×128 synthetic scene, in Figure 3.3. To create speckle, random phase is added to the reflectivities of the underlying scene. The corresponding SAR data are simulated by taking a 32×32 band-limited segment from the 2D Fourier transform of the scene. Then a 1D cross-range varying random phase error, uniformly distributed in $[-\pi, \pi]$ has been added to the data. Speckle is clearly visible in the conventional image reconstructed from the data without phase errors in Figure 3.3(a). The images reconstructed by conventional imaging and sparsity-driven imaging when the data are corrupted by phase errors are shown in Figures 3.3(b) and (c), respectively. The result in Figure 3.3(d) demonstrates that SDA can effectively perform imaging and phase error compensation in the presence of speckle.

In Figure 3.4 we present the images reconstructed from the Slicy data without phase errors. The Slicy target is a precisely designed and machined engineering test target containing multiple simple geometric radar reflector static shapes. The data used in the experiments have been collected with a squint angle of 330° . Figure 3.4 (a) shows the photo of the Slicy target, Figure 3.4(b) shows the image reconstructed conventionally and Figure 3.4(c) shows the result of sparsity-driven imaging. As seen in the figures, sparsity-driven imaging provides high resolution images with

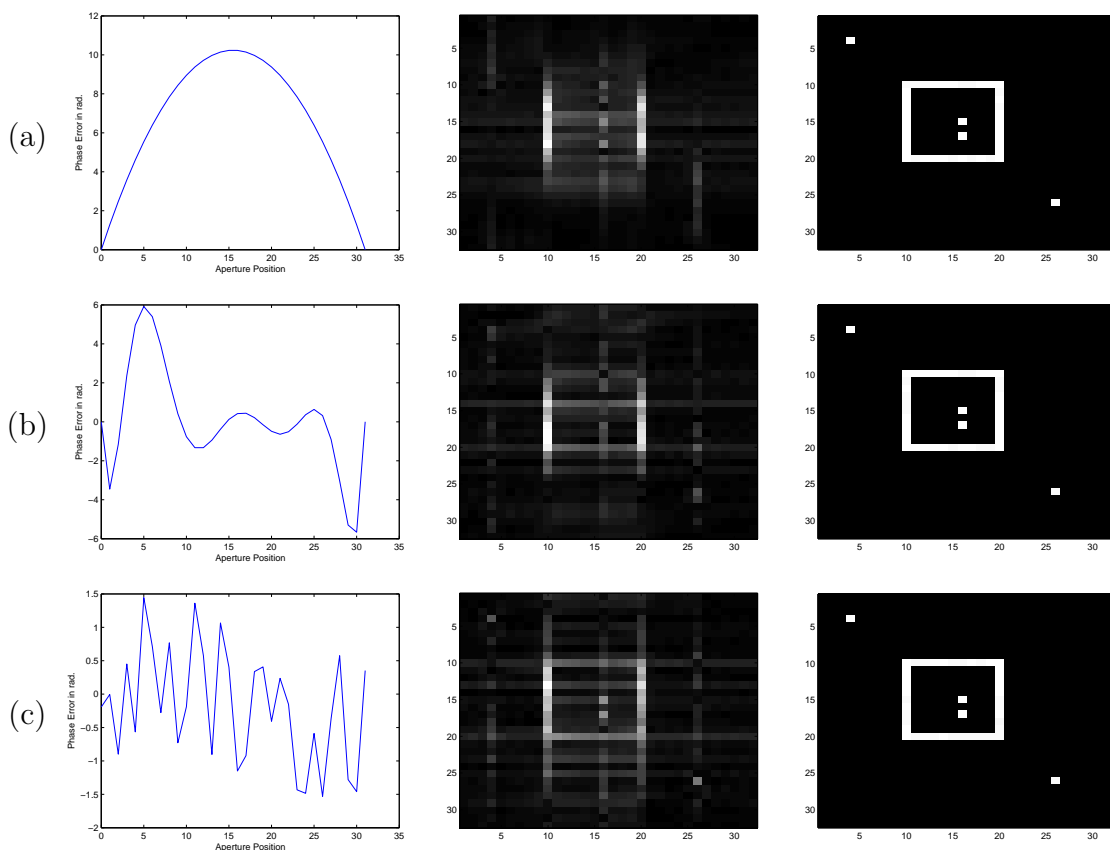
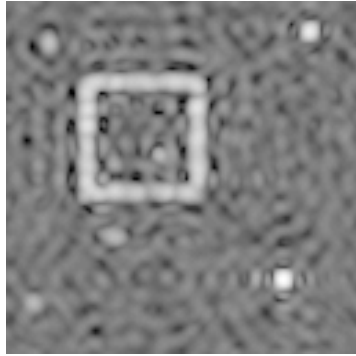
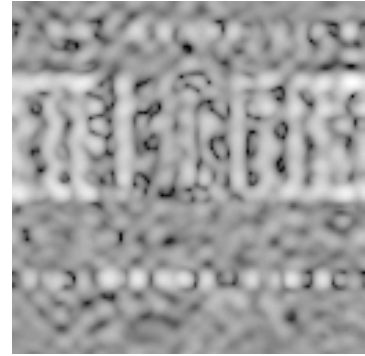


Figure 3.2: Left- Phase error. Middle- Images reconstructed by conventional imaging. Right- Images reconstructed by the proposed SDA method. (a) Results for quadratic phase error. (b) Results for an 8th order polynomial phase error. (c) Results for a phase error uniformly distributed in $[-\pi/2, \pi/2]$.

enhanced features (in this particular example, this means locations of dominant point scatterers). Figure 3.5(a) and (b) show the results on the Slicy data for a 1D quadratic and a 1D random phase error which is uniformly distributed in $[-\pi, \pi]$. The images in the middle row correspond to direct application of the sparsity-driven imaging technique of [20] without model error compensation. The significant degradation in the reconstructions show that sparsity-driven imaging without model error compensation cannot handle phase errors. From the images presented in the bottom row we can see clearly that the images formed by the proposed SDA method inherit and exhibit the advantages of sparsity-driven imaging (see Figure 3.4(c)) and in the meantime the phase errors are removed as well. In Figure 3.6(a) and (b), the results for 2D separable and non-separable random phase errors are displayed. 2D phase



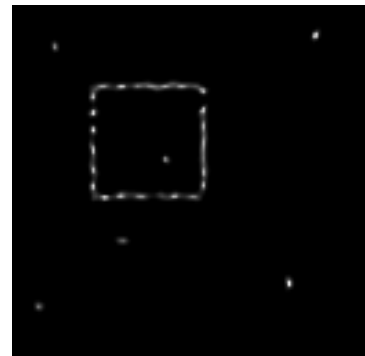
(a)



(b)



(c)

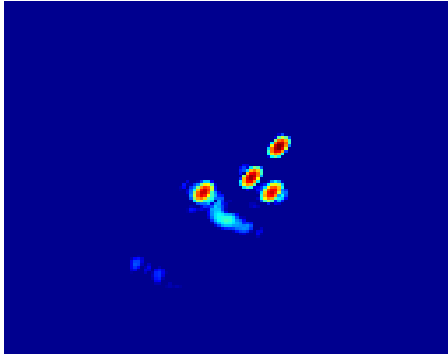


(d)

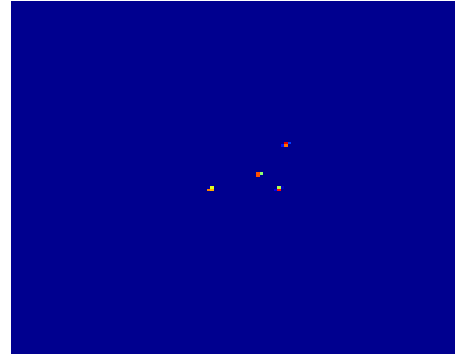
Figure 3.3: Experimental results on a speckled scene. (a) Conventional image reconstructed from noisy data without phase error. (b) Conventional image reconstructed from noisy data with phase error. (c) Image reconstructed by sparsity-driven imaging from noisy data with phase error. (d) Image reconstructed by the proposed SDA method.



(a)



(b)



(c)

Figure 3.4: (a) Photo of the Slicy target. (b) Conventional imaging from the data without phase error. (c) Sparsity-driven imaging from the data without phase error.

errors cause a dramatic degradation on the reconstructed images. However, the proposed SDA method successfully corrects the 2D phase errors as well, and produces images that exhibit accurate localization of the true scatterers and significant artifact suppression.

Here, note that, it is possible to estimate a 2D separable phase error function by using the algorithm for 2D non-separable phase errors. However, we know that a 2D separable phase error function has a structure and to obtain the two 1D phase error functions separately we need to use this structure information during the estimation process since it is difficult to separate a 2D phase error function into 1D phase error functions due to the nonuniqueness. In the previous experiments for 2D separable

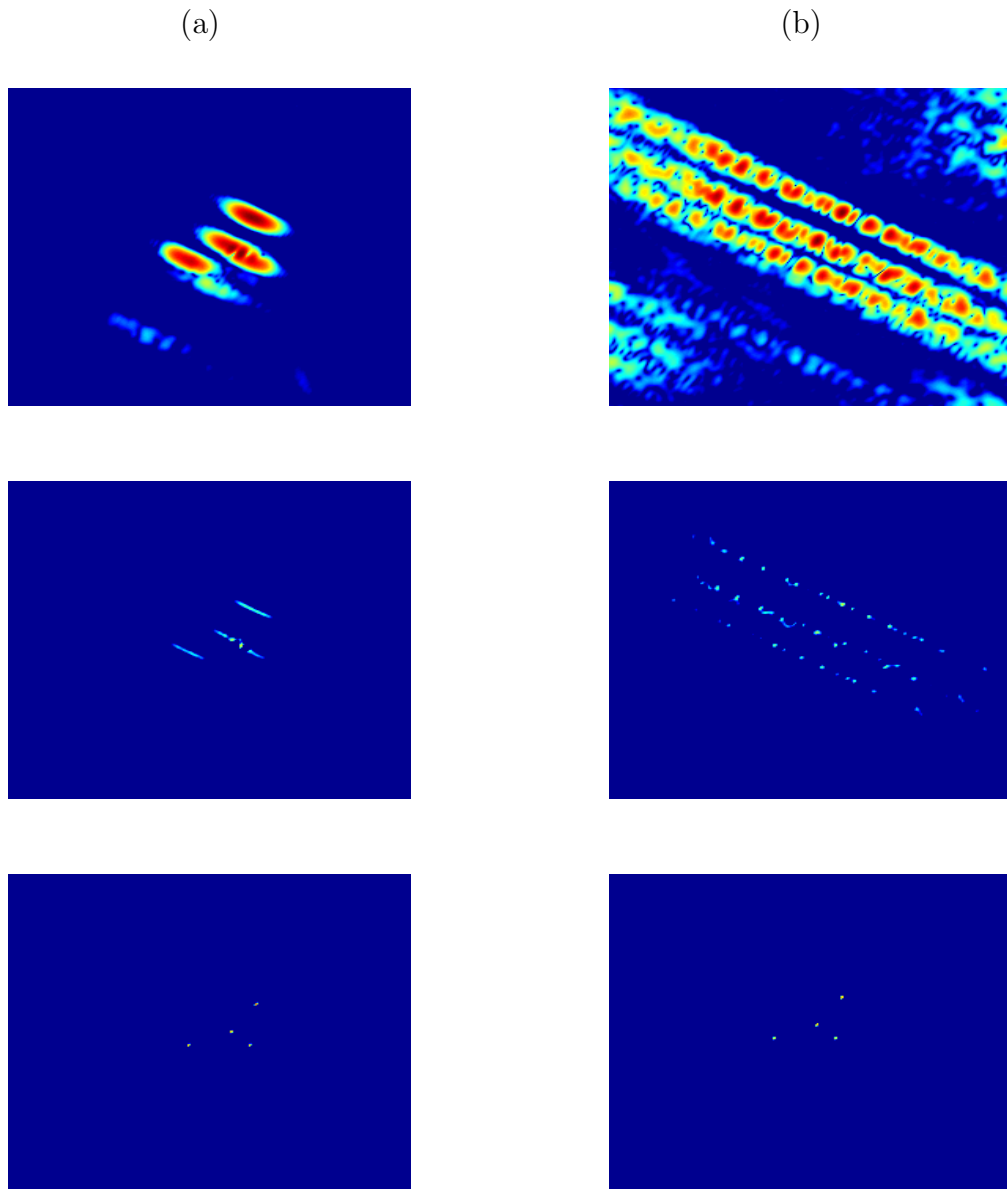


Figure 3.5: Top- Images reconstructed by conventional imaging. Middle- Images reconstructed by sparsity-driven imaging. Bottom- Images reconstructed by the proposed SDA method. (a) Results for a 1D quadratic phase error. (b) Results for a 1D phase error uniformly distributed in $[-\pi, \pi]$.

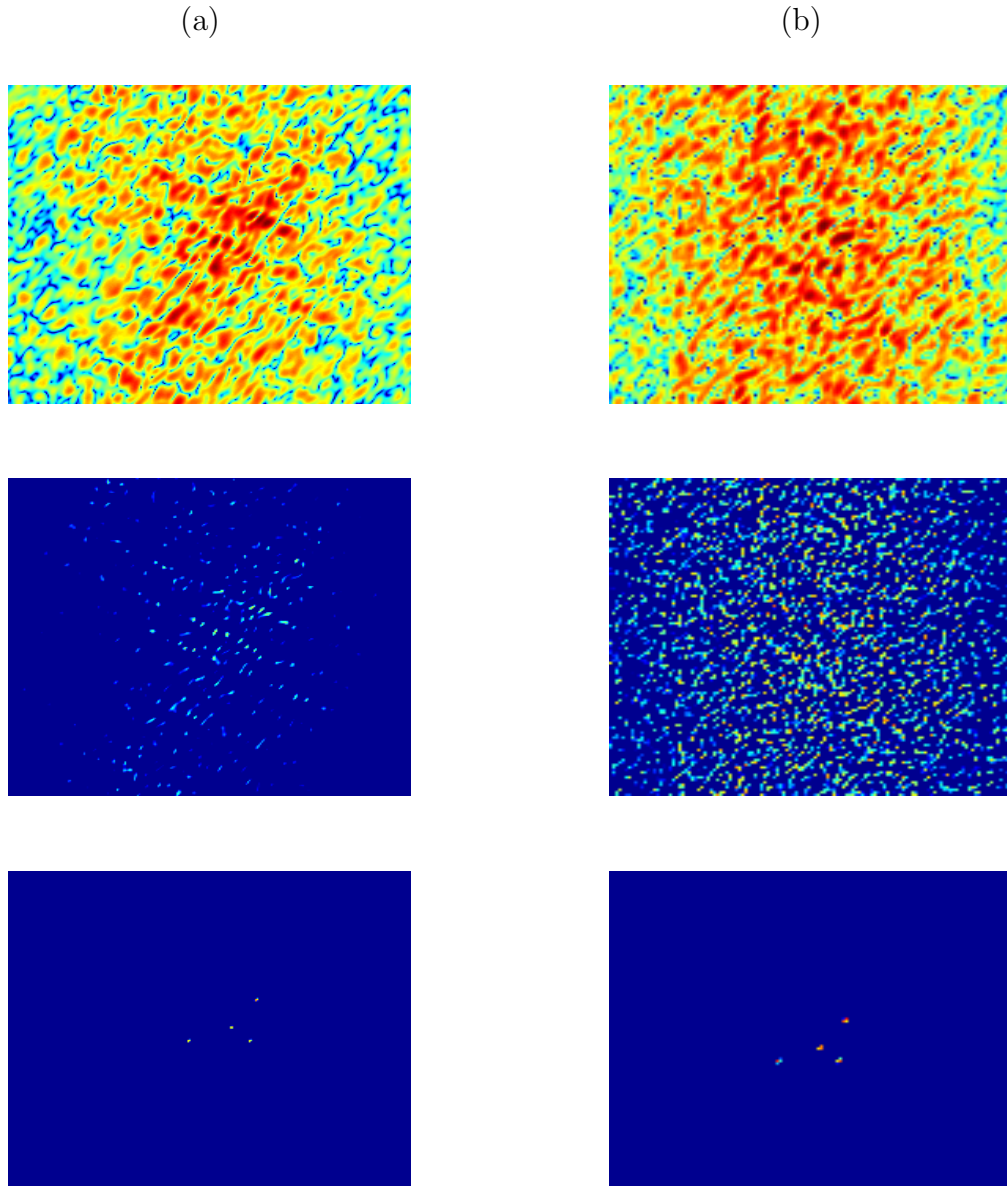


Figure 3.6: Top- Images reconstructed by conventional imaging. Middle- Images reconstructed by sparsity-driven imaging. Bottom- Images reconstructed by the proposed SDA method. (a) Results for a 2D separable phase error composed of two 1D phase errors uniformly distributed in $[-3\pi/4, 3\pi/4]$. (b) Results for a 2D non-separable phase error uniformly distributed in $[-\pi, \pi]$.

phase errors, the phase error estimation is done as explained in Section 3.1.2, i.e., in every iteration first the phase error in the cross-range direction and then the phase error in the range direction is estimated and compensated. To get an intuition about whether the order of these estimation steps has any effect on the solution, we have performed an experiment. In this experiment, a 2D separable phase error composed of two 1D phase errors, one of which is uniformly distributed in $[-\pi, \pi]$ and the other is uniformly distributed in $[-\pi/2, \pi/2]$, has been applied to the Slicy data. Results, produced by using the original SDA algorithm for 2D separable phase errors, and the SDA algorithm with a phase error estimation step in reverse order, i.e., the phase error estimation is done first for the range direction and then for the cross-range direction, are displayed in Figure 3.7(b) and (c), respectively. In Figure 3.7(d) and (e), the difference between the phase error estimates of these two cases are shown for the cross-range and range dependent phase error functions, respectively. Based on the results of this experiment, it seems that changing the order of the phase error estimation does not have a remarkable effect on the performance of the algorithm. The phase error estimates for two cases are almost the same and the difference between these estimates is at most 0.0215 radians which is negligible. However, we acknowledge this is a limited experiment, and this issue can be examined more rigorously.

We present 2D image reconstruction experiments based on the AFRL ‘Backhoe Data Dome, Version 1.0’, which consists of simulated wideband (7-13 GHz), full polarization, complex backscatter data from a backhoe vehicle in free space, as well. The backscatter data are available over a full upper 2π steradian viewing hemisphere. In our experiments, we use VV polarization data, centered at 10 GHz, and with an azimuthal span of 110° . The data we use in our experiments have a bandwidth of 1 GHz. To deal with the wide-angle observation in the Backhoe dataset, we incorporate the subaperture-based composite imaging approach of [53] into our framework. The composite image is formed by combining the subaperture images so that each pixel value of the composite image is determined by selecting the maximum value for that pixel across the subaperture images. For this experiment, phase error estimation and correction are performed for every subaperture image. In Figure 3.8 we show the facet of the Backhoe vehicle and, the conventionally and

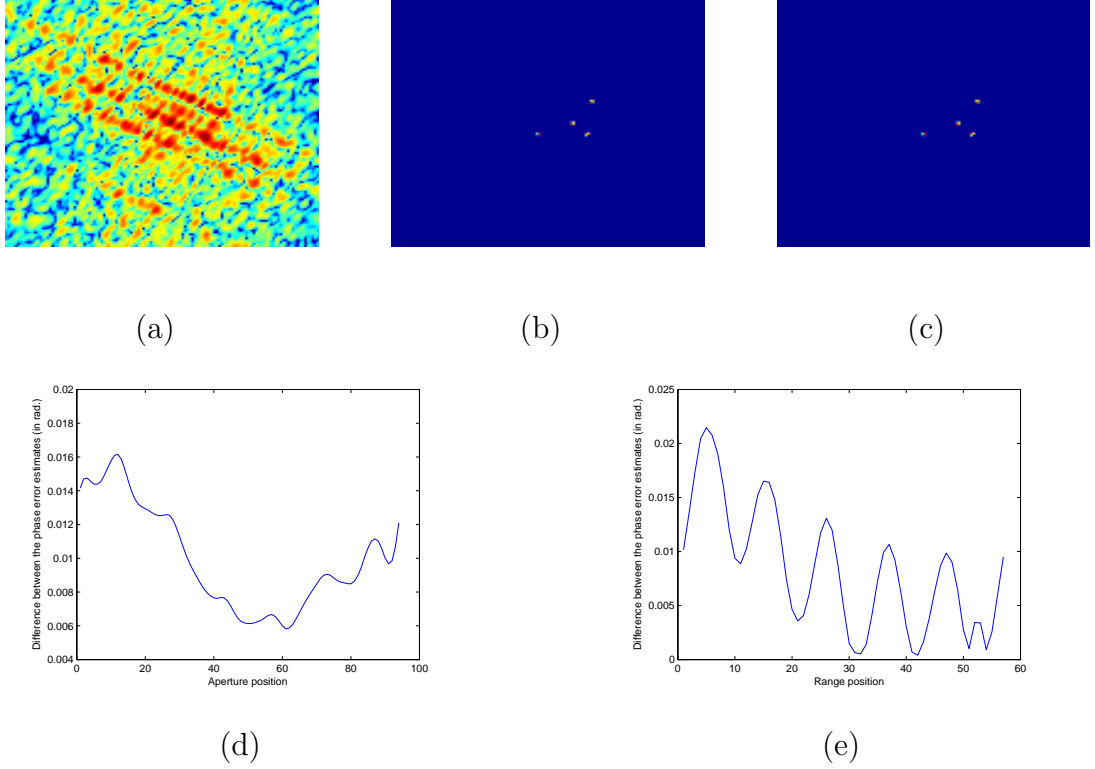
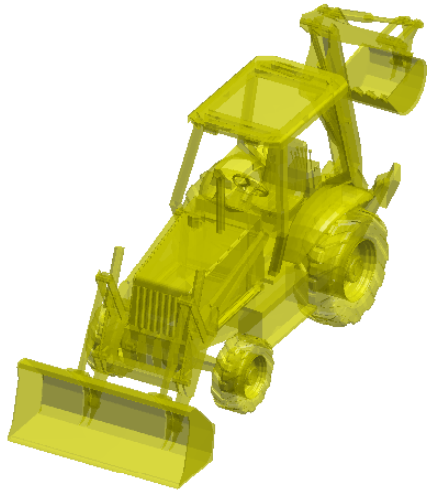


Figure 3.7: Results for a 2D separable phase error composed of two 1D phase errors, one of which is uniformly distributed in $[-\pi, \pi]$ and the other is uniformly distributed in $[-\pi/2, \pi/2]$. (a) Conventional imaging. (b) Image reconstructed by the proposed SDA method (the order of phase error estimation process: 1)for cross-range direction 2)for range direction). (c) Image reconstructed by the proposed SDA method (the order of phase error estimation process: 1)for range direction 2)for cross-range direction). (d) Difference between the cross-range dependent phase error estimates of two cases. (e) Difference between the range dependent phase error estimates of two cases.

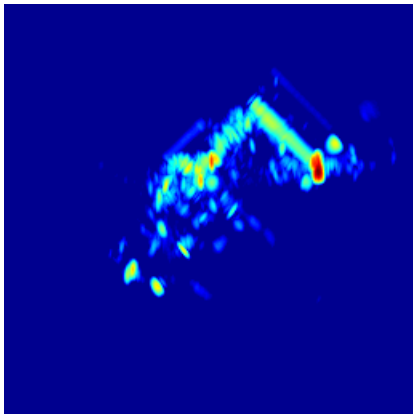
sparsity-driven reconstructed images for the data without phase error. The results on Backhoe data for 1D and 2D separable random phase errors are presented in Figure 3.9. In the top and middle rows of Figure 3.9, the artifacts due to phase errors are clearly seen in the images reconstructed by conventional imaging and sparsity-driven imaging, respectively. However, both 1D and 2D phase errors are compensated effectively by the proposed method. From the given examples so far we see that the proposed SDA method corrects the phase errors effectively and provides images with high resolution and reduced sidelobes, thanks to the nonquadratic regularization-based framework.

We mentioned that regularization-based imaging gives satisfying results in cases of incomplete data as well. We explore this aspect in the presence of phase errors performing two experiments on Slicy data with frequency band omissions. In the first experiment, the data from 30% of frequencies were randomly set to zero, i.e., only 70% of the spectral data within that bandwidth are available, and then a 1D random phase error function, uniformly distributed in $[-\pi, \pi]$ was applied to the data. The results of this experiment are presented in Figure 3.10 and Figure 3.11. In the second experiment, this time, data with 70% frequency band omissions were used and a 1D quadratic phase error function was applied to the data. The images of the second experiment are displayed in Figure 3.12 and Figure 3.13. As seen from the reconstructions, the proposed method produces feature-enhanced images and removes phase errors effectively even when the data are partially available.

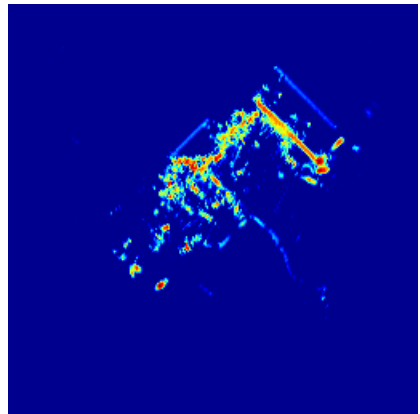
Now we want to demonstrate how the nonquadratic regularization functional in our framework supports phase error compensation, through a simple experiment in which we compare the results of our approach with a quadratic regularization scheme. In this experiment, we have applied a 1D cross-range varying random phase error, uniformly distributed in $[-\pi, \pi]$ to the data from a synthetic scene simulated just by taking its 2D Fourier transform. To construct a quadratic regularization-based scheme, we have replaced the l_1 - norm in our approach with an l_2 - norm without changing the phase error estimation piece. We present the results of this experiment in Figure 3.14. As seen from images, with the quadratic regularization approach, it is not possible to correct phase errors, whereas the image reconstructed by our nonquadratic regularization-based SDA algorithm is perfectly focused.



(a)



(b)



(c)

Figure 3.8: (a) The facet of the Backhoe vehicle. (b) Conventional imaging from the data without phase error. (c) Sparsity-driven imaging from the data without phase error.

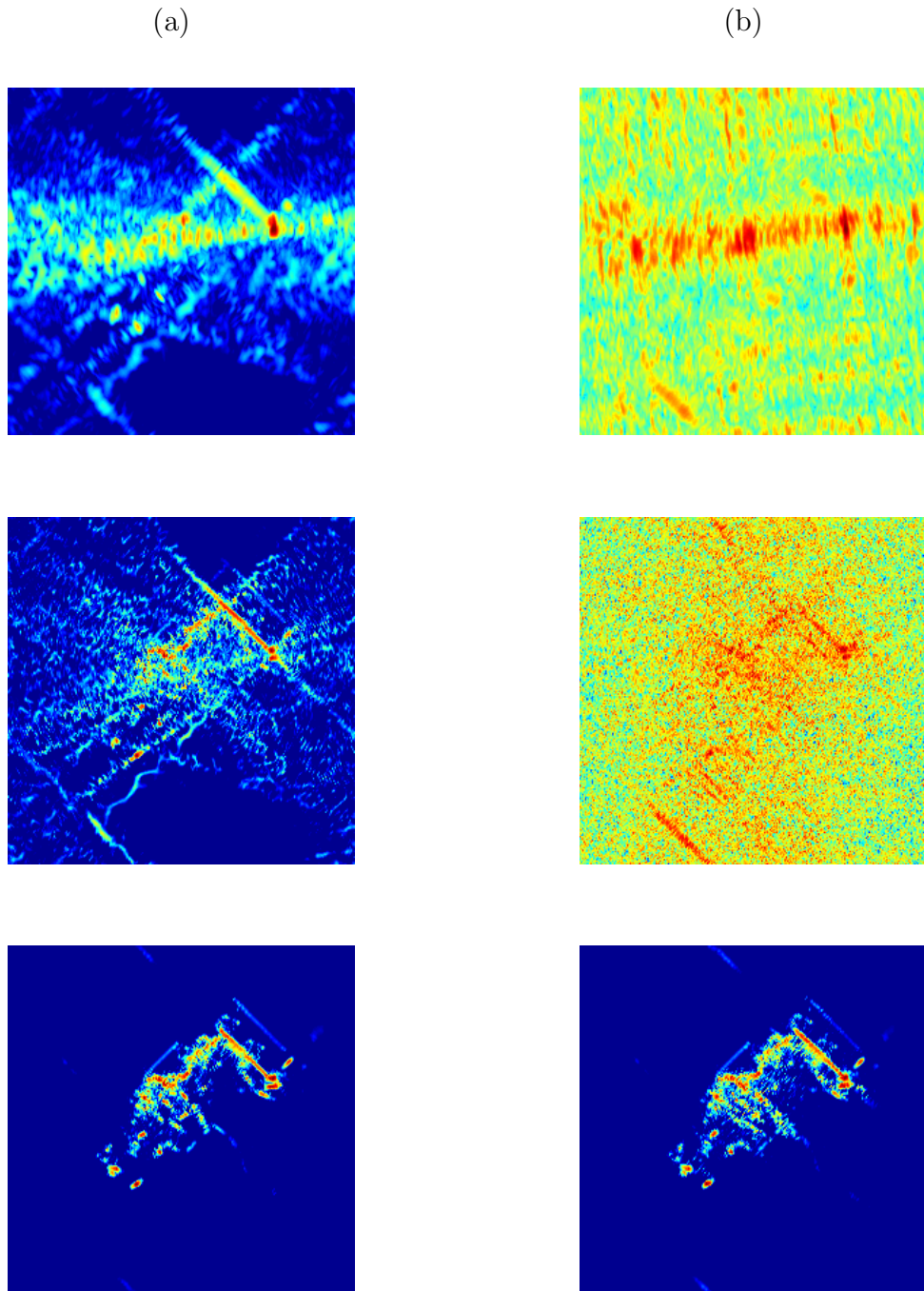
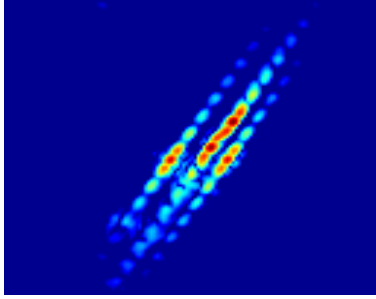
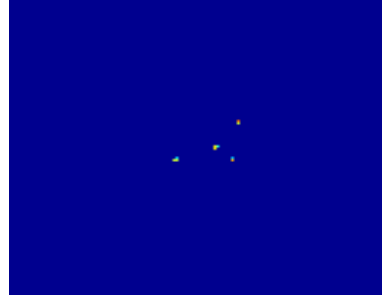


Figure 3.9: Top- Images reconstructed by conventional imaging. Middle- Images reconstructed by sparsity-driven imaging. Bottom- Images reconstructed by the proposed SDA method. (a) Results for a 1D phase error uniformly distributed in $[-\pi/2, \pi/2]$. (b) Results for a 2D separable phase error composed of two 1D phase errors uniformly distributed in $[-3\pi/4, 3\pi/4]$.

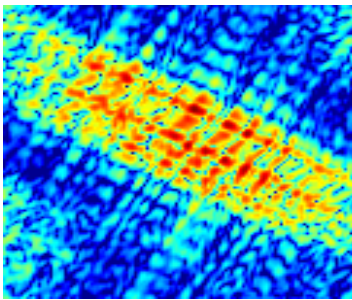


(a)

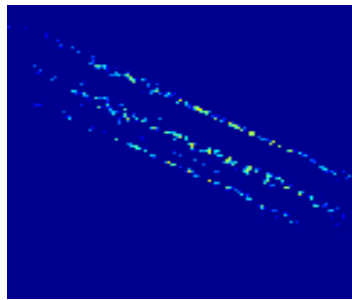


(b)

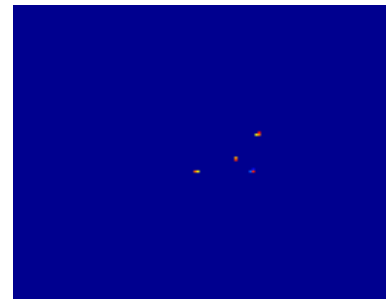
Figure 3.10: Experiments on the Slicy data with 30% frequency band omissions : (a) Conventional imaging from the data without phase error. (b) Sparsity-driven imaging from the data without phase error.



(a)

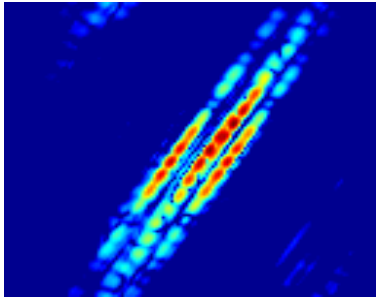


(b)

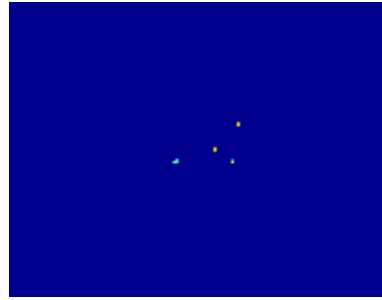


(c)

Figure 3.11: Experiments on the Slicy data with 30% frequency band omissions and 1D random phase error uniformly distributed in $[-\pi, \pi]$: (a) Conventional imaging. (b) Sparsity-driven imaging. (c) Proposed SDA method.

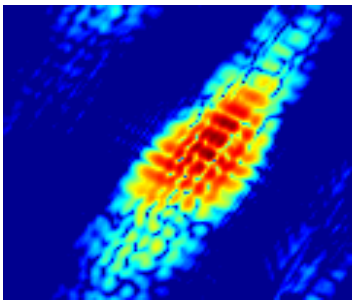


(a)

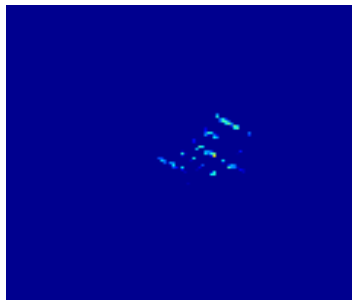


(b)

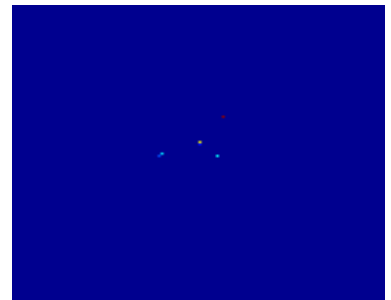
Figure 3.12: Experiments on the Slicy data with 70% frequency band omissions : (a) Conventional imaging from the data without phase error. (b) Sparsity-driven imaging from the data without phase error.



(a)

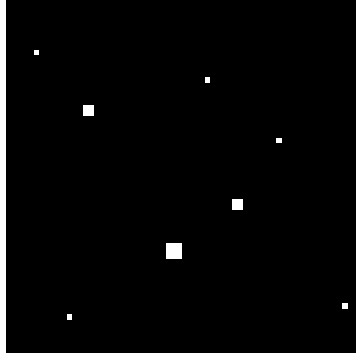


(b)

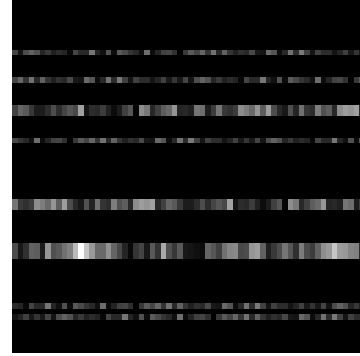


(c)

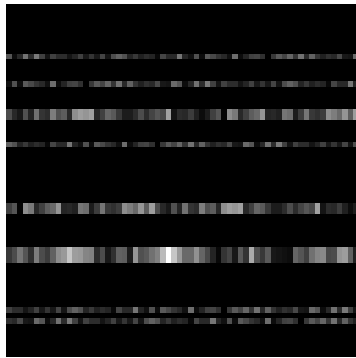
Figure 3.13: Experiments on the Slicy data with 70% frequency band omissions and 1D quadratic phase error: (a) Conventional imaging. (b) Sparsity-driven imaging (c) Proposed SDA method.



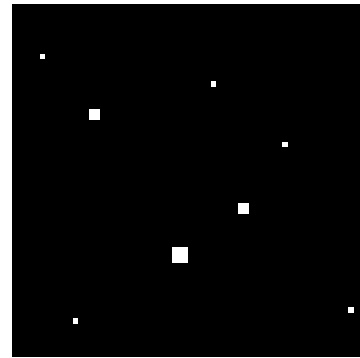
(a)



(b)



(c)



(d)

Figure 3.14: Results of the experiment for testing the effect of the nonquadratic regularization term in the proposed SDA method on phase error compensation. (a) The original scene. (b) Conventional imaging from the data with phase error. (c) Image reconstructed in the case of replacing the $l_1 - norm$ in our approach with an $l_2 - norm$ without changing the phase error estimation piece. (d) Image reconstructed by the proposed SDA method.

Before going to the next section, it is useful here to discuss the effect of the regularization parameter λ on the solution. To obtain satisfactory results, it is important to choose a proper regularization parameter. According to the size and the type of the data and the observation model and according to the noise-level, a different regularization parameter value needs to be selected. In this thesis, regularization parameters in all experiments are selected heuristically. Actually, there are many methods proposed for the automatic selection of the regularization parameter and they have been applied also to SAR imaging [54, 55]. These techniques can be integrated into our method to determine the regularization parameter automatically. However, since these techniques have been developed for regularization-based imaging with an observation model without any errors, they may not give the optimum result in the problems with model errors. These techniques may be integrated into our method in an adaptive way, i.e., in each iteration a new regularization parameter can be selected using the parameter selection techniques. Of course, using an automatic regularization parameter selection method would bring some extra computational load.

To give an idea of how the regularization parameter selection changes the solution, in Figure 3.15 we present results obtained for different λ values, from the noisy, phase-corrupted data of a 64×64 synthetic scene. In this experiment, the data have been obtained by taking the 2D FFT of the synthetic scene and as phase error, a 1D random phase error function, uniformly distributed in $[-\pi/2, \pi/2]$, has been applied. The input SNR is 16dB. For this experiment, we see that in terms of both phase error compensation and noise suppression, reasonable results have been obtained for λ values between 2.5 and 2000.

3.2.2 Quantitative Results in Comparison to State-of-the-art Autofocus Methods

In the second part of the experimental study, we present results for comparison of the proposed technique with existing autofocus techniques. In Figure 3.16 we show comparative results for a 64×64 synthetic scene. The SAR data are simulated by taking a band-limited segment on a rectangular grid from the 2D discrete Fourier

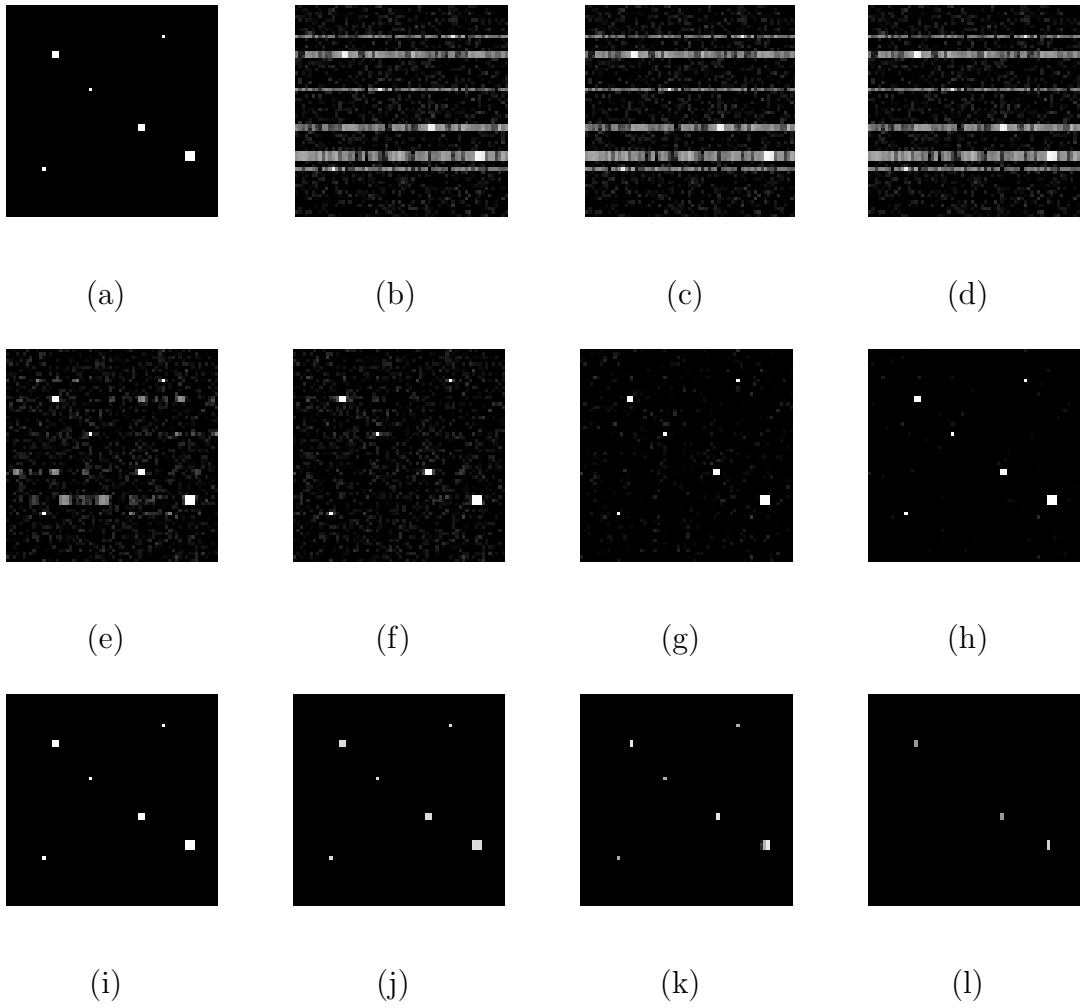


Figure 3.15: (a) The original scene. (b) Conventional imaging from noisy data with phase error. Results of the proposed SDA method for various regularization parameter (λ) values. (c) $\lambda = 0.5$. (d) $\lambda = 1$. (e) $\lambda = 1.5$. (f) $\lambda = 2.5$. (g) $\lambda = 25$. (h) $\lambda = 50$. (i) $\lambda = 100$. (j) $\lambda = 2000$. (k) $\lambda = 2500$. (l) $\lambda = 4000$.

transform (DFT) of the scene. Then complex white Gaussian noise is added to the data so that the input SNR is 10.85dB. Then a 1D cross-range varying random phase error, uniformly distributed in $[-\pi, \pi]$ is added to the data. The performance of the proposed technique is compared to the performance of PGA [4] and entropy minimization techniques [5, 7–9]. For entropy minimization we have used the procedure given in [7]. For this particular experiment, the results suggest that all three methods do a good job in estimating the phase error. However in terms of image quality, while PGA and entropy minimization are limited by conventional imaging, the proposed SDA method demonstrates the advantage of joint sparsity-driven imaging and phase error correction, and produces a scene that appears to provide a very accurate representation of the original scene. For the same synthetic scene we

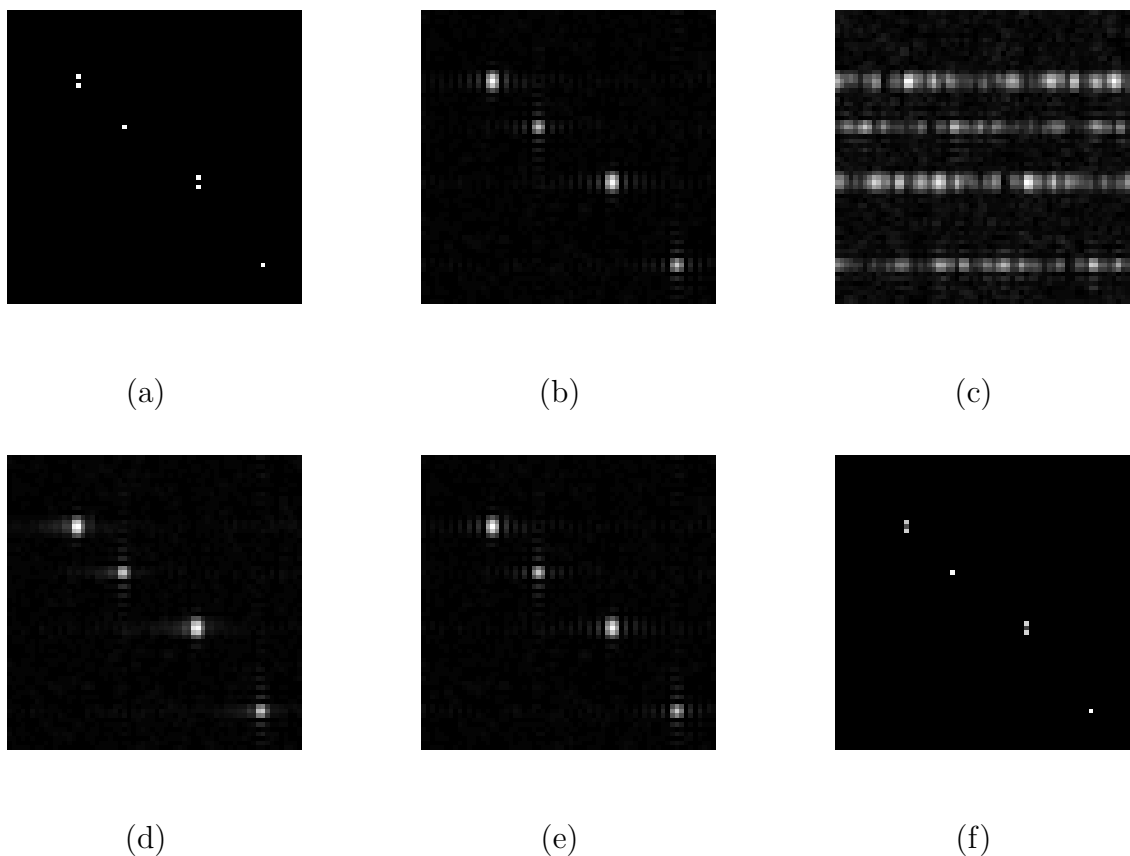


Figure 3.16: (a) The original scene. (b) Conventional imaging from noisy data without phase error. (c) Conventional imaging from noisy data with phase error. (d) Result of PGA. (e) Result of entropy minimization. (f) Result of the proposed SDA method.

have also performed experiments with different input SNRs. For each SNR value we have applied 20 different random 1D phase errors, all of them uniformly distributed in $[-\pi, \pi]$. For each experiment we compute 3 different metrics. These are the MSE between the original image and the image resulting from the application of the autofocus technique considered, target-to-background ratio, and metrics for the phase error estimation error. These metrics are computed as follows:

$$MSE = \frac{1}{I} \left\| |f| - |\hat{f}| \right\|_2^2 \quad (3.22)$$

Here, f and \hat{f} denote the original and the reconstructed images, respectively. I is the total number of pixels.

Target-to-background ratio is used to determine the accentuation of the target pixels with respect to the background:

$$TBR = 20 \log_{10} \left(\frac{\max_{i \in T} |\hat{f}_i|}{\frac{1}{I_B} \sum_{j \in B} |\hat{f}_j|} \right) \quad (3.23)$$

Here, T and B denote the pixel indices for the target and the background regions, respectively. I_B is the number of background pixels.

To compare the phase error estimation performance of the proposed method to other techniques, we first compute the estimation error for phase errors:

$$\phi_e = \phi - \hat{\phi} \quad (3.24)$$

Here ϕ_e is effectively the phase error that remains in the problem after correction of the data or the model using the estimated phase error. To evaluate various techniques based on their phase error estimation performance, it makes sense to first remove the components in ϕ_e that either have no effect on the reconstructed image, or that can be easily dealt with, and then perform the evaluation based on the remaining error. We first note that a constant (as a function of the aperture position) phase shift has no effect on the reconstructed image [3]. Second, a linear phase shift does not cause blurring, but rather a spatial shift in the reconstructed image. Such a phase error can be compensated by appropriate spatial operations on the scene [6], which we perform prior to quantitative evaluation. To disregard the effect of any constant phase shift in our evaluation, and also noting that the amount of variation of the phase error across the aperture is closely related to the degree of

degradation of the formed imagery, we propose using evaluation metrics based on the total variation (TV) of ϕ_e and on the l_2 - *norm* of the gradient of ϕ_e :

$$\begin{aligned} TV_{PE} &= \frac{1}{M-1} \|\nabla\phi_e\|_1 \\ MSE_{PE} &= \frac{1}{M-1} \|\nabla\phi_e\|_2^2 \end{aligned} \quad (3.25)$$

Here, $\nabla\phi_e$ is the $(M-1)\times 1$ vector, obtained by taking first-order differences between successive elements of ϕ_e . M is the total number of cross-range positions.

Now we get back to the quantitative evaluation of the reconstruction of the scene in Figure 3.16(a) for various SNRs. We present the comparison results for these three metrics in Figure 3.16. Since TV_{PE} and MSE_{PE} values are similar for these particular experiments, we show the results for MSE_{PE} only. From the plots presented, it is clearly seen that the proposed method performs better than the other techniques, especially for low SNR values. We also note in Figure 3.16(a) that the proposed SDA method yields much better performance in terms of the MSE between the original and the reconstructed images even at high SNRs. This is due to the fact that SDA benefits from the advantages of sparsity-driven imaging (unlike the other techniques) over conventional imaging (see Figure 3.16) in addition to successfully correcting the phase errors (like the other techniques) at high SNRs.

All of the three algorithms were implemented using non-optimized MATLAB code on an Intel Celeron 2.13GHz CPU. In the experiment of Figure 3.16, the computation times required by PGA, entropy minimization, and the proposed SDA method are 0.6240s, 1.1076s, and 2.1216s, respectively. For the experiments of Figure 3.17, Figure 3.18 and Figure 3.19, the average computation times for PGA, entropy minimization, and SDA are 0.3095s, 0.4719s, and 3.4961s, respectively. The computational load of SDA is relatively more than the other methods, but this can be justified through the benefits provided by the sparsity-driven imaging framework underlying SDA, as demonstrated in our experiments.

In Figure 3.20, we display some comparative results on the Backhoe data as well. For this experiment the applied 1D phase error is a random error with a uniform distribution in $[-\pi, \pi]$. In this example, for quantitative comparison, we use the MSE for the phase error. The MSE_{PE} values are shown in Table 3.2. The results show that the proposed method performs phase error estimation more accurately

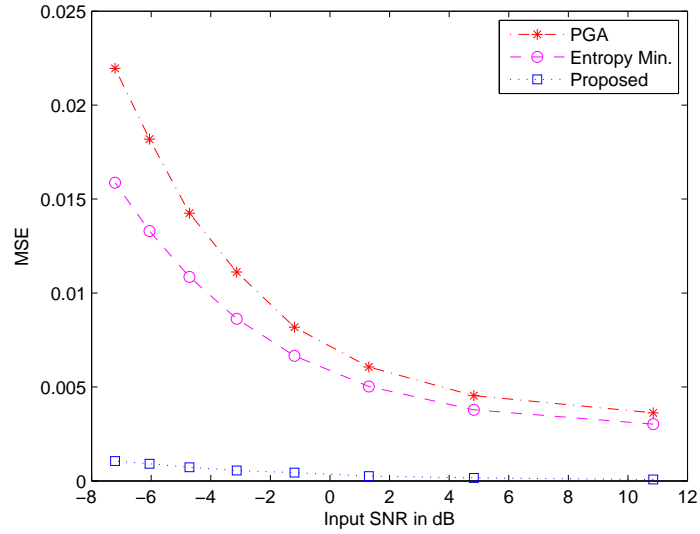


Figure 3.17: MSE evaluation of the reconstruction of the scene in Figure 3.14(a) for various SNRs. Each point on the curves corresponds to an average over 20 experiments with different random 1D phase errors uniformly distributed in $[-\pi, \pi]$.

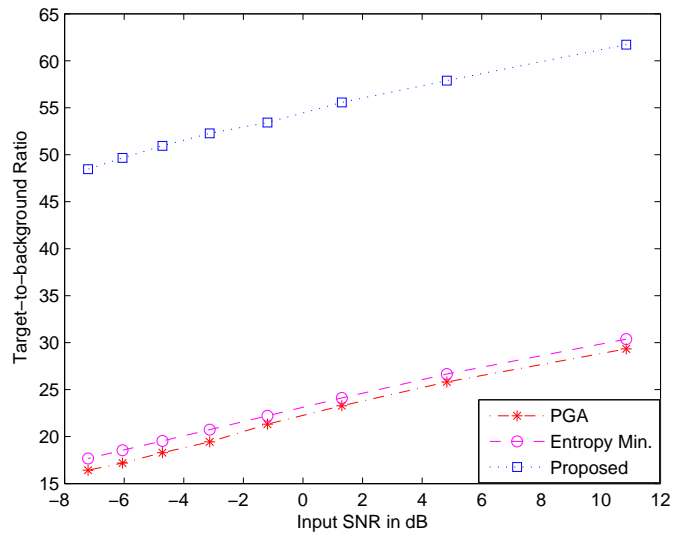


Figure 3.18: Target-to-background ratio evaluation of the reconstruction of the scene in Figure 3.14(a) for various SNRs. Each point on the curves corresponds to an average over 20 experiments with different random 1D phase errors uniformly distributed in $[-\pi, \pi]$.

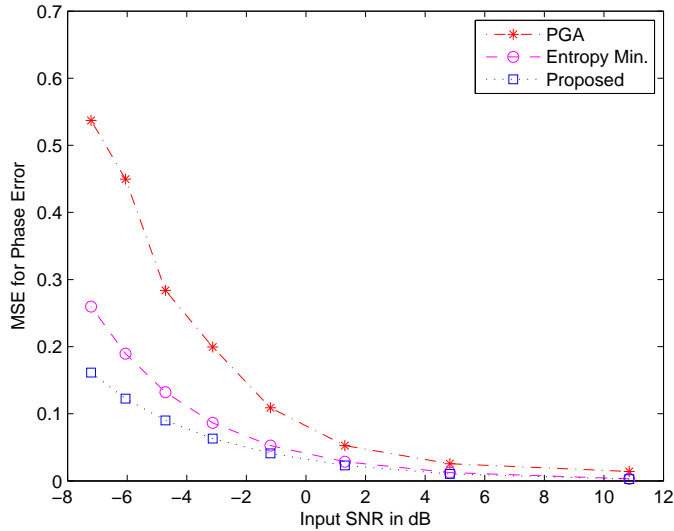
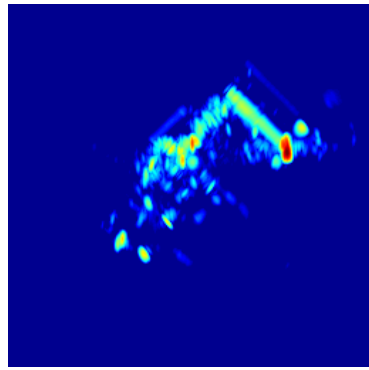


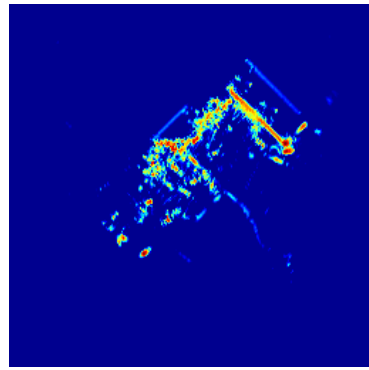
Figure 3.19: MSE evaluation of phase error estimations for the scene in Figure 3.14(a) for various SNRs. Each point on the curves corresponds to an average over 20 experiments with different random 1D phase errors uniformly distributed in $[-\pi, \pi]$.

than PGA and entropy minimization techniques. Furthermore, the proposed method also exhibits superiority over existing autofocus techniques in terms of the quality of the reconstructed scene. In particular, the proposed method results in a finer and more detailed visualization through noise and sidelobe suppression as well as resolution improvements. The reconstructed images and quantitative comparison show the effectiveness of the proposed approach.

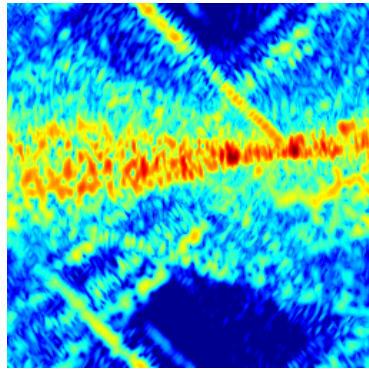
Finally, we compare our method with the recently proposed multichannel autofocus (MCA) technique [14]. We have generated a 64×64 synthetic scene that satisfies the requirements of MCA, involving a condition on the rank of the image, as well as the presence of a low-return region in the scene. The SAR data used in these experiments are corrupted by a 1D cross-range varying random phase error, uniformly distributed in $[-\pi, \pi]$. We show the results of the experiments performed for various input SNR levels in Figure 3.21 and Figure 3.22. We observe that both MCA and SDA perform successful phase error compensation at the relatively high SNR of 27 dB (see Figure 3.21(c) and (d)). However when SNR is reduced to 10 dB, MCA is not able to correct the phase error, as shown in Figure 3.21(f). On



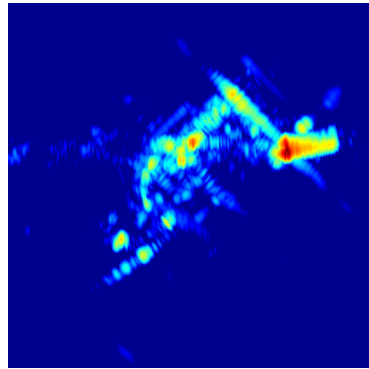
(a)



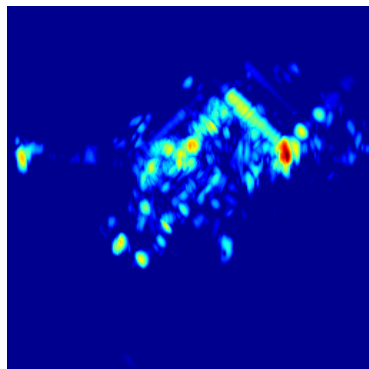
(b)



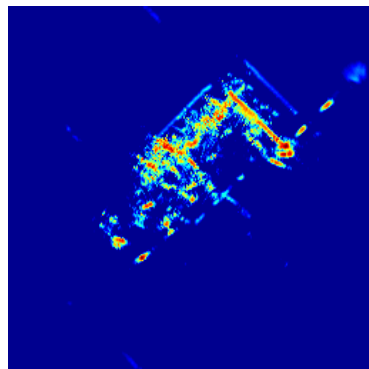
(c)



(d)



(e)



(f)

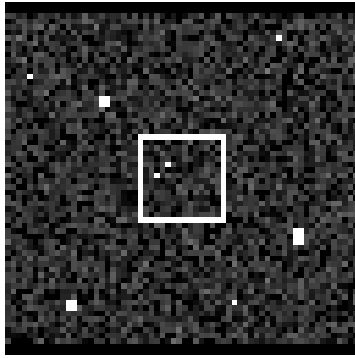
Figure 3.20: Experiments on the Backhoe data for a 1D random phase error with a uniform distribution in $[-\pi, \pi]$. (a) Conventional imaging from data without phase error. (b) Sparsity-driven imaging from data without phase error. (c) Conventional imaging with phase error. (d) Result of PGA. (e) Result of entropy minimization. (f) Result of the proposed SDA method.

the other hand, SDA compensates phase errors, and suppresses noise and clutter effectively even for this relatively low SNR case, as shown in Figure 3.21(g). Figure 3.22 contains a plot of MSEs for phase error estimation achieved by MCA and SDA on this scene for various SNR levels. This plot demonstrates the robustness of SDA to noise. Average computation times required by MCA and the proposed SDA method for the experiments displayed in Figure 3.21 and Figure 3.22 are 0.1629s and 2.5151s, respectively (using non-optimized MATLAB code on an Intel Celeron 2.13GHz CPU). The results of these experiments show that although MCA is a fast algorithm, working very well in scenarios involving high-quality data, its performance degrades significantly as SNR decreases.

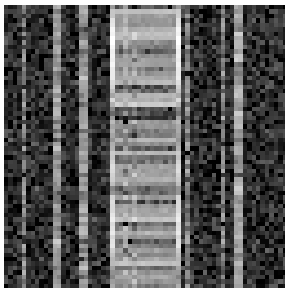
Table 3.2: MSE achieved by various methods in estimating the phase error for the Backhoe experiment in Figure 3.20.

	PGA	Entropy Minimization	Proposed SDA Method
MSE_{PE}	3.3267	2.1715	2.1382

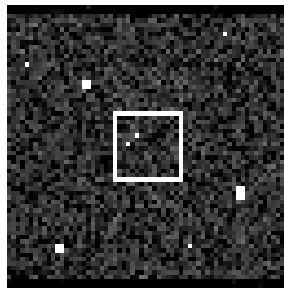
Finally, note that, in all of the experiments on synthetic scenes, the grid we use for imaging is the same with the grid on which point targets lie. For the Backhoe and the Slicy data, we just have access to the phase history data, so the scatterers in this case may not lie on our imaging grid.



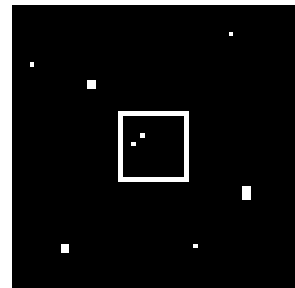
(a)



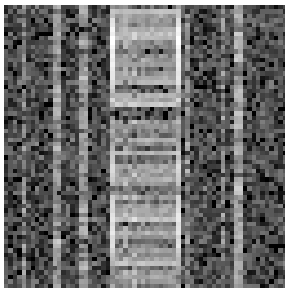
(b)



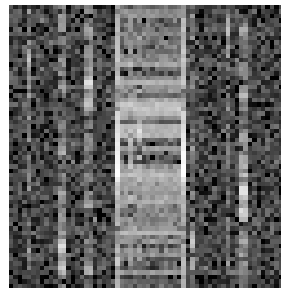
(c)



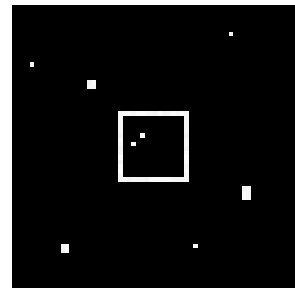
(d)



(e)



(f)



(g)

Figure 3.21: (a) The original scene. (b) Conventional imaging from noisy phase-corrupted data for input SNR of 27dB. (c) Result of MCA for input SNR of 27dB. (d) Result of the proposed SDA method for input SNR of 27dB. (e) Conventional imaging from noisy phase-corrupted data for input SNR of 10dB. (f) Result of MCA for input SNR of 10dB. (g) Result of the proposed SDA method for input SNR of 10dB.

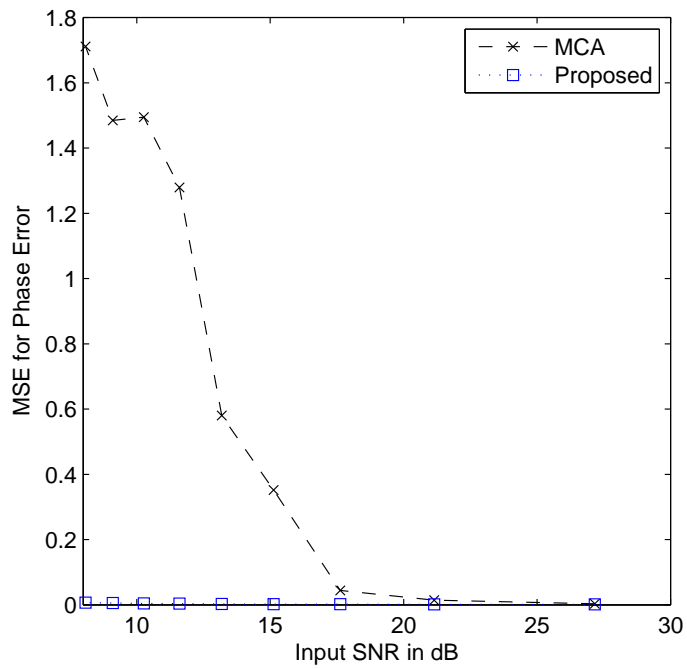


Figure 3.22: MSEs for phase error estimation versus SNR.

Chapter 4

Moving Target Imaging

In synthetic aperture radar (SAR) imaging, uncertainties on the position of the sensing platform or on the motion of the targets in the underlying scene cause phase errors in the SAR data and subsequently defocusing in the reconstructed image. Phase errors arising due to uncertainties in the position of the SAR sensing platform cause space-invariant defocusing, i.e., the amount of the defocusing in the reconstructed image is the same for all points in the scene. This problem is handled in the previous chapter. However, moving targets in the scene induce a space-variant defocus, i.e., defocusing appears only around the positions of the moving targets whereas the stationary background is not defocused [27].

In this chapter, we present an extension of the framework of SDA for the *space-variant* defocusing problem. In this technique, the problem is handled as an optimization problem, in which besides the constraint on the sparsity of the reflectivity field, also a constraint on the spatial sparsity of the phase errors is imposed based on the assumption that motion in the scene is limited to a small number of spatial locations. The method is performed through iterative minimization of a cost function of both the field and the phase errors. Each iteration consists of two steps, the first of which is for image formation and the second is for phase error estimation. For phase error estimation we present two approaches. The first approach looks for potential motion and estimates the phase errors at all points in the scene. The second approach aims to improve the computational efficiency of the phase error estimation procedure by first determining regions of interest for potential motion using a fast procedure, and then performing phase error estimation only in these regions. Ex-

perimental results on various synthetic scenes demonstrate the effectiveness of the proposed method.

4.1 SAR Imaging Model

The phase history data r can be viewed as the sum of the SAR data corresponding to each point in the scene.

$$r = \underbrace{C_{clmn-1}f(1)}_{rp_1} + \underbrace{C_{clmn-2}f(2)}_{rp_2} + \dots + \dots + \underbrace{C_{clmn-I}f(I)}_{rp_I} \quad (4.1)$$

Here, C_{clmn-i} is the i -th column of the model matrix C and, $f(i)$ and rp_i represent the complex reflectivity at the i -th point of the scene and the corresponding SAR data, respectively. I is the total number of points in the scene. The cross-range component of the target velocity causes the image of the target to be defocused in the cross-range direction, whereas the range component causes shifting in the cross-range direction and defocusing in both cross-range and range directions [7, 17]. The image of a target that experiences significant vibration is defocused in the cross-range direction as well [56]. The defocusing arises due to the phase errors in the SAR data of these targets. It is possible to clarify the connection between motion and phase error further. Regarding that SAR data are approximately 2D Fourier transform of the underlying scene, the motion-phase error relationship may be better understood from the Fourier transform perspective. The position of a point in the scene is captured in the phase of the corresponding frequency domain data. We know it also from the Fourier transform property which relates a shift in the image domain with a proportional phase addition in the frequency domain. Therefore, if a target moves from point a to point b, in the time between two data collection points, the data collected when the target is in point b would be the same as the data if the target was at point a but the data are phase corrupted.

Now, let us view the i -th point in the scene as a point target having a motion which results in defocusing along the cross-range direction. The SAR data of this

target can be expressed as [7, 17]:

$$\begin{bmatrix} rp_{i_{1e}} \\ rp_{i_{2e}} \\ \cdot \\ \cdot \\ \cdot \\ rp_{i_{Me}} \end{bmatrix} = \begin{bmatrix} e^{j\phi_i(1)} rp_{i_1} \\ e^{j\phi_i(2)} rp_{i_2} \\ \cdot \\ \cdot \\ \cdot \\ e^{j\phi_i(M)} rp_{i_M} \end{bmatrix} \quad (4.2)$$

Here, ϕ_i represents the phase error caused by the motion of the target and, rp_i and rp_{i_e} are the phase history data for the stationary and moving point target, respectively. In a similar way, this relation can be expressed in terms of the model matrix C as follows:

$$\begin{bmatrix} C_{clmn-i_1}(\phi) \\ C_{clmn-i_2}(\phi) \\ \cdot \\ \cdot \\ \cdot \\ C_{clmn-i_M}(\phi) \end{bmatrix} = \begin{bmatrix} e^{j\phi_i(1)} C_{clmn-i_1} \\ e^{j\phi_i(2)} C_{clmn-i_2} \\ \cdot \\ \cdot \\ \cdot \\ e^{j\phi_i(M)} C_{clmn-i_M} \end{bmatrix} \quad (4.3)$$

Here, $C_{clmn-i}(\phi)$ is the i -th column of the model matrix $C(\phi)$ that takes the movement of the targets into account and $C_{clmn-i_m}(\phi)$ is the part of $C_{clmn-i}(\phi)$ for the m -th cross-range position. In the presence of additional observation noise, the observation model for the overall system becomes

$$g = C(\phi)f + v \quad (4.4)$$

where, v is the observation noise. In this way, we have turned the moving target imaging problem into the problem of imaging a stationary scene with phase corrupted data. Here, the aim is to estimate f and ϕ from the noisy observation g .

4.2 Proposed Method

We propose a sparsity-driven method for joint estimation of the field and phase errors caused by the targets moving in cross-range direction [57]. A constant velocity in the

range direction results in a cross-range shift in the image domain without defocusing and like other autofocus techniques, our approach is also insensitive to such type of errors. Therefore, currently, our approach is limited to motions in cross-range direction. The method is based on a nonquadratic regularization-based framework which allows the incorporation of the prior sparsity information about the field and about the phase errors into the problem. The phase errors are incorporated into the problem using the vector β , which includes phase errors corresponding to all points in the scene, for all aperture positions.

$$\beta = \begin{bmatrix} \beta_1 \\ \beta_2 \\ \cdot \\ \cdot \\ \beta_M \end{bmatrix} \quad (4.5)$$

Here, β_m is the vector of phase errors for the m -th aperture position and has the following form:

$$\beta_m = [e^{j\phi_1(m)}, e^{j\phi_2(m)}, \dots, e^{j\phi_I(m)}]^T \quad (4.6)$$

The method is performed by minimizing the following cost function with respect to the field and phase errors.

$$\begin{aligned} \arg \min_{f, \beta} J(f, \beta) &= \arg \min_{f, \beta} \|g - C(\phi)f\|_2^2 + \lambda_1 \|f\|_1 + \lambda_2 \|\beta - \mathbf{1}\|_1 \\ &s.t. \quad |\beta(i)| = 1 \quad \forall i \end{aligned} \quad (4.7)$$

Here, $\mathbf{1}$ is a $MI \times 1$ vector of ones. Since the number of moving points is much less than the total number of points in the scene, most of the ϕ values in the vector β are zero. Since the elements of β are in the form of $e^{j\phi}$'s, when ϕ is zero, β becomes one. Therefore, this sparsity on the phase errors is incorporated into the problem by using the regularization term $\|\beta - \mathbf{1}\|_1$.

This problem is solved similarly to the optimization problem in the previous chapter and in a previous work on SAR imaging [58]. The algorithm is iterative and at each iteration, in first step, the cost function $J(f, \beta)$ is minimized with respect

to the field f .

$$\hat{f}^{(n+1)} = \arg \min_f J(f, \hat{\beta}^{(n)}) = \arg \min_f \|g - C(\phi^n)f\|_2^2 + \lambda_1 \|f\|_1 \quad (4.8)$$

This minimization problem is solved identically to the one in the previous chapter. In the second step of each iteration, we use the field estimate \hat{f} from the first step and estimate the phase errors by minimizing the following cost function for each aperture position:

$$\begin{aligned} \hat{\beta}_m^{(n+1)} = \arg \min_{\beta_m} J(\hat{f}^{(n+1)}, \beta_m) = \arg \min_{\beta_m} \|g_m - C_m T^{(n+1)} \beta_m\|_2^2 + \lambda_2 \|\beta_m - \mathbf{1}\|_1 \\ \text{s.t.} \quad |\beta_m(i)| = 1 \quad \forall i \end{aligned} \quad (4.9)$$

Here, T is a diagonal matrix, with the entries $\hat{f}(i)$ on its main diagonal, as follows:

$$T^{(n+1)} = \text{diag} \left\{ \hat{f}^{(n+1)}(i) \right\} \quad (4.10)$$

In (4.9), $\mathbf{1}$ is a $I \times 1$ vector of ones. The constrained optimization problem in (4.9) is replaced with the following unconstrained problem that incorporates a penalty term on the magnitudes of $\beta_m(i)$'s.

$$\begin{aligned} \hat{\beta}_m^{(n+1)} = \arg \min_{\beta_m} \|g_m - C_m T^{(n+1)} \beta_m\|_2^2 + \lambda_2 \|\beta_m - \mathbf{1}\|_1 + \lambda_3 \sum_{i=1}^I (|\beta_m(i)| - 1)^2 \\ = \arg \min_{\beta_m} \|g_m - C_m T^{(n+1)} \beta_m\|_2^2 + \lambda_2 \|\beta_m - \mathbf{1}\|_1 + \lambda_3 \|\beta_m\|_2^2 - 2\lambda_3 \|\beta_m\|_1 \\ m = 1, 2, \dots, M \end{aligned} \quad (4.11)$$

This optimization problem is solved by using the same technique as in the field estimation step. In each iteration, $\hat{\beta}_m$ is obtained as

$$\begin{aligned} \hat{\beta}_m^{(\bar{n}+1)} = \left[2 \left(C_m T^{(n+1)} \right)^H \left(C_m T^{(n+1)} \right) + \lambda_2 W_1(\hat{\beta}_m^{(\bar{n})}) + 2\lambda_3 W_2(\hat{\beta}_m^{(\bar{n})}) - 2\lambda_3 W_3(\hat{\beta}_m^{(\bar{n})}) \right]^{-1} \\ \left[2 \left(C_m T^{(n+1)} \right)^H g_m + \lambda_2 W_1(\hat{\beta}_m^{(\bar{n})}) \mathbf{1} \right] \end{aligned} \quad (4.12)$$

where $W_1(\hat{\beta}_m^{(n)})$, $W_2(\hat{\beta}_m^{(n)})$ and $W_3(\hat{\beta}_m^{(n)})$ are diagonal matrices as follows:

$$W_1(\hat{\beta}_m^{(\bar{n})}) = \text{diag} \left[\frac{1}{\left(\left| \hat{\beta}_m^{(\bar{n})}(i) - 1 \right|^2 + \sigma \right)^{1/2}} \dots \frac{1}{\left(\left| \hat{\beta}_m^{(\bar{n})}(I) - 1 \right|^2 + \sigma \right)^{1/2}} \right] \quad (4.13)$$

$$W_2(\hat{\beta}_m^{(\bar{n})}) = \Lambda \quad (4.14)$$

$$W_3(\hat{\beta}_m^{(\bar{n})}) = \text{diag} \left[\frac{1}{\left(\left| \hat{\beta}_m^{(\bar{n})}(i) \right|^2 + \sigma \right)^{1/2}} \cdots \frac{1}{\left(\left| \hat{\beta}_m^{(\bar{n})}(I) \right|^2 + \sigma \right)^{1/2}} \right] \quad (4.15)$$

Here, \bar{n} denotes the iteration number in the internal optimization problem and Λ in (4.14) is the identity matrix. Using the estimate $\hat{\beta}_m$, the following matrix is created,

$$B_m^{(n+1)} = \text{diag} \left\{ \hat{\beta}_m^{(n+1)}(i) \right\} \quad (4.16)$$

which is used to update the model matrix for the m – th aperture position.

$$C_m(\phi^{n+1}) = C_m B_m^{(n+1)} \quad (4.17)$$

After these phase estimation and model matrix update procedures have been completed for all aperture positions, the algorithm passes to the next iteration, by incrementing n and returning to (4.8).

4.2.1 Phase Error Estimation and Correction by Determining Regions of Interest (ROI)

The approach we have described in the previous section looks for potential motion everywhere in the scene. However, moving points usually exist in limited regions of a scene. Let us consider a scene containing a few moving vehicles. In this case, only a small portion of the entire scene will contain motion, and all the points belonging to a vehicle will have the same motion. In order to exploit such a structure both for computational gains and for improved robustness, we present a modified phase error estimation procedure. In the phase error estimation step of every iteration to solve the optimization problem in (4.7), we now propose a two-level approach [59]. In the first level, we determine the range lines that are likely to contain moving objects. This generates regions of interest which we use in the second level to estimate the phase error. Assuming that the targets in each of these regions have the same motion and clutter is not strong, we perform space-invariant phase error estimation and compensation for each region. Now let us describe the overall phase

error estimation step in detail. In the first level of the phase error estimation step the following cost function is minimized with respect to phase errors.

$$\begin{aligned}\hat{\beta}_m &= \arg \min_{\beta_m} J(\hat{f}^{(n+1)}, \beta_m) \\ &= \arg \min_{\beta_m} \|g_m - C_m T^{(n+1)} \beta_m\|_2^2 + \lambda_2 \|\beta_m - \mathbf{1}\|_1\end{aligned}\quad (4.18)$$

Note that this optimization problem is slightly different from the one in (4.9) in the sense that the constraint on the magnitudes of the vector β is missing. This slight modification leads to significant computational savings. Since the goal of this first level is just to determine the ROI, rather than estimating β perfectly, the inaccuracies caused by this modification do not have a significant impact on overall performance. Using the estimated the β_m vectors, a matrix P is created, columns of which are the phase values of the β_m vectors, i.e., the ϕ values.

$$P = \begin{bmatrix} \angle \hat{\beta}_1 & \angle \hat{\beta}_2 & \dots & \angle \hat{\beta}_M \end{bmatrix} \quad (4.19)$$

i -th row of the matrix P corresponds to the phase error vector for the i -th point in the scene. After taking the absolute value of each element of the matrix P , an $I \times 1$ vector P_{sum} is created by summing the elements in each row.

$$P_{sum}(i) = \sum_{m=1}^M abs(P(i, m)) \quad \forall i \quad (4.20)$$

Let the total number of image domain range indices be A and the total number of image domain cross-range indices be B . By reshaping the vector P_{sum} to an $A \times B$ matrix and then summing the elements in each column of this matrix, a $1 \times B$ vector V is obtained which includes a phase error-related value for each range line in the scene. For the range lines in which moving targets exist, this value is relatively greater than the values for other range lines. The vector V is normalized and the range lines having a value greater than a pre-determined threshold ς are decided to be range lines that potentially contain moving targets. This completes the first level of the phase error estimation step.

The second level involves estimation of the phase error in each region determined in the first level. We assume that there is a single target on a weak background in each distinct ROI and adjacent range lines correspond to the same target. Regarding

this assumption we apply space-invariant focusing for each spatially distinct region.¹ This reduces the number of unknown phase error terms as compared to our more generic approach, and leads to improved robustness in cases where the assumption that there is a single motion in each spatially connected ROI is valid. To simply explain the second level of the phase error estimation procedure, let us assume that there is only one moving target in the scene. Let the parts of the model matrix and the field corresponding to the region of interest be C_{reg} and f_{reg} , and the parts of model matrix and the field corresponding to the outside of this region be C_{out} and f_{out} , respectively. Then the phase error ϕ_{reg} is estimated by minimizing the following cost function for every aperture position

$$\hat{\phi}_{reg}^{(n+1)}(m) = \arg \min_{\phi_{reg}(m)} \left\| g_{regm}^{(n+1)} - e^{j\phi_{reg}(m)} C_{regm} \hat{f}_{reg}^{(n+1)} \right\|_2^2 \quad (4.21)$$

for $m = 1, 2, \dots, M$

where g_{reg} is the phase history data corresponding to the region of interest and is given by:

$$g_{reg}^{(n+1)} = g - C_{out} f_{out}^{(n+1)} \quad (4.22)$$

The problem in (4.22) is solved in closed form for every aperture position [50, 52]. Using the phase error estimate, the corresponding part of the model matrix is updated.

$$C_{regm}(\hat{\phi}_{reg}^{(n+1)}(m)) = e^{j\hat{\phi}_{reg}^{(n+1)}(m)} C_{regm} \quad \text{for } m = 1, \dots, M \quad (4.23)$$

If there are more than one moving targets in the scene, then this procedure is implemented for all regions with a potentially moving target. After the model matrix has been updated, the algorithm passes to the next iteration, by incrementing n and returning to the field estimation step.

Note that, the algorithms developed for moving target indication (MTI) share the same idea with our approach. In MTI processing, the change in successive pulses are used since the components of the received signal belonging to a stationary target

¹We could apply space variant focusing in each ROI. This would require less computation than our general approach, described at the beginning of Section 4.2, but more than the space-invariant approach described here.

or the stationary background have the same amplitude and phase for each pulse, where the phase of a moving target component varies due to the changing range. If the change between successive pulses is greater than a threshold, a moving target is declared. However, in MTI processing the only information obtained is the presence or the absence of a moving target in the scene. Moreover, it does not provide information about the number of targets [60].

4.3 Experimental Results

We present experimental results on various synthetic scenes. To demonstrate the effectiveness of and highlight the benefits specifically provided by the proposed method, for all experiments, the images reconstructed by conventional imaging (the polar format algorithm [27]) and sparsity-driven imaging [20] are presented as well. Moreover, to show that the algorithms developed for the space-invariant focusing cannot deal with the space-variant defocusing, for the first two experiments the results obtained by the SDA method proposed in Chapter 3 for space-invariant focusing and the well-known PGA method are presented as well. Synthetic scenes used in the first two experiments include many point targets with different type of phase errors. To simulate different motions and velocities of the targets, the phase history data of each target are corrupted by a different phase error function. In the first experiment, results of which are displayed in Figure 4.1, the phase histories of the three point targets are corrupted by independent random phase error functions uniformly distributed in $[-\pi/2, \pi/2]$. The phase histories of the two bigger targets are corrupted by quadratic phase error functions of different peak values. In the second experiment, results of which are displayed in Figure 4.2, the scene is constructed so that it involves many stationary point targets and a strongly vibrating rigid-body target. To simulate it, the phase history data corresponding to each point of this target are corrupted by independent random phase error functions uniformly distributed in $[-\pi/2, \pi/2]$. From the results of these two experiments, for conventional imaging and sparsity-driven imaging without any phase error correction, the defocusing and artifacts in the reconstructed images caused by the moving targets are clearly seen. Besides, we see that space-invariant focusing algorithms cannot

correct space-variant defocusing. However, with the proposed approach, phase errors are effectively removed and focused images are obtained. The scene for the third experiment is shown in Figure 4.3(a). There are four targets in the scene one of which (the leftmost one) is stationary and the other three have different motions. To simulate different motions and velocities of the targets, the phase history data of each target are corrupted by a different phase error function. The phase histories of the two targets lying in the right side of the scene are corrupted by independent random phase error functions uniformly distributed in $[-\pi/2, \pi/2]$ to simulate a vibration effect. The phase history data of the remaining target, third one from right in the scene, are corrupted by a quadratic phase error function to simulate a constant motion in cross-range direction. In Figure 4.3, the results of this experiment are displayed. In the results for conventional imaging and sparsity-driven imaging without any phase error correction, the defocusing and artifacts in the reconstructed images caused by the moving targets are clearly seen. On the other hand, images reconstructed by the proposed method are well focused and exhibit the advantages of sparsity-driven imaging such as high resolution, reduced speckle and sidelobes. For the next experiments, we establish the physical relationship between the phase error and the velocity of a target having a constant motion in cross-range direction. In this part we provide results also for the ROI-based approach. The threshold ς used in ROI-based approach is chosen as 0.3. In the next experiment, the scene involves many stationary point targets and two moving targets with constant velocities of $5m/s$ and $8m/s$ in the cross-range direction. The SAR system parameters for this experiment are shown in Table 4.1. For the two moving targets, the cross-range velocity induced quadratic phase error is computed as follows [7]:

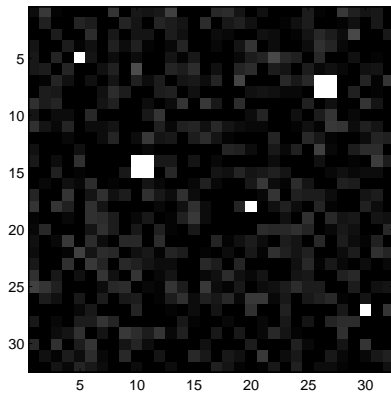
$$\phi(t_s) = \frac{4\pi v_{cr} v_p t_s^2}{\lambda_w d_0} \quad (4.24)$$

Here, t_s is the slow-time variable (continuous variable along the cross-range) and v_{cr} is the constant cross-range velocity of the target. According to this relationship, the target with velocity $5m/s$ and the target with velocity $8m/s$ will induce a quadratic phase error defined over an aperture $-T/2 \leq t_s \leq T/2$ with a center to edge amplitude of 2.5π radians and 4π radians, respectively. In Figure 4.4, the results for this experiment are displayed. In this experiment, we present the results of our general approach as well as our ROI-based approach. As shown in Figure 4.4, the

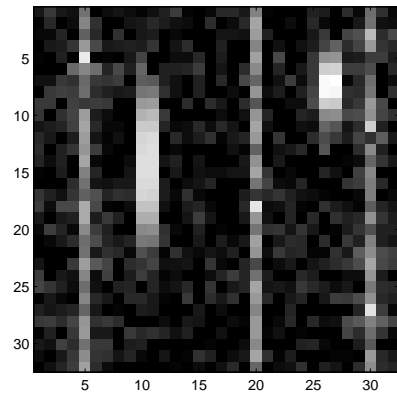
Table 4.1: SAR System Parameters for Experiments in Figure 4.4 and Figure 4.5

range resolution ρ_r	$1m$
cross-range resolution ρ_{cr}	$1m$
wavelength λ_w	$0.02m$
angular range ($\Delta\theta$)	0.573°
center frequency f_0	$15GHz.$
distance between the SAR platform and patch center d_0	$30000m$
platform velocity v_p	$300m/s$
aperture time $T = \frac{\lambda_w d_0}{2v_p \rho_{cr}}$	$1s$

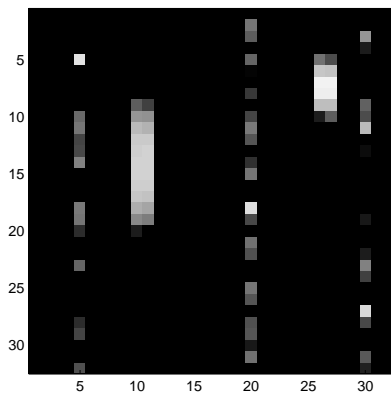
two approaches produce successful and visually indistinguishable results. In the last experiment, performed on another synthetic scene involving many point-like targets and a larger rigid-body target, we again use SAR system parameters displayed in Table 4.1. The phase history data of the rigid-body target are corrupted with a quadratic phase error of a center to edge amplitude of 4π radians which corresponds to a cross-range velocity of $8m/s$. In this experiment, we employ our ROI-based approach. The results presented in Figure 4.5 show the effectiveness of the approach in estimating and compensating phase errors.



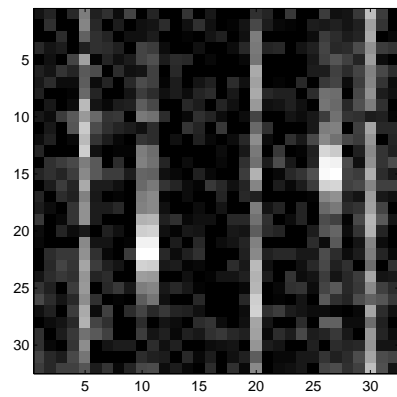
(a)



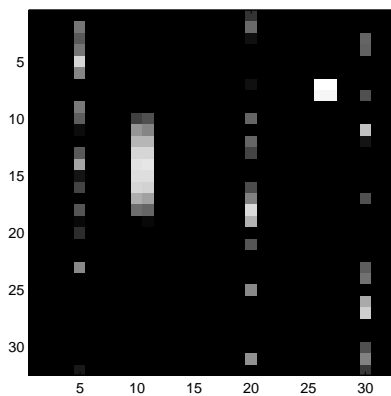
(b)



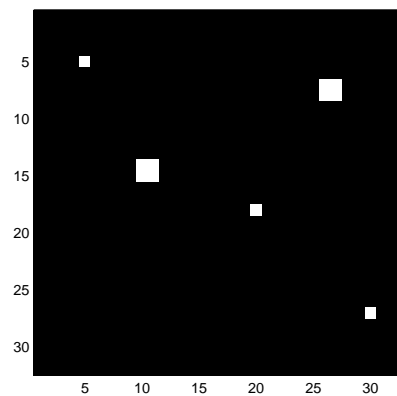
(c)



(d)

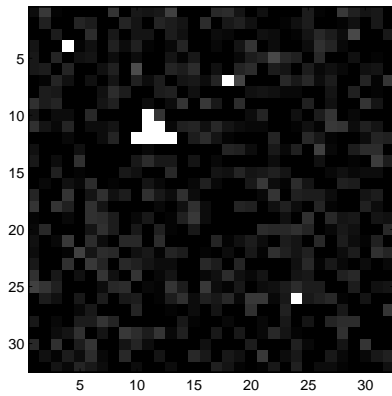


(e)

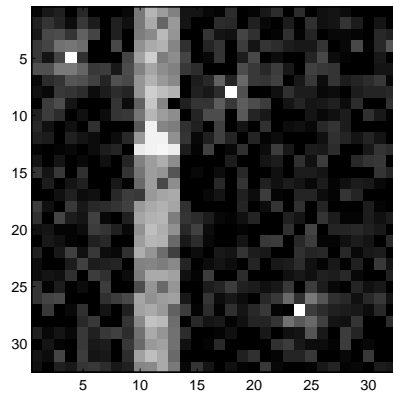


(f)

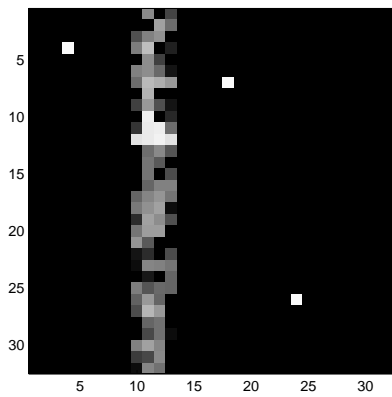
Figure 4.1: Results of the first experiment. a) Original scene. b) Image reconstructed by conventional imaging. c) Image reconstructed by sparsity-driven imaging. d) Image obtained by using the PGA method for space-invariant focusing. e) Image reconstructed by the SDA method for space-invariant focusing. f) Image reconstructed by the proposed method for space-variant focusing.



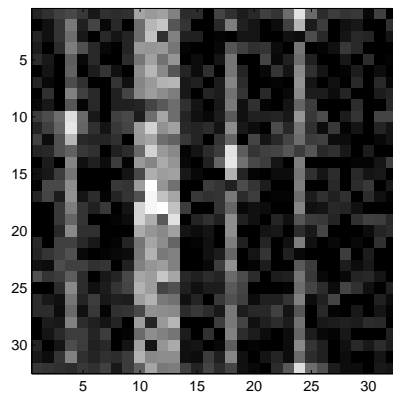
(a)



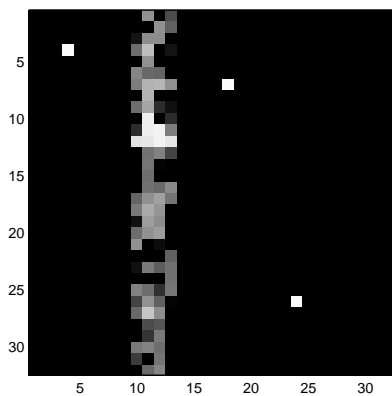
(b)



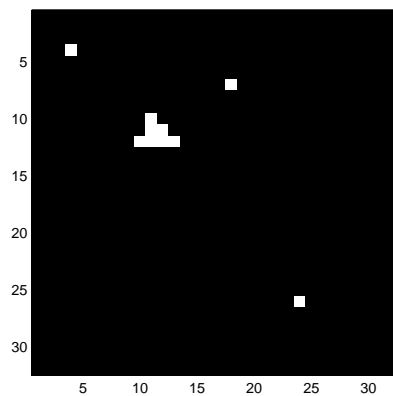
(c)



(d)

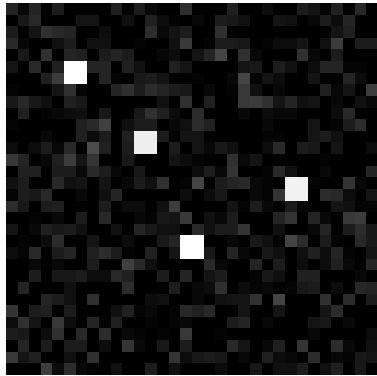


(e)

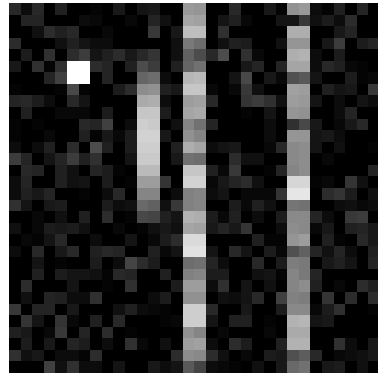


(f)

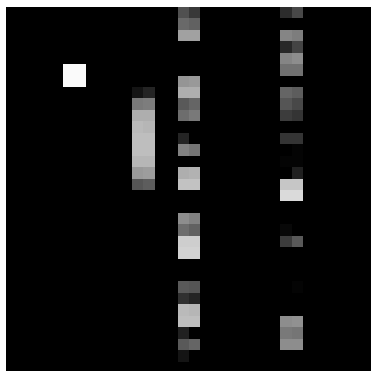
Figure 4.2: Results of the second experiment. a) Original scene. b) Image reconstructed by conventional imaging. c) Image reconstructed by sparsity-driven imaging. d) Image obtained by using the PGA method for space-invariant focusing. e) Image reconstructed by the SDA method for space-invariant focusing. f) Image reconstructed by the proposed method for space-variant focusing.



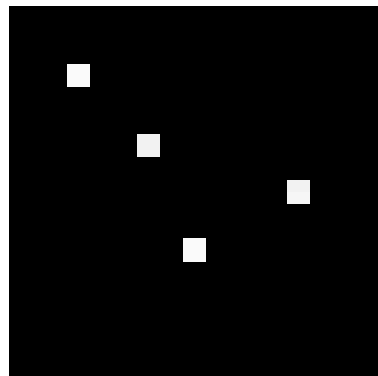
(a)



(b)

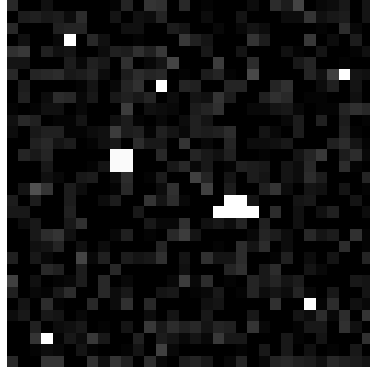


(c)

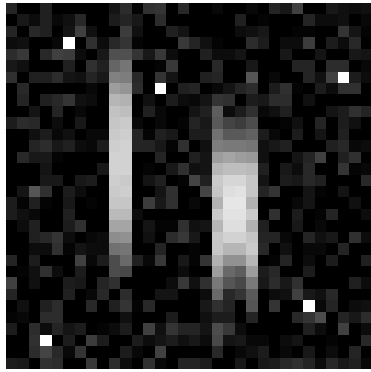


(d)

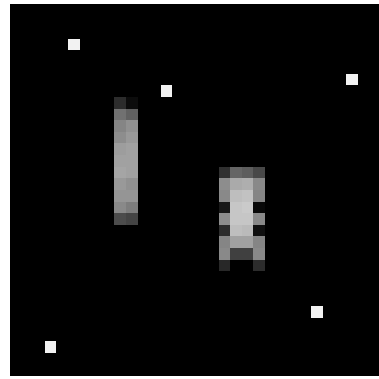
Figure 4.3: Results of the third experiment. a) Original scene. b) Image reconstructed by conventional imaging. c) Image reconstructed by sparsity-driven imaging. d) Image reconstructed by the proposed method.



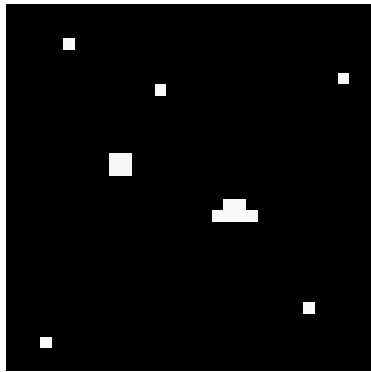
(a)



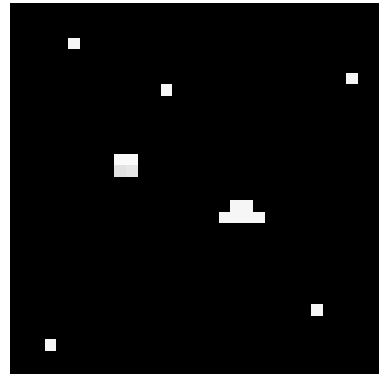
(b)



(c)

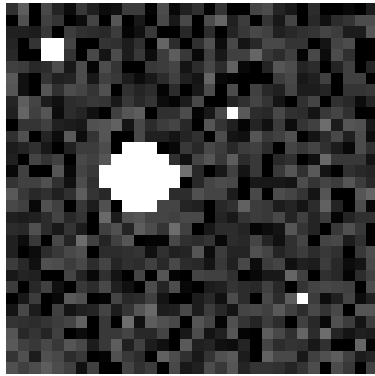


(d)

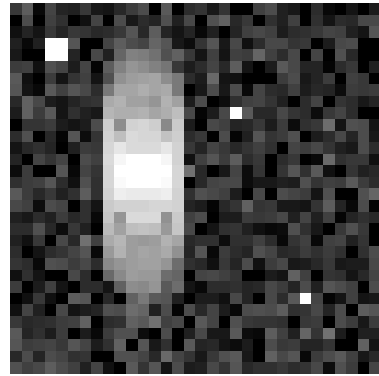


(e)

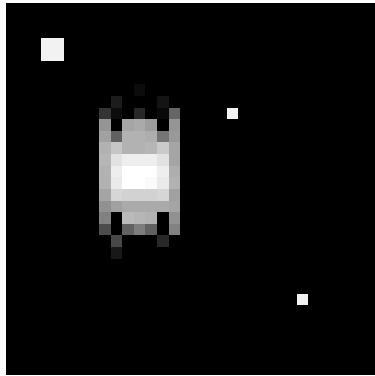
Figure 4.4: Results of the fourth experiment. a) Original scene. b) Image reconstructed by conventional imaging. c) Image reconstructed by sparsity-driven imaging. d) Image reconstructed by the proposed method. e) Image reconstructed by the proposed method with phase error estimation for ROI.



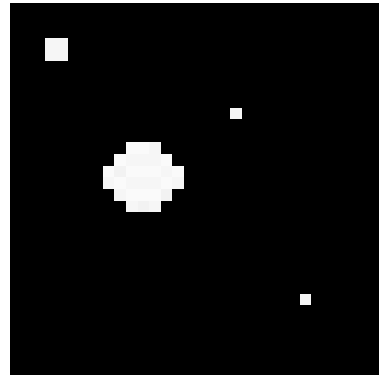
(a)



(b)



(c)



(d)

Figure 4.5: Results of the fifth experiment. a) Original scene. b) Image reconstructed by conventional imaging. c) Image reconstructed by sparsity-driven imaging. d) Image reconstructed by the proposed method with phase error estimation for ROI.

Chapter 5

Conclusion and Potential Future Research

5.1 Conclusion

We have proposed and demonstrated a sparsity-driven technique for joint SAR imaging and phase error correction. The method corrects the phase errors during the image formation process while it produces high resolution focused SAR images, thanks to its sparsity enforcing nature resulting from the use of a nonquadratic regularization-based framework. Since image formation and phase error estimation are performed simultaneously, the overall computational load of the proposed method is not significantly more than that of sparsity-driven imaging without phase error compensation. The method can handle 1D as well as 2D phase errors. Experimental results on various scenarios demonstrate the effectiveness of the proposed approach as well as the improvements it provides over existing methods for phase error correction.

We have presented an extension of this framework for the *space-variant* defocusing problem as well. In this technique, the problem is handled as an optimization problem, in which besides the constraint on the sparsity of the reflectivity field, also a constraint on the spatial sparsity of the phase errors is imposed based on the assumption that motion in the scene is limited to a small number of spatial locations. The algorithm involves iterative minimization of a cost function of both the field and the phase errors. Each iteration consists of two steps, the first of which is

for image formation and the second is for phase error estimation. For phase error estimation we have presented two approaches. The first approach looks for potential motion and estimates the phase errors at all points in the scene. The second approach aims to improve the robustness of the phase error estimation procedure by first determining regions of interest for potential motion using a fast procedure, and then performing phase error estimation only in these regions. Experimental results on various synthetic scenes have demonstrated the effectiveness of the proposed method.

5.2 Potential Future Research

There are many potential future research directions.

5.2.1 Application of the Proposed Method to Other Areas

First, in this work we considered SAR, but our model-error formulation makes our approach applicable in other areas, where similar types of model errors are encountered, as well. Especially in medical imaging (e.g. Magnetic Resonance Imaging (MRI), Computerized Tomography (CT)), similar motion-induced errors appear due to the patient movements during the imaging. The sparsity can be imposed to the problem using appropriate dictionaries.

5.2.2 Using the Proposed Framework with Other Dictionaries

Other potential extensions may be the formulation of the problem for scenarios involving sparse representations of the field in various spatial dictionaries (e.g., wavelets, shearlets, learned dictionaries) or in other domains with appropriate regularization terms (e.g. for a smooth field, the derivative of the field may be considered as sparse). Another option is the incorporation of prior information or some constraints on phase error. Moreover, the dictionary approach can be used also for phase error estimation step by creating a dictionary using potential phase values to be captured in every iteration.

5.2.3 Adaptive Approaches in Regularization-based Imaging

Some improvement can be obtained in the performance of the SDA technique by using an adaptive approach in the regularization-based imaging process. An example may be to select the regularization parameter adaptively, i.e., the regularization parameter will be not fixed, in every iteration a new regularization parameter will be determined according to the convergence of the algorithm. Another example of using an adaptive approach may be to use the weighted l_1 -norm procedure [61]. The algorithm consists of solving a sequence of weighted l_1 -minimization problems where the weights used for the next iteration are computed from the value of the current solution [61]. It has been shown that in many situations this ‘weighted’ approach outperforms l_1 -minimization in the sense that substantially fewer measurements are needed for exact recovery [61].

5.2.4 Velocity Estimation using the Corresponding Phase Error Estimate

The mathematical relationship between the velocity of a moving target and the corresponding phase error has been examined and derived before for various motion types [7, 17, 56]. However, although the mathematical formulation of this relationship is known, to obtain the velocity information from the corresponding phase error estimate is not an easy task due to: 1) As explained before in Section 3.2.2, a constant (as a function of the aperture position) phase shift has no effect on the reconstructed image and a linear phase shift does not cause blurring, but rather a spatial shift in the reconstructed image. Since our method (like all other autofocus techniques) is insensitive to such type of phase errors, the constant and the linear components, the phase error estimate may involve should be first removed to obtain a reliable velocity estimation. 2) The estimated phase error function is the wrapped version of the original phase error function into the interval $[-\pi, \pi]$. To obtain the velocity information, an unwrapping operation, which is a nontrivial task, is needed. Therefore, a potential future research topic is the development of a procedure to deal with the problems mentioned above. If the magnitude of the

velocity can be estimated perfectly then to determine the direction of the velocity may be possible as well.

5.2.5 Imaging of Moving Targets with Reflectivities Changing in Time

In the proposed technique, it is assumed that the reflectivities of the moving targets do not change during the data collection time. However, in practice, particularly for wide angle imaging, the reflectivities of the targets may change during the data collection time. The proposed technique can be extended so that it considers this fact. Actually, the same problem appears in wide angle imaging of stationary fields as well. In the experiments on Backhoe data, we have overcome this problem by combining sub-aperture images via composite imaging, where we have assumed that the reflectivities inside the time intervals for the sub-apertures do not change but they can change across sub-apertures. The same composite imaging approach can be applied to moving target imaging as well. A more challenging alternative would be to consider data from the entire aperture simultaneously while the reflectivities of the targets may be changing. Such an idea has been used in wide-angle imaging of stationary scenes before [62], and could be considered for the moving target imaging problem as well.

5.2.6 Multi-static SAR Applications

In this dissertation, we considered mono-static SAR. In mono-static SAR, the SAR sensor system involves one transmitter and one receiver on the same platform. However, currently, multi-static SAR systems are great of interest. These SAR systems may include many transmitters and receivers, also on separate platforms and this helps to collect additional information about the scene. Since such SAR systems have many transmitters and receivers, the potential to encounter motion-induced errors increases. Therefore, the model errors arising in multistatic SAR scenarios are a potential research topic for us.

5.2.7 Group Sparsity Approach for Moving Target Imaging

In moving target imaging, this version of our approach does not put any constraints in the phase error vector we get at each aperture position. However, we expect to get nonzero phase error at the same spatial locations at all aperture positions. This might motivate a "group sparsity" approach on the phase error vector based on all data.

Appendix A

Appendix

In this appendix, we describe how we get from Eqn. (3.7) to Eqn. (3.8). The cost function in (3.7) for phase error estimation is as follows:

$$\hat{\phi}_{1D}^{(n+1)}(m) = \arg \min_{\phi_{1D}(m)} J(\hat{f}^{(n+1)}, \phi_{1D}(m)) = \arg \min_{\phi_{1D}(m)} \left\| \bar{g}_m - e^{(j\phi_{1D}(m))} \bar{C}_m \hat{f}^{(n+1)} \right\|_2^2$$

for $m = 1, 2, \dots, M$

Here, M denotes the total number of cross-range positions. When we evaluate the norm expression we get

$$\begin{aligned} \left\| \bar{g}_m - e^{(j\phi_{1D}(m))} \bar{C}_m \hat{f}^{(n+1)} \right\|_2^2 &= (\bar{g}_m - e^{(j\phi_{1D}(m))} \bar{C}_m \hat{f}^{(n+1)})^H (\bar{g}_m - e^{(j\phi_{1D}(m))} \bar{C}_m \hat{f}^{(n+1)}) \\ &= \bar{g}_m^H \bar{g}_m - \bar{g}_m^H e^{(j\phi_{1D}(m))} \bar{C}_m \hat{f}^{(n+1)} - \hat{f}^{(n+1)H} \bar{C}_m^H (e^{(j\phi_{1D}(m))})^H \bar{g}_m + \\ &\quad \hat{f}^{(n+1)H} \bar{C}_m^H \underbrace{(e^{(j\phi_{1D}(m))})^H}_{e^{(-j\phi_{1D}(m))}} \bar{C}_m \hat{f}^{(n+1)} \\ &= \bar{g}_m^H \bar{g}_m - \bar{g}_m^H [\cos(\phi_{1D}(m)) + j \sin(\phi_{1D}(m))] \bar{C}_m \hat{f}^{(n+1)} - \\ &\quad \hat{f}^{(n+1)H} \bar{C}_m^H [\cos(\phi_{1D}(m)) - j \sin(\phi_{1D}(m))] \bar{g}_m + \hat{f}^{(n+1)H} \bar{C}_m^H \bar{C}_m \hat{f}^{(n+1)} \\ &= \bar{g}_m^H \bar{g}_m - 2Re\{\cos(\phi_{1D}(m)) \hat{f}^{(n+1)H} \bar{C}_m^H \bar{g}_m\} + 2Re\{j \sin(\phi_{1D}(m)) \hat{f}^{(n+1)H} \bar{C}_m^H \bar{g}_m\} + \\ &\quad \hat{f}^{(n+1)H} \bar{C}_m^H \bar{C}_m \hat{f}^{(n+1)} \\ &= \bar{g}_m^H \bar{g}_m - 2 \cos(\phi_{1D}(m)) Re\{\hat{f}^{(n+1)H} \bar{C}_m^H \bar{g}_m\} - \\ &\quad 2 \sin(\phi_{1D}(m)) Im\{\hat{f}^{(n+1)H} \bar{C}_m^H \bar{g}_m\} + \hat{f}^{(n+1)H} \bar{C}_m^H \bar{C}_m \hat{f}^{(n+1)} \end{aligned}$$

Let $Re\{\hat{f}^{(n+1)H} \bar{C}_m^H \bar{g}_m\} = \Re$ and $Im\{\hat{f}^{(n+1)H} \bar{C}_m^H \bar{g}_m\} = \Im$

Since we can write $\sin(\phi_{1D}(m))$ as $\cos(\phi_{1D}(m) - \frac{\pi}{2})$ the equation becomes

$$\left\| \bar{g}_m - e^{j\phi_{1D}(m)} \bar{C}_m \hat{f}^{(n+1)} \right\|_2^2 = \bar{g}_m^H \bar{g}_m - 2[\Re \cos(\phi_{1D}(m)) + \Im \cos(\phi_{1D}(m) - \frac{\pi}{2})] + \hat{f}^{(n+1)H} \bar{C}_m^H \bar{C}_m \hat{f}^{(n+1)}$$

The cosines in the previous equation can be added with phasor addition rule to a single cosine. The phasors for the terms $\Re \cos(\phi_{1D}(m))$ and $\Im \cos(\phi_{1D}(m) - \frac{\pi}{2})$ can be seen below.

$$P_1 = Re^{j0} = \Re \quad P_2 = \Im e^{-j\frac{\pi}{2}} = -j\Im$$

If we add the phasors

$$P_1 + P_2 = \Re + (-j\Im) = \Re - j\Im$$

we can find the magnitude and the phase of the new cosine as

$$magnitude = \sqrt{\Re^2 + \Im^2} \quad phase = \arctan\left(\frac{-\Im}{\Re}\right)$$

Finally, we can write

$$\left\| \bar{g}_m - e^{j\phi_{1D}(m)} \bar{C}_m \hat{f}^{(n+1)} \right\|_2^2 = \bar{g}_m^H \bar{g}_m - 2\sqrt{\Re^2 + \Im^2} \cos[\phi_{1D}(m) + \arctan\left(\frac{-\Im}{\Re}\right)] + \hat{f}^{(n+1)H} \bar{C}_m^H \bar{C}_m \hat{f}^{(n+1)}$$

Bibliography

- [1] C. R. Jackson and ed. J. R. Apel, *Synthetic Aperture Radar Marine User's Manual*, U.S. Department of Commerce, sponsored by NOAA/NESDIS, <http://www.sarusersmanual.com/>, 2004.
- [2] IEEE Global History Network, *Synthetic Aperture Radar*, [http : //www.ieeeahn.org/wiki/index.php/SyntheticApertureRadar](http://www.ieeeahn.org/wiki/index.php/SyntheticApertureRadar).
- [3] C. V. Jakowatz, Jr., D. E. Wahl, P. H. Eichel, D. C. Ghiglia, and P. A. Thompson, *Spotlight-Mode Synthetic Aperture Radar: A Signal Processing Approach*, Springer, 1996.
- [4] D. E. Wahl, P. H. Eichel, D. C. Ghiglia, and C. V. Jakowatz, Jr., "Phase Gradient Autofocus - A robust tool for high resolution SAR phase correction," *IEEE Trans. Aerosp. Electron.Syst.*, vol. 30, no. 7, pp. 827–835, 1994.
- [5] L. Xi, L. Guosui, and J. Ni, "Autofocusing of ISAR images based on entropy minimization," *IEEE Trans. Aerosp. Electron. Syst.*, vol. 35, no. 10, pp. 1240–1252, 1999.
- [6] J. R. Fienup, "Synthetic-aperture radar autofocus by maximizing sharpness," *Optics Letters*, vol. 25, pp. 221–223, 2000.
- [7] J. R. Fienup and J. J. Miller, "Aberration correction by maximizing generalized sharpness metrics," *J. Opt. Soc. Amer. A*, vol. 20, no. 4, pp. 609–620, 2003.
- [8] T. J. Kragh, "Monotonic iterative algorithm for minimum-entropy autofocus," *Adaptative Sensor Array Processing (ASAP)*, 2006.

- [9] R. L. Morrison, Jr., M. N. Do, and D. C. Munson, Jr., “SAR image autofocus by sharpness optimization: A theoretical study,” *IEEE Trans. Image Processing*, vol. 16, pp. 2309–2321, 2007.
- [10] F. Berizzi and G. Corsini, “Autofocusing of inverse synthetic aperture radar images using contrast optimization,” *IEEE Trans. Aerosp. Electron. Syst.*, vol. 32, no. 7, pp. 1185–1191, 1996.
- [11] M. P. Hayes and S. A. Fortune, “Recursive phase estimation for image sharpening,” *presented at the Image and Vision Computing New Zealand*, 2005.
- [12] R. G. Paxman and J. C. Marron, “Aberration correction of speckled imagery with an image-sharpness criterion,” *Statistical Optics, Proc. SPIE*, vol. 976, pp. 37–47, 1988.
- [13] T. C. Calloway and G. Donohoe, “Subaperture autofocus for synthetic aperture radar,” *IEEE Trans. Aerosp. Electron. Syst.*, vol. 30, pp. 617–621, 1994.
- [14] R. L. Morrison, Jr., M. N. Do, and D. C. Munson, Jr., “MCA: A multichannel approach to SAR autofocus,” *IEEE Trans. Image Processing*, vol. 18, pp. 840–853, 2009.
- [15] W. D. Brown and D. C. Ghiglia, “Some methods for reducing propagation-induced phase errors in coherent imaging systemsI: Formalism,” *J. Opt. Soc. Amer. A*, vol. 5, pp. 924–942, 1988.
- [16] D. C. Ghiglia and W. D. Brown, “Some methods for reducing propagation-induced phase errors in coherent imaging systemsII: Numerical results,” *J. Opt. Soc. Amer. A*, vol. 5, pp. 943–957, 1988.
- [17] C. V. Jakowatz, Jr., and D. E. Wahl, “Eigenvector method for maximum-likelihood estimation of phase errors in synthetic aperture radar imagery,” *J. Opt. Soc. Amer. A*, vol. 10, pp. 2539–2546, 1993.
- [18] P. H. Eichel, D. C. Ghiglia, and C. V. Jakowatz, Jr., “Speckle processing method for synthetic aperture radar phase correction,” *Opt. lett.*, vol. 14, pp. 1101–1103, 1989.

- [19] L. Kuang-Hung, A. Wiesel, and D. C. Munson, Jr., “Synthetic aperture radar autofocus via semidefinite relaxation,” *IEEE Int. Conf. Acoustics, Speech, Signal Processing*, 2010.
- [20] M. Çetin and W. C. Karl, “Feature-enhanced synthetic aperture radar image formation based on nonquadratic regularization,” *IEEE Trans. Image Processing*, pp. 623–631, 2001.
- [21] J. W. Burns, N. S. Subotic, and D. Pandelis, “Adaptive decomposition in electromagnetics,” in *Proc. Int. Symp. Antennas Propag. Soc.*, p. 19841987, 1997.
- [22] T. J. Kragh and A. A. Kharbouch, “Monotonic iterative algorithms for SAR image restoration,” in *Proc. IEEE Int. Conf. Image Processing*, p. 645648, 2006.
- [23] M. Çetin, “Feature-enhanced synthetic aperture radar imaging,” *PhD Thesis, Boston University*, 2001.
- [24] A. C. Kak and M. Slaney, *Principles of Computerized Tomographic Imaging*, New York: IEEE Press, 1988.
- [25] D. C. Munson, Jr., J. D. O’Brien, and W. K. Jenkins, “A tomographic formulation of spotlight-mode synthetic aperture radar,” *Proc. IEEE*, vol. PROC-71, pp. 917–925, 1983.
- [26] D. W. Warner, D. Ghiglia, A. FitzGerrell, and J. Beaver, “Two-dimensional phase gradient autofocus,” *Image reconstruction from incomplete data, Proc. SPIE*, vol. 4123, pp. 162–173, 2000.
- [27] W. G. Carrara, R. M. Majewski, and R. S. Goodman, *Spotlight Synthetic Aperture Radar: Signal Processing Algorithms*, Artech House, 1995.
- [28] W. C. Karl, *Regularization in Reconstruction and Restoration in Handbook of Image and Video Processing ed. by A. Bovik*, Academic Press Limited, 2000.

- [29] *MSTAR, Air Force Research Laboratory, Model Based Vision Laboratory, Sensor Data Management System*, <http://www.mbulab.wpafb.af.mil/public/sdms/datasets/mstar/>.
- [30] *Backhoe Data Sample & Visual-D Challenge Problem, Air Force Research Laboratory, Sensor Data Management System*, <https://www.sdms.afrl.af.mil/main.htm>.
- [31] M. Çetin and W. C. Karl, “Superresolution and edge-preserving reconstruction of complex-valued synthetic aperture radar images,” *IEEE Int. Conf. on Image Processing (ICIP)*, pp. 701–704, 2000.
- [32] D. L. Donoho and M. Elad, “Optimally sparse representation in general (non-orthogonal) dictionaries via l_1 minimization,” *Proc. Natl. Acad. Sci.*, vol. 100, pp. 2197–2202, 2003.
- [33] L. C. Potter, E. Ertin, J. T. Parker, and M. Çetin, “Sparsity and compressed sensing in radar imaging,” *Proc. of the IEEE*, vol. 98, pp. 1006–1020, 2010.
- [34] V. M. Patel, G. R. Easley, D. M. Healy, and R. Chellappa, “Compressed sensing for synthetic aperture radar imaging,” *IEEE International Conference on Image Processing*, 2009.
- [35] R. Baraniuk and P. Steeghs, “Compressive radar imaging,” in *Proc. IEEE 2007 Radar Conf.*, p. 128133, 2007.
- [36] C. Gurbuz, J. McClellan, and R. Scott, Jr., “A compressive sensing data acquisition and imaging method for stepped frequency GPRs,” *IEEE Trans. Signal Processing*, vol. 57, pp. 2640–2650, 2009.
- [37] I. Stojanovic, W. C. Karl, and M. Çetin, “Compressed sensing of mono-static and multi-static SAR,” *Algorithms Synthetic Aperture Radar Imagery XVI, Proc. SPIE*, 2009.
- [38] C. Berger, S. Zhou, and P. Willett, “Signal extraction using compressed sensing for passive radar with OFDM signals,” in *Proc. 11th Int. Conf. Inf. Fusion*, p. 16, 2008.

- [39] I. Stojanovic and W.C. Karl, “Imaging of moving targets with multi-static SAR using an overcomplete dictionary,” *IEEE Journal of Selected Topics in Signal Processing*, vol. 4, pp. 164–176, 2010.
- [40] M. Çetin and A. Lanterman, “Region-enhanced passive radar imaging,” *Proc. Inst. Elect. Eng. Radar, Sonar Navig.*, vol. 152, pp. 185194, 2005.
- [41] M. A. Herman and T. Strohmer, “High-resolution radar via compressed sensing,” *IEEE Trans. Signal Processing*, vol. 57, pp. 22752284, 2009.
- [42] K. R. Varshney, M. etin, J. W. Fisher, III, and A. S. Willsky, “Sparse signal representation in structured dictionaries with application to synthetic aperture radar,” *IEEE Trans. Signal Processing*, vol. 56, pp. 35483561, 2008.
- [43] C. D. Austin and R. L. Moses, “Wide-angle sparse 3D synthetic aperture radar imaging for nonlinear flight paths,” in *Proc. IEEE Nat. Aerosp. Electron. Conf.*, p. 330336, 2008.
- [44] C. Austin, E. Ertin, and R. L. Moses, “Sparse multipass 3D imaging: Applications to the GOTCHA data set,” *Defense Security Symp. Algorithms Synthetic Aperture Radar Imagery XVI, Proc. SPIE*, vol. 7337, pp. 733703–1733703–12, 2009.
- [45] M. Ferrara, J. Jackson, and M. Stuff, “Three-dimensional sparse-aperture moving-target imaging,” *Algorithms Synthetic Aperture Radar Imagery XIV, Proc. SPIE*, vol. 6970, pp. 697006, 2008.
- [46] D. L. Mensa, *High Resolution Radar Imaging*, MA: Artech House, 1981.
- [47] B. Borden, “Maximum entropy regularization in inverse synthetic aperture radar imagery,” *IEEE Trans. Signal Processing*, vol. 40, pp. 969–973, 1992.
- [48] M. Herman and T. Strohmer, “General deviants: An analysis of perturbations in compressed sensing,” *IEEE Journal of Selected Topics in Signal Processing: Special Issue on Compressive Sensing*, vol. 4(2), pp. 342–349, 2010.

- [49] M. Çetin, W. C. Karl, and A. S. Willsky, “Feature-preserving regularization method for complex-valued inverse problems with application to coherent imaging,” *Opt. Eng.*, vol. 45, 2006.
- [50] N. Ö. Önhon and M. Çetin, “A non-quadratic regularization based technique for joint SAR imaging and model error correction,” *Algorithms for Synthetic Aperture Radar Imagery XVI, Proc. SPIE*, vol. 7337, 2009.
- [51] N. Ö. Önhon and M. Çetin, “A sparsity-driven approach for joint SAR imaging and phase error correction,” *IEEE Transactions on Image Processing*, to appear in 2012.
- [52] N. Ö. Önhon and M. Çetin, “Joint sparsity-driven inversion and model error correction for radar imaging,” *IEEE Int. Conf. Acoustics, Speech, Signal Processing (ICASSP)*, pp. 1206–1209, 2010.
- [53] M. Çetin and R. L. Moses, “SAR imaging from partial-aperture data with frequency-band omissions,” *Algorithms for Synthetic Aperture Radar Imagery XII, Proc. SPIE*, vol. 5808, pp. 32–43, 2005.
- [54] Ö. Batu and M. Çetin, “Parameter selection in sparsity-driven SAR imaging,” *IEEE Trans. Aerospace and Electronic Systems*, vol. 47, pp. 3040–3050, 2011.
- [55] Ö. Batu, “Parameter selection in non-quadratic regularization-based SAR imaging,” *Master Thesis, Sabancı University*, 2008.
- [56] A. R. Fasih, B. D. Rigling, and R. L. Moses, “Analysis of target rotation and translation in SAR imagery,” *Algorithms for Synthetic Aperture Radar Imagery XVI, SPIE*, 2009.
- [57] N. Ö. Önhon and M. Çetin, “Sparsity-driven image formation and space-variant focusing for SAR,” *IEEE Int. Conf. on Image Processing (ICIP)*, pp. 173–176, 2011.
- [58] S. Samadi, M. Çetin, and M. A. Masnadi-Shirazi, “Sparse representation-based synthetic aperture radar imaging,” *IET Radar, Sonar and Navigation*, vol. 5, no. 2, pp. 182–193, 2011.

- [59] N. Ö. Önhon and M. Çetin, “Sar moving target imaging in a sparsity-driven framework,” *SPIE Optics+Photonics, Wavelets and Sparsity XIV*, vol. 8138, 2011.
- [60] M. A. Richards, *Fundamentals of Radar Signal Processing*, McGraw-Hill, 2005.
- [61] E. J. Cands, M. B. Wakin, and S. P. Boyd, “Enhancing sparsity by reweighted l_1 minimization,” *J Fourier Anal Appl*, vol. 14, pp. 877–905, 2008.
- [62] K. R. Varshney, M. Çetin, J. W. Fisher III, and A. Willsky, “Sparse representation in structured dictionaries with application to synthetic aperture radar,” *IEEE Transactions on Signal Processing*, vol. 56, pp. 3458–3561, 2008.